Optimized orthovoltage stereotactic radiosurgery

by

Jessica M. Fagerstrom

A dissertation submitted in partial fulfillment of
the requirements for the degree of

Doctor of Philosophy

(Medical Physics)

at the

University of Wisconsin-Madison

2017

Date of final oral examination: March 7, 2017

This dissertation is approved by the following members of the Final Oral Committee:
Wesley S. Culberson, Assistant Professor, Medical Physics
Bryan P. Bednarz, Associate Professor, Medical Physics
Larry A. DeWerd, Professor, Medical Physics
Douglass L. Henderson, Professor, Engineering Physics
Michael W. Kissick, Assistant Professor, Medical Physics

For my mother, Mary Fagerstrom.

Abstract

Because of its ability to treat intracranial targets effectively and noninvasively, stereotactic radiosurgery (SRS) is a prevalent treatment modality in modern radiation therapy. This work focused on SRS delivering rectangular function dose distributions, which are desirable for some targets such as those with functional tissue included within the target volume. In order to achieve such distributions, this work used fluence modulation and energies lower than those utilized in conventional SRS.

In this work, the relationship between prescription isodose and dose gradients was examined for standard, unmodulated orthovoltage SRS dose distributions. Monte Carlo-generated energy deposition kernels were used to calculate 4π, isocentric dose distributions for a polyenergetic orthovoltage spectrum, as well as monoenergetic orthovoltage beams. The relationship between dose gradients and prescription isodose was found to be field size and energy dependent, and values were found for prescription isodose that optimize dose gradients.

Next, a pencil-beam model was used with a Genetic Algorithm search heuristic to optimize the spatial distribution of added tungsten filtration within apertures of cone collimators in a moderately filtered 250 kVp beam. Four cone sizes at three depths were examined with a Monte Carlo model to determine the effects of the optimized modulation compared to open cones, and the simulations found that the optimized cones were able to achieve both improved penumbra and flatness statistics at depth compared to the open cones.

Prototypes of the filter designs calculated using mathematical optimization techniques and Monte Carlo simulations were then manufactured and inserted into custom built orthovoltage SRS cone collimators. A positioning system built in-house was used to place the collimator and filter assemblies temporarily in the 250 kVp beam line. Measurements were performed in water using radiochromic film scanned with both a standard white light flatbed scanner as well as a prototype laser densitometry system. Measured beam profiles showed that the modulated beams could more closely approach rectangular function dose profiles compared to the open cones.

A methodology has been described and implemented to achieve optimized SRS delivery, including the development of working prototypes. Future work may include the construction of a full treatment platform.

Acknowledgments

First, I would like to thank my advisor and the UWMRRC associate director, Dr. Wesley Culberson, for his many contributions to the UWMRRC and for having me as his first advisee. Thank you also to the UWMRRC director, Dr. Larry DeWerd, and the UWADCL associate director, John Micka, for their guidance and for all they do for the lab. Many thanks to UWMRRC members who contributed to this work, particularly Manik Aima, Clifford Hammer, Benjamin Palmer, and Drs. Michael Lawless and Benjamin Rosen. Sincere gratitude to Drs. Edward Bender, Steven Howard, and Michael Kissick for their insight and enthusiasm, and to my committee, for the time and direction they offered.

Aside from the academic support I received, I also benefited from indispensable support outside of school from many people. Thank you most of all to my family, especially my wonderful mother, Mary Fagerstrom, for supporting me in undertaking this doctoral project. I owe many thanks to current lab members for the poker nights, camping trips, and Badger games, most especially Vimal Desai, Eric Similie, Sameer Taneja, and Natalie Viscariello. Thank you to the other dear friends I met in Madison, especially to the Tuesday potluck group, the Grace Episcopal pantry volunteers, Dr. Laura Bartol, Ruth Bronston and Charles Buse, Lindsay Jones, Dr. Jessica and Andrew Miller, and Anne Palmer. I received training in clinical physics (and pidgin) at the Queen's and Kuakini Medical Centers, for which I am indebted to the physics and dosimetry teams, especially to Emily Hirata. Thank you also to the rest of my Hawaii ohana—who are too numerous to list—but especially to Rebecca Arlander and Frank Silva. Finally, thank you to Matthew Wuerffel.

Contents

List of Figures

List of Tables

List of Abbreviations

AANS	American Association of Neurological Surgeons
AAPM	American Association of Physicists in Medicine
ABS	acrylonitrile butadiene styrene
ACR	American College of Radiology
ASTRO	American Society for Therapeutic Radiology and Oncology
AVM	arteriovenous malformation
BCQN	bound-constrained quasi-Newton
BEAMDP	BEAM Data Processor program
BRW	Brown-Roberts-Wells SRS head frame
CDF	cumulative distribution function
CH	condensed history
CNS	central nervous system
CRI	cutaneous radiation injury
CSA	constrained simulated annealing
CT	computed tomography
DGI	dose gradient index
dpi	dots per inch
DVH	dose-volume histogram
EBT	External Beam Therapy radiochromic film
EDK	energy-deposition kernel
EGSnrc	National Research Council's Electron Gamma Shower Monte Carlo code

FDA	U.S. Food and Drug Administration
FWHM	full width at half maximum
GA	Genetic Algorithm
HC	homogeneity coefficient
HPC	high performance computing
HVL	half-value layer
ICRP	International Commission on Radiological Protection
ICRU	Internal Commission on Radiation Units and Measurements
ICVI	Integrated Conical collimator Verification and Interlock
IMRT	intensity modulated radiation therapy
IP	integer programming
KKT	Karush-Kuhn-Tucker
LDS	laser densitometry system
LET	linear energy transfer
LRA	lateral response artifact
MCNP	Monte Carlo N-Particle transport code
MDPD	ratio of maximum dose to prescription dose
MLC	multileaf collimator
MRI	magnetic resonance imaging
MTF	modulation transfer function
MTLE	mesial temporal lobe epilepsy
NCCTG	North Central Cancer Treatment Group
NIST	National Institute of Standards and Technology
NLP	nonlinear programming
OD	optical density
PA	pituitary adenoma
PDD	percent depth dose

PDF	probability density function
PITV	ratio of prescription isodose volume to target volume
PMMA	polymethyl methacrylate
QA	quality assurance
RBE	relative biological effectiveness
ROI	region of interest
RTOG	Radiation Therapy Oncology Group
SAD	source-to-axis distance
SBRT	stereotactic body radiation therapy
SQP	sequential quadratic programming
SRS	stereotactic radiosurgery
SSD	source-to-surface distance
TIFF	tagged image file format
UWADCL	University of Wisconsin Accredited Dosimetry Calibration Laboratory
UWMRRC	University of Wisconsin Medical Radiation Research Center
UWRCL	University of Wisconsin Radiation Calibration Laboratory

Chapter 1

Introduction

1.1 Overview of dissertation

In its 1995 Therapy Committee Task Group Report 42, the American Association of Physicists in Medicine (AAPM) defines stereotactic radiosurgery (SRS) as combining "the use of a stereotactic apparatus and energetic radiation beams to irradiate [a] lesion with a single treatment," the result of which is a concentrated dose in small intracranial or spinal target volumes with steep dose gradients at the outer edges of the treatment volume (Schell et al., 1995). According to the American Association of Neurological Surgeons (AANS) and American Society for Therapeutic Radiology and Oncology (ASTRO), SRS is currently defined as the treatment in a single fraction of a central nervous system (CNS) target site, using externally generated ionizing radiation with precise positioning and localization of the treatment volume. The rapid dose fall-off near the edge of the target volume provides the ability to spare nearby critical structures (Barnett et al., 2007). Today, stereotactic radiosurgery and radiotherapy procedures have moved into the mainstream radiation therapy clinic as a minimally invasive alternative to surgical resection for patients who are non-surgical candidates or for other reasons elect not to undergo surgery (Alexander and Loeffler, 1999).

This project sought to design, build, model, and characterize an orthovoltage energy-modulated SRS system. This involved first the design of orthovoltage beam filters for energy fluence modulation of stereotactic cones, based on mathematical optimization of a pencil-beam model. This was accomplished by the calculation of a beamlet kernel database indexed by attenuating material thickness for epoxy-infiltrated bonded tungsten thicknesses ranging from 0.5 mm to 5 mm. Source-blurring kernel parameters were determined computationally by deconvolving beamlet kernel distributions from full Monte Carlo-calculated dose distributions of modulated fields, then Genetic Algorithm (GA) optimization was used to define the optimal energy fluence to produce a dose-to-water distribution approximating rectangular function geometry at 5 cm depth in water. Next, prototype stereotactic collimation and filtration assemblies were developed, modeled, and constructed for use with the NIST-matched University of Wisconsin Accredited Dosimetry Calibration Laboratory (UWADCL) orthovoltage beams based on the results of the optimization. A custom positioning chassis was designed and machined for the temporary and reproducible alignment of the assembly in the orthovoltage beam path. Four nondivergent cone collimators were constructed from free machining brass to be used optionally along with epoxy-infiltrated bonded tungsten filters of variable thicknesses. The EGSnrc Monte Carlo code was used to model the system. This model, along with EBT3 radiochromic film, were used to characterize the dosimetry of the system. An EBT3 dose response curve in water was created, then film and Monte Carlo methods were used to compare dose-to-water distributions of collimated-modulated, and collimated-unmodulated beams to an open $(10 \times 10)\,\mathrm{cm}^2$ field. Specifically, qualitative dose distributions as well as quantitative measurements of static beam dose profile penumbra widths and beam flatness were examined, and compared to standard, high-energy beam profiles.

1.2 Description of upcoming chapters

Chapter 2 provides relevant background information for the project. The chapter includes an overview of the rectangular function dose distribution in radiosurgery, which is central to this work, and discusses target sites of interest for the orthovoltage energy-modulated SRS system, including benign tumors, vascular malformations, functional disorders, and pituitary tumors. Relevant previous work is summarized, including published work describing optimal modulated-fluence stereotactic cones with a 6 MV linear accelerator, as well as studies of orthovoltage energy ranges for SRS and stereotactic body radiation therapy (SBRT). This material is applied to the current work to arrive at the motivations and goals of this thesis.

Chapter 3 describes the film dosimetry methods used throughout this work. Radiochromic film, specifically EBT3 film, is described, including an overview of previous publications on film dosimetry relevant to this work. Basic film handling methods used in the project are detailed as well as scanning digitization protocols used for both a white light, flatbed scanner and a prototype laser densitometry system designed and built at the University of Wisconsin Medical Radiation Research Center (UWMRRC). The film calibration processes, using both Monte Carlo methods as well as measurements in water, are described. A description of the film dosimetry full uncertainty analysis calculation methodology is included.

Chapter 4 provides a general analysis of dose gradients and prescription isodose for orthovoltage systems. This is accomplished through the construction of a pencil-beam model. The Monte Carlo and computational methods used to generate pencil kernels are described. These kernels are then used to determine isotropic, 4π dose distributions in water phantoms of various sizes. Distributions are calculated from a variety of monoenergetic orthovoltage energies as well as a polyenergetic spectrum, collimated with a range of stereotactic cone sizes. These distributions are analyzed in terms of prescription isodose line and dose gradient index (DGI). The relationship between DGI and prescription isodose was found to be

both field size and energy dependent, and values were found to exist that optimize DGI in this generalized problem.

In Chapter 5, the pencil-beam model described in Chapter 4 was adjusted to one applicable for the UWMRRC modulated orthovoltage SRS system cone prototypes. This adjustment involved using very different input kernels for the model than those previously published for use with a 6 MV linear accelerator, and a description of the computational methods used to generate the kernels is included. The model was then used optimize the spatial distribution of attenuating material in order to achieve dose distributions approaching rectangular functions. These results were used to design optimized orthovoltage SRS cone and filter assemblies. The chapter describes the optimization methods used in this work, including a description of the Genetic Algorithm search heuristic, the chosen optimization constraints, drawbacks of the methodology, and examples of resulting single beam dose distributions from optimized energy fluence compared to those resulting from standard (open) orthovoltage SRS. An uncertainty analysis of the Monte Carlo methods used to calculate these profiles is included. The orthovoltage profile results are compared to representative measured data from a 6 MV linear accelerator. In addition to the investigation of single beam profiles, 4π irradiation geometries are used to examine doses at shallow depths for modulated and unmodulated orthovoltage beams as well as unmodulated ^{60}Co beams. A DGI analysis (similar to the those introduced in Chapter 4) is included for the UWMRRC system.

Chapter 6 details the construction of the cone and filter assemblies designed in Chapter 5 using both in-house machining techniques as well as the commissioning of an outside prototyping firm capable of binderjetting, an additive manufacturing technique, using tungsten. Also discussed are the construction of a variable-position ceiling alignment system and a temporary aluminum framing chassis for positioning the collimator and filter assemblies along the UWMRRC orthovoltage unit beam line. Radiochromic EBT3 film measurements were performed using the chassis, cone, and filter system in a custom, thin-window water

phantom. These films were scanned with both the flatbed scanner and the UWMRRC prototype laser densitometry system described in Chapter 3. A description of the automated process of extraction of beam profiles from the film data is included, and the resulting profile data are analyzed.

Chapter 7 includes a summary of the conclusions made from this work, as well as an outline of pertinent factors concerning possible future treatment platforms, including relative biological effectiveness, design considerations, and possible radiation-induced complications. Finally, some recommendations for future work are included based on the novel prototypes designed and characterized in this work.

Chapter 2

Background and motivation

A wide variety of imaging, positioning, planning, motion-management, and delivery techniques have been developed for use with SRS: standard linear accelerators may be used with tertiary collimators such as cones or multileaf collimators (MLCs) to create sharp penumbrae; miniature linear accelerators may be mounted on a robotic arm to deliver SRS, as with the CyberKnife® robotic system; Gamma Knife® units utilize approximately 200 ^{60}Co sources to direct radiation toward a focal target; neutrons or heavy charged particles may be used for stereotactic procedures; and rigid stereotactic frames or other, less invasive, frameless techniques may be used to localize the target to the high degree of accuracy necessary for radiosurgery (Seung et al., 2013). In addition to variations in equipment, prescriptions may also vary depending on the technique as well as physician preference (for example, Gamma Knife prescriptions commonly specify dose to the 50% isodose line, whereas linear accelerator-based SRS system prescriptions usually specify dose to much higher isodose lines) (Badakhshi, 2016; Kooy, 1993; Yamamoto, 1999). Finally, a range of target sites have been successfully treated with SRS, including vascular disorders, metastatic disease, functional disorders, primary malignancies, and primary benign disease (Kondziolka et al., 2000, 2012; Larson et al., 1993; Levy et al., 1993). The wide variety of SRS equipment, physicians preference, and patient population result in diverse final dose distributions.

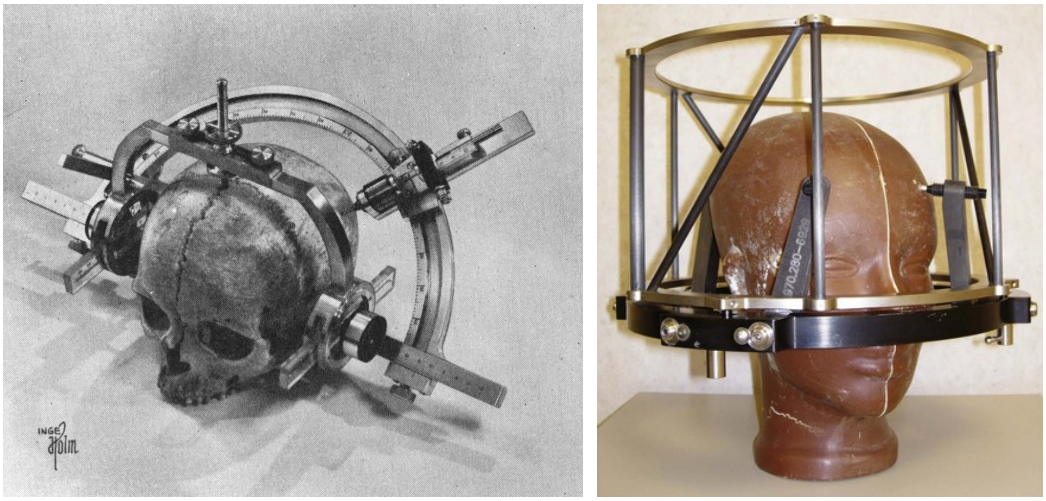

(a) (b)

Figure 2.1: Photographs of examples of localizing stereotactic head frames used for SRS treatment procedures. (a) An early localizing SRS head frame affixed to a human skull, published by Leksell in 1949. Reprinted with permission from L. Leksell, "A stereotactic apparatus for intracerebral surgery," Acta Chirurgica Scandinavica, 99, 229–233, 1949. Copyright 1949, John Wiley & Sons, Inc. (b) A modern SRS head frame, as well as the Brown-Roberts-Wells (BRW) coordinate system affixed, to an anthropomorphic human head phantom. Reprinted with permission from 2012 D. McHaffie et al., "Stereotactic irradiation: linear accelerator and Gamma Knife," Clinical Radiation Oncology, 3rd Edition. 331–343, 2012. Copyright 2012, Saunders, an imprint of Elsevier, Inc.

2.1 Historical background

The idea of orthovoltage energy SRS is not new. Early use of radiation for therapeutic purposes primarily used low-energy x- and γ-rays based on available isotopes and x-ray tubes. X-rays (then known as "Roentgen rays") were first used to treat the human central nervous system (CNS) in 1905 (Raymond, 1905), and were subsequently used to treat a variety of conditions, with the first reported treatment of an intracranial tumor published four years later (Gramegna, 1909). Though reported results from these initial uses were generally positive, they were often not accompanied by rigorous discussion of experimental technique and the results were not always validated by subsequent examinations (Cleave, 1963). In 1927, key studies in radiobiology (Regaud and Ferroux, 1927) were published

suggesting the value of fractionation. These studies indicated that male livestock could not be sterilized in a single dose of radiation to the testes without incurring skin necrosis, but could be sterilized without skin necrosis if the radiation dosage was delivered in multiple doses over a period of weeks (Bernier et al., 2004; Hall and Giaccia, 2006). Prior to this work, radiation was often delivered in a few large doses or a single dose. In the 1950s, Swedish neurosurgeon Lars Leksell returned to the idea of treating small intracranial targets with a single dose by means of localizing the treatment volume with a stereotactic frame he developed (Leksell, 1949, 1951). In 1968, the first stereotactic Gamma Knife unit using ^{60}Co was installed at Sophiahemmet Hospital in Stockholm, Sweden (Leksell, 1983). Some modern localizing head frames rely on similar design components as those first proposed by Leksell and other early pioneers in the field of SRS (Figure 2.1).

SRS has dramatically gained popularity since its introduction in Leksell's landmark studies. In the most recent available AAPM professional information survey profiling the radiation oncology departments of AAPM members, 45% of surveyed clinics offered either stereotactic radiosurgery or stereotactic radiotherapy (AAPM, 2004). Ten years later, the most recent Abt Associates Inc. study completed for the AAPM indicated that in 2014, 82% of surveyed clinics offered single-fraction stereotactic radiosurgery, 85% offered multiple-fraction stereotactic radiotherapy, and 90% offered stereotactic body irradiation (Abt Associates, 2015). The expanding clinical interest in SRS stems from its ability to exploit basic radiobiological advantages by ablating a target with doses large enough to overwhelm repair functions (Timmerman, 2008; Vaughan and Rao, 2016), its robust track record in patient outcomes (Nedzi, 2008), its availability to patients who are not surgical candidates (O'Neill et al., 2003), and its cost-effectiveness compared to surgical resection (Rutigliano et al., 1995).

2.2 Rectangular function dose distribution in radiosurgery

This project focuses on the creation of a homogeneous dose distribution conforming strictly to a target volume, with steep dose gradients outside the target—an overall distribution similar in shape to a rectangular function or a "top hat." Podgorsak and Podgorsak (1999) claimed, "the important parameters to be considered with regard to a radiosurgical treatment plan are: (1) conformity of the prescribed isodose surface to the target volume; (2) volume of healthy tissue irradiated by the prescription isodose surface; and (3) dose homogeneity inside the target volume." Creating these idealized rectangular function dose distributions is the goal of this project.

Evaluation of both the homogeneity and the steep dose fall-off have been quantified in various ways. The Radiation Therapy Oncology Group (RTOG) of the American College of Radiology (ACR) is a national clinical cooperative group that conducts radiation therapy research and multicenter clinical trials. When institutions participating in clinical trials submit patient radiation therapy plans to the RTOG, the organization uses various quality assurance (QA) metrics to quantify dose homogeneity within the target as well as the dose conformity of the treatment volume relative to the target volume, and to evaluate how closely a given plan follows protocol guidelines. The RTOG's dose homogeneity QA metric measures the ratio of the maximum dose (MD) to the prescribed dose (PD). The MD/PD (or simply MDPD) index more closely follows protocol guidelines the closer to a homogeneous dose the target receives. Similarly, the RTOG's dose conformity QA metric measures how closely the prescription isodose line conforms to the target volume. The ratio of prescription isodose (PI) volume to target volume (TV), or PI/TV (or simply PITV) index, more closely follows protocol guidelines the closer to a conformal dose the target receives (Andrews et al., 2004; Brown et al., 2014; Shaw et al., 1993, 2000; Souhami et al., 2004; Sperduto et al., 2012). The RTOG's SRS criteria are summarized in Tables 2.1 and 2.2.

Table 2.1: Summary of the RTOG's SRS criteria according to the RTOG SRS QA Guidelines and Protocols 0320, 9005, 9305, 9508.

	per protocol	minor variation	major variation
dose homogeneity (MDPD)	≤ 2.0	> 2.0 but < 2.5	≥ 2.5
dose conformity (PITV)	≥ 1.0 and ≤ 2.0	≥ 0.9 but < 1.0 or > 2.0 but < 2.5*	≤ 0.9 or ≥ 2.5*
isodose line as percentage of prescription encompassing target	$\geq 90\%$	$< 90\%$ but $\geq 80\%$	$< 80\%$

* RTOG 0320 specifies using a value of 3.5 instead of 2.5.

Table 2.2: Summary of the RTOG's SRS criteria according to RTOG Protocol 1270/North Central Cancer Treatment Group (NCCTG) Protocol N107C.

	per protocol	minor variation	major variation
dose conformity (PITV) for lesions $\geq$5 mm	≥ 1.0 and ≤ 2.0	≥ 0.9 but < 1.0 or > 2.0 but < 3.0	≤ 3.0
dose conformity (PITV) for lesions <5 mm	≥ 3.0	>3.0 but ≤ 3.5	>3.5
isodose line as percentage of prescription encompassing target	$\geq 95\%$	90%	$< 90\%$

Hong et al. (2011) noted that the RTOG criteria do not address dose fall-off outside the target; while a smaller PITV value may imply a more conformal plan, this value does not include information about isodose volumes less than the prescription volume. Multiple metrics have been proposed to quantify the sharpness of the dose gradient outside of the target. One such metric is the dose gradient index (DGI) proposed by Paddick and Lippitz (2006):

$$DGI = \frac{Vol_{50\%\,\mathrm{Rx}}}{Vol_{100\%\,\mathrm{Rx}}}, \tag{2.1}$$

where $Vol_{50\%\,\mathrm{Rx}}$ is the volume of the three-dimensional shape encompassed by the 50% prescription isodose line and $Vol_{100\%\,\mathrm{Rx}}$ is the volume of the three-dimensional shape encompassed by the 100% prescription isodose line.

Intuitively, minimizing treatment volume by creating sharper dose gradients outside a conformal target would be expected to reduce toxicity. Calzavara et al. (1966) studied the radiobiological effects of penumbrae in rat liver irradiations and found penumbral dose was harmful to healthy tissue surrounding the target volume, but it was sublethal to targeted neoplastic cells. They concluded that penumbral dose should be minimized because it only contributes to healthy tissue integral dose without adequate target control in those volumes. The dose-volume effect has been well documented in SRS procedures, beginning with Kjellberg's work on brain necrosis following proton radiosurgery (Kjellberg, 1979; Kjellberg et al., 1983). In general, the smaller the target volume, the greater the dose to which it can be irradiated while avoiding unacceptable toxicity (Flickinger et al., 1992; Nedzi et al., 1991). Decreases in length of spinal cord irradiated using photon and proton beams in small (Bijl et al., 2002; Hopewell et al., 1987; van der Kogel, 1991, 1993) and large animal studies (Powers et al., 1998; Schultheiss et al., 1994) have shown to decrease the incidence of varying degrees of myelopathy in CNS irradiations. Massager et al. (2009) showed that rapid dose fall-off in radiosurgery is associated with less risk of adverse histological changes in the normal tissue surrounding the target in animal studies.

While several studies have indicated support for minimizing treatment volume in SRS, creating homogeneous dose distributions within the target volume is not always desirable. The AAPM's Task Group on stereotactic body radiation therapy (SBRT) stated that including dose heterogeneous hot spots within an SBRT target, as long as the target does not involve functional normal tissue, offers the advantage of eradicating radioresistant hypoxic cells. These types of cells are often located, for example, within the center of lung targets (Benedict et al., 2010). Nevertheless, increased homogeneity of dose within intracranial SRS target volumes has been associated with reduction of toxicities in certain target sites (to be detailed individually in the following section), making the "flat top" aspect of the "top hat" dose distribution a worthy goal (Andrews et al., 2001; Balagamwala et al., 2012; Massager et al., 2006).

2.3 Target sites of interest for the orthovoltage energy-modulated SRS system

SRS has been used to treat a variety of histologies. Dose homogeneity becomes clinically important when the target volume contains or is immediately proximal to sensitive normal tissue. The risk of toxicity may also be further reduced by increasing dose gradients at the target periphery (Barnett et al., 2007; Shaw et al., 1996).

As discussed in Section 2.2, highly conformal dose distributions resulting in rapid dose fall-off in the surrounding tissue is essential for most SRS treatments. For some types of tumors with hypoxic and/or radioresistant central regions, it may be desired to deliver an inhomogeneous dose distribution for the purposes of tumor control. However, this is not the case for all target sites, especially in terms of avoiding complications. Nedzi et al. (1991) completed a retrospective study of patients treated with linear accelerator-based SRS for recurrent or inoperable intracranial tumors. They found that, of all variables studied, dose inhomogeneity within the target volume was the variable most highly associated with

toxicity. Tumor dose inhomogeneity had a higher log-likelihood in their logistic model of complication rates than any other single variable associated with toxicity (including maximum tumor dose, number of isocenters, maximum normal tissue dose, and tumor volume), and a higher log-likelihood than any other two variables combined.

Balancing target response with complication risk is a basic tenet for radiation oncology in general, and the orthovoltage energy-modulated SRS system offers a new tool to this end. For illustrative purposes, a selection of common and/or challenging radiosurgical targets that would benefit from such a system will be briefly discussed, including some benign tumors, vascular malformations, functional disorders, and pituitary tumors.

2.3.1 Benign intracranial lesions

According to classification by the World Health Organization, benign lesions are relatively slow-growing and unlikely to metastasize; however, benign lesions in the brain can present serious health risks to patients due to involvement of functional tissue and increased inflammation and pressure (Louis et al., 2007). Clinical presentation may include symptoms of seizures, hemiparesis, visual field loss, diplopia, sensorineural hearing loss, vertigo, dysphagia, facial numbness, and gait ataxia (DeAngelis, 2004; DeAngelis and Posner, 2001; Mansky and Hamilty, 2001). Among benign tumors, meningiomas and schwannomas are well demarcated using contrast-enhanced computed tomography (CT) or magnetic resonance imaging (MRI) (Kondziolka et al., 1991) and are the benign neoplasms most commonly treated using SRS (Biswas et al., 2003). Schwannomas, meningiomas, and craniopharyngiomas all present challenges for standard SRS delivery, for which the orthovoltage energy-modulated system proves a promising new modality.

2.3.1.1 Vestibular schwannomas

Vestibular schwannomas (sometimes called acoustic neuromas) represent 6–10% of all intracranial tumors (Ruzevick et al., 2013b). They arise from the Schwann cells covering

the vestibular portion of the vestibulocochlear cranial nerve. The most common symptom associated with vestibular schwannomas is hearing loss. If left untreated, the condition can lead to compression of the cerebellum and brainstem (Andrews et al., 1998; DeAngelis and Posner, 2001). SRS treatments of vestibular schwannomas necessarily irradiate a portion of the vestibular nerve as part of the target volume, though damage to this nerve (dependent on the severity) results in vertigo, tinnitus, nystagmus, and partial or complete hearing loss in the affected ear (Hammond and Masel, 2012). Treatment planning is further complicated by the immediate vicinity of the facial, cochlear, and trigeminal nerves (Ruzevick et al., 2013b). SRS has proven successful in achieving high rates of tumor control (Kondziolka et al., 1998), though at the expense of high rates of complications (achieving only a hearing preservation of approximately 50–75% in patients with serviceable hearing before SRS) (Kim et al., 2013). Chang et al. (2005) suggested improved tumor dose homogeneity may help improve hearing preservation, a result confirmed by Massager et al. (2006). Due to the need for steep dose fall-off in order to avoid damaging adjacent cranial nerves, as well as uniform dose to the tumor to avoid overdosing the vestibular nerve within the target volume, the orthovoltage energy-modulated SRS system offers a valuable option for treatment of this challenging site.

2.3.1.2 Meningiomas

Meningiomas are tumors arising from the meninges, which are connective tissue membranes enveloping the spinal cord and brain. Meningiomas are usually benign. They are also common, representing the most frequently diagnosed primary brain tumor and accounting for 34% of all primary brain and CNS tumors reported in the United States (Mansky and Hamilty, 2001; Wiemels et al., 2010). Anatomical location of meningiomas vary, but SRS target volumes necessarily may include functional tissue, and often abut critical structures (Chung et al., 2015). As an example, primary optic nerve sheath meningiomas grow circumferentially along the optic nerve, and targets may abut or include the ophthalmic artery

and central retinal artery (Marchetti et al., 2011). Base of skull meningiomas, such as those in the cavernous sinus, often infiltrate critical structures such as the optic chiasm, brainstem, carotid arteries, and cranial nerves (Chan et al., 2004). Pollock and Stafford (2005) suggested that treatment of cavernous sinus meningiomas using linear accelerator-based radiosurgery may benefit from greater dose homogeneity and lower maximum dose compared to Gamma Knife treatments. Similarly, Spiegelmann et al. (2002) stated that such targets contain critical neurovascular structures and therefore it is important to consider the conformity and homogeneity of treatment dose within the target when planning. Chang and Adler (1997) reviewed linear accelerator-based SRS treatment of cranial base meningiomas, noting that, due to the location of the targets, cranial nerves must necessarily be treated with a full dose. Again, the lack of dose hot spots within the target is crucial. Hakim et al. (1998) reviewed meningiomas arising in a variety of intracranial anatomical locations treated with linear accelerator-based SRS, stating that maximum dose and dose inhomogeneity within the target are important variables associated with complications. They also noted that proximity to critical structures presents a risk factor for complications. Therefore, the orthovoltage energy-modulated SRS system could be a valuable tool in offering rectangular function dose distributions to provide both the necessary rapid dose fall-off outside the target as well as target dose homogeneity.

2.3.1.3 Craniopharyngiomas

Craniopharyngiomas are benign tumors that arise from remnants of the craniopharyngeal duct and/or Rathke cleft. Though relatively rare in adults (accounting for 1–4% of intracranial tumors), they present with greater frequency in pediatric patients and represent the most common non-glial intracranial tumor in children (della Cuna and Gasparini, 1988; DeAngelis and Posner, 2001; Hoffman, 1994). Surgical resection is complicated by the location of the tumor immediately adjacent to the optic apparatus, as well as the tendency for finger-like extensions of the tumor to adhere to critical structures such as the hypotha-

lamus, optic nerves, pituitary stalk, and carotid arteries (Chiou et al., 2001; Lee et al., 2008; Niranjan et al., 2010). If surgery is attempted, gross resection may not be possible without incurring unacceptable morbidities, and recurrent or residual craniopharyngiomas may occur. For this reason, SRS treatments of the area offer an alternative to surgery, provided the SRS dose distributions maintain sharp dose gradients at the target periphery in order to avoid critical structures outside of the target volume, and hot spots within the target volume are avoided in order to prevent radiation-induced toxicity (Demiral et al., 2014; Plowman et al., 1999). The orthovoltage energy-modulated SRS system offers such dose distributions.

2.3.2 Vascular malformations: arteriovenous malformations

Arteriovenous malformations (AVMs) constitute a type of non-neoplastic vascular lesion that can pose substantial health risks when located in the CNS. These malformations are composed of a central tangle of blood vessels (the "nidus"), in which arteries and veins are connected contiguously so that blood flows directly from arteries to veins without an intervening capillary bed (Greenberg, 2010). Left untreated, AVMs present a significant risk for rupture and hemorrhage with high rates of morbidity and mortality (Alexander and Loeffler, 1998; Lunsford, 1991; Ondra et al., 1990). Even if an untreated AVM does not rupture, it may result in the formation of large masses of vessels that feed or drain the AVMs, as well as in ischemia (a restriction of blood supply to tissues), both of which can result in seizures (Allen et al., 1978). Treatment options for AVMs include surgical resection, endovascular embolization, radiation therapy, and SRS, or a combination thereof, with the goal of excising or obliterating the nidus (Ruzevick et al., 2013a).

A major shortcoming of SRS in the treatment of AVMs is that the progressive obliteration of AVMs occurs throughout a latency period of two to three years following irradiation, during which there is still a risk of hemorrhage (Nataf et al., 2004; Pollock et al., 1995; Shrieve et al., 2010). Colombo et al. (1994; 2006; 2009) investigated variables relating to

bleeding risk during the latency period, and found that dose inhomogeneity, and, to a lesser extent, target volume, were associated with the largest risk. As a result, their planning process now involves the routine evaluation of the homogeneity and conformity indices, in an effort to deliver a highly conformal, uniform dose to the entire malformation. The modulated orthovoltage SRS system is designed to deliver such dose distributions.

2.3.3 Functional disorders: epilepsy

Epilepsy is a broad category of conditions characterized by recurrent seizures caused by electrical discharge in the brain, with underlying pathophysiology that is complex and currently ill defined (Oster et al., 2012; Pincus and Tucker, 2003). Its underlying causes are classified as genetic; structural/metabolic, including stroke, trauma, and infection (epilepsy is often cited as a symptom of AVM, see Section 2.3.2); or "unknown cause" (Berg et al., 2010). Epilepsy is a prevalent condition (approximately 20% of all neurological consultations relate to epilepsy) and imposes a high personal, social, and economic cost, often disrupting the patient's ability to drive or to maintain employment. Standard of care includes antiepileptic drug therapy; however, an estimated 20%–30% of patients suffer from drug-resistant epilepsy (Freeman et al., 2012; Kwan and Brodie, 2000; Shorvon et al., 2009). Radiosurgery offers an alternative treatment for these patients.

The most common form of epilepsy is mesial temporal lobe epilepsy (MTLE), which is one of the most medically refractory forms of human epilepsy (Engel, 2001). The treatment of MTLE with radiosurgery is currently an active area of research (Barbaro et al., 2009). Targets for MTLE include the conformal treatment of the amygdala, anterior hippocampus, and the parahippocampal gyrus, which necessitates strict conformity of the target to avoid irradiation of the brainstem and optic tract (Quigg et al., 2012). Clinicians have long observed the reduction of epileptic seizures following the irradiation of intracranial tumors and AVMs, even before the conclusion of the latency period during which the primary lesion that caused the secondary epilepsy regresses (Barcia et al., 1994; Régis et al., 2013). This

observation inspired the proposal of a "clinical differential effect," by Régis et al. (2012), defined as the induction of a functional effect by radiation while simultaneously sparing underlying functional tissue within the treatment volume. This effect is due to the capacity of low radiation doses to affect some systems while sparing others. Treating with low dose (approximately 10 Gy) in order to affect epileptic neurons preferentially while avoiding tissue necrosis was first completed by Barcia-Salorio et al. (1985; 1993; 1994) and Barcia et al. (1994) with promising results.

Dose selection and distribution (necrotizing vs. non-necrotizing) remains an unresolved question in epilepsy radiosurgery, with the need to balance seizure response with morbidity risks, particularly as compared to surgical resection (Kondziolka, 1999; Kondziolka et al., 2012, 2013). The modulated orthovoltage SRS system offers a useful tool in this area of research, particularly beneficial for its ability to offer high dose gradients outside the target in order to avoid nearby critical structures, and its treatment of well-defined, uniform doses for the study of the clinical differential effect.

2.3.4 Pituitary adenomas

The pituitary gland is positioned at the skull base in a region called the sella turcia, and secretes important hormones including growth hormone, thyroid-stimulating hormone, prolactin, and adrenocorticotropin hormone (Bonadonna and Buraggi, 1988; Saladin, 2005). Adenomas, or benign glandular tissue tumors, of the pituitary are common neoplasms, representing between 10% to 20% of all primary brain tumors (Kim et al., 2012; Raleigh et al., 2016). Pituitary adenomas (PAs) are generally classified as nonfunctioning (chemically inactive) or functioning (hormone secreting, in which the specific hormone secreted determines the resulting endocrine condition). Two major goals of treatment of PAs are to limit hormone overproduction and to remove or reduce a neoplastic disease that, unhindered, could compress normal glandular and neural structures.

Surgery is the standard treatment of PA; however, radiosurgery is an option for patients who recur following surgery, patients who are not surgical candidates, and patients with tumors that invade parasellar structures, tumors that are inaccessible at primary operation, or tumors that are subtotally resected (DeAngelis and Posner, 2001; Ganz, 1998; Iwata et al., 2011). The modulated orthovoltage SRS system could be an effective option for treating such cases. After conducting an extensive literature review, Laws et al. (2004) concluded that radiosurgery, with the intent to inhibit tumor growth and hormone oversecretion, must also avoid damaging the residual normal pituitary gland and surrounding vascular and neural structures. To this end, Leenstra et al. (2010) emphasized the need to limit dose to the pituitary in order to preserve pituitary function, noting that endocrine deficits following radiosurgery were correlated with increasing dose to the gland. Adler et al. (2006) also noted the importance of dose homogeneity in the treatment of PA, specifically in cases in which the optic nerve is assumed to be attaining full dose. In general, for patients with surgically and medically refractory PA, high conformality and high homogeneity dose distributions offer local control while avoiding new pituitary or visual deficits (Iwata et al., 2011; Kajiwara et al., 2005; Yoon et al., 1998), achievable with the modulated orthovoltage SRS system.

2.4 Relevant previous work from other research groups

2.4.1 Modulated-fluence stereotactic cones

The work of Bender (2014) describes novel prototype collimation devices for linear accelerator cone-based SRS procedures. The collimation devices modulate standard cylindrical 4 mm, 6 mm, 8 mm, and 10 mm cones using concentric hypodermic needles of varying lengths and diameters. Machined plastic spacers were used for needle positioning, and the entire needle and spacer assembly was inserted into SRS linear accelerator cone applicators during irradiation. Examples of these inserts are shown in Figure 2.2.

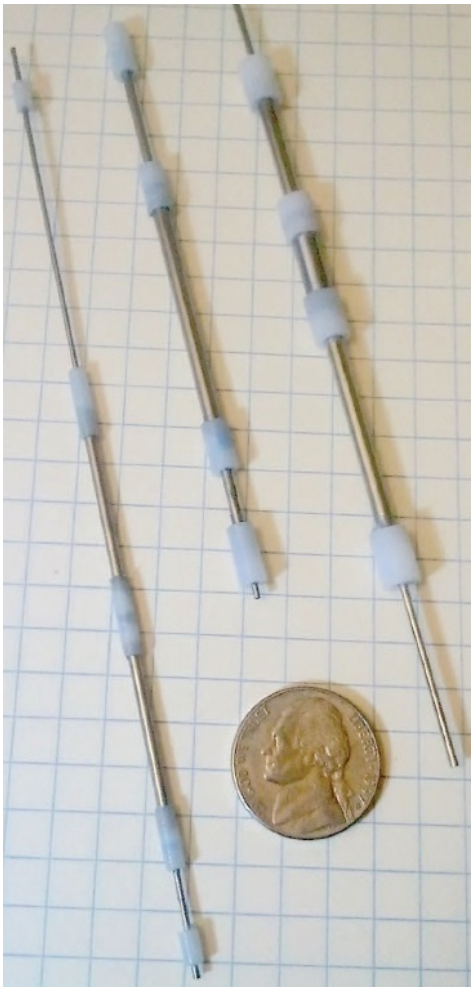

Figure 2.2: Photograph of the optimized needle inserts for 4 mm, 6 mm, and 8 mm cone collimators used by Bender (2014). For the 4 mm collimator, the optimized needle sizes are 15 and 20 gauge, for the 6 mm collimator the optimized sizes are 12, 16, and 20 gauge, and for the 8 mm collimator, the optimized sizes are 8, 12, and 18 gauge. Four machined plastic spacers are used on each assembly to allow concentric placement of the needles within the lead collimator. Reprinted with permission from E. T. Bender, "Increasing dose gradient and uniformity in small fields using modulation: Theory and prototypes for cone-based stereotactic radiosurgery," Medical Physics, 41, 051706, 2014. Copyright 2014, American Association of Physicists in Medicine.

Bender used a pencil-beam model for his optimization dose calculations, convolving a TERMA distribution with two distribution kernels, as shown in Equation 2.2.

$$\begin{aligned} K_{\text{total}}(x,y,z) &= \int_{-\infty}^{\infty}\int_{-\infty}^{\infty} K_{\text{source}}(x',y',z) \times K_{\text{PB}}(x-x',y-y',z)dx'dy', \\ D_{\text{s}}(x,y,z) &= \int_{-\infty}^{\infty}\int_{-\infty}^{\infty} T(x',y',z) \times K_{\text{total}}(x-x',y-y',z)dx'dy'. \end{aligned} \tag{2.2}$$

The quantity K_{source} is the kernel that describes the radiation source (a two-component Gaussian distribution model with one component for the source and one for head scatter), and the quantity K_{PB} is the kernel that describes the distribution of the radiation dose due to the transport of secondary particles, for which Bender used an analytical expression from the literature fitted to Monte Carlo data (Ahnesjö et al., 1992). Convolved together, these two kernels make up the total kernel, K_{total}, which is convolved with the TERMA distribution T to find dose to water D_{s} resulting from that distribution.

In order to calculate the optimal arrangement of the needles, numerical methods in MATLAB® (The MathWorks, Inc., Natick, MA) were used. The summed-square deviations were minimized between the resulting pencil beam-calculated dose distributions and the idealized rectangular function distributions, using the nominal diameters of commercially available hypodermic needles. Using these modulated cones to treat multi-isocenter plans (commonly done for non-ellipsoidal target geometries) results in hot spots that destroy the rectangular function distribution and eliminate the benefit of the modulation. However, the use of the cones with small, single isocenter cases, such as trigeminal neuralgia, as well as larger, ellipsoidal or spherical targets, may be a valuable application. Bender suggests that the cones represent a model system to explore the possibilities of beam modulation. Even if tertiary collimator systems using micro- or high-definition MLCs are capable of delivering single-isocenter, conformal plans for irregular targets, they do not approach the upper limit of the benefit of modulation.

2.4.2 Studies of ideal energy ranges for SRS and SBRT

2.4.2.1 Optimization of energy in inverse planning for extracranial targets

For some extracranial targets, low-energy beams have the ability to provide superior conformity around a target compared to high-energy beams, due to a decrease in lateral scatter. Low-energy beams also pose less risk of neutron dose, but may contribute a higher dose to peripheral normal tissue compared to high-energy beams. Morrill et al. (1990) discussed the optimization of various treatment parameters—including beam energy—using a constrained simulated annealing (CSA) technique and a treatment planning system developed in-house.

St-Hilaire et al. (2009) used "Ballista," their in-house aperture-based IMRT system, coupled with the Pinnacle^3 treatment planning system (Philips Radiation Oncology Systems, Fitchburg, WI) to investigate lung and prostate planning. St-Hilaire et al. added beam energy as an optimization parameter in Ballista, which also uses a CSA engine. Ballista's CSA engine optimizes beam geometry (table, gantry, collimator, and wedge angles), and the system uses a bound-constrained quasi-Newton (BCQN) engine to optimize beam weighting. The energy parameter was added as an "energy angle"—an independent degree of freedom for the CSA engine. They optimized plans with 6 MV beams, 23 MV beams, and mixed energy plans with one or two energies per incident beam angle. For multiple-energy optimization, each segment was duplicated at the two available energy levels, then assigned a weight determined with the BCQN engine. St-Hilaire et al. assigned each plan a cost function based on dose-volume metrics to quantify plan quality, and found that deep-seated targets could be treated with comparatively low (6 MV) energy beams without a decrease in plan quality. They also concluded that planning for targets in the lung could benefit from both high and low energies.

2.4.2.2 Modified CT scanner for non-coplanar lung SBRT

Deloar et al. (2004; 2006) modified a conventional CT scanner for use in lung SBRT using a cylindrical collimator. They modeled x-ray tubes of various energies (100, 200, 147.5, 200, 300, 400, and 500 kVp) using Monte Carlo techniques. They then used CT images of a thorax phantom and a human lung, converting CT values to physical densities with Monte Carlo, and calculated plans using three non-coplanar arcs over a range of kilovoltage energies (147.5, 200, 300, and 500 kVp) as well as more standard treatment energies in the megavoltage range (4, 6, and 10 MV). Deloar et al. then used a commercial treatment planning system to analyze the Monte Carlo-calculated dose-volume histograms (DVHs) and the maximum, minimum, and average dose values according to the International Commission on Radiation Units and Measurements (ICRU) Reports 50 and 62 (1993; 1999). The simulated system was compared to measured percent depth dose (PDD) values and profiles in water with two of the simulated kilovoltage energies (120 and 147.5 kVp). Measurements were taken with both a pinpoint ionization chamber and radiochromic film. Good agreement was found between the measured and simulated values, and the kilovoltage energy beams resulted in plans with superior DVHs and dose homogeneity over the plans generated with MV beams.

2.4.2.3 Intermediate energy SRS

A group from the Sunnybrook Health Center sought to find an optimal energy for delivery of intracranial SRS, exploiting the fact that, for SRS fields, the radiological penumbra is the dominating component of the overall penumbra, and for these fields the radiological penumbra is largely due to the range of secondary electrons produced by the primary photons. They reasoned that reducing the primary photon energy could result in improved dose gradients, conformality, and homogeneity. The group published a series of three papers describing their investigation. First, the group calculated the theoretical benefit of lower energies for SRS, comparing distributions from a single small field due to monoenergetic

photon beams from 100 keV to 1 MeV, in 100 keV increments, to a standard 6 MV photon beam (O'Malley et al., 2006). A formal optimization was not performed, but rather different monoenergetic photon energies were used with Monte Carlo simulations. As expected, they found sharper penumbrae with the lower energy beams compared to 6 MV. They then commissioned a virtual machine in Pinnacle treatment planning system with a low energy (800 kV, with a mean energy of 200–300 keV) and calculated treatment plans. They found DVHs with better conformality, homogeneity, and healthy tissue sparing for the 800 kV compared to the 6 MV beams.

The group then adjusted their linear accelerator hardware to approximate the beam simulated in the initial paper (Keller et al., 2007). They removed an electron scattering foil, replaced it with a tungsten target, and detuned the linear accelerator to arrive at a spectrum reasonably close to the theoretical beam. The end result was a photon beam in the ∼400 keV mean energy range, which they called a nominal 1 MV beam. They benchmarked their new beam against Monte Carlo, and measured small field penumbrae using film. The expected decrease in penumbrae was confirmed.

The group finally tested whether overlapping single beam penumbrae in a multiple-beam clinical treatment would blur the dose distribution and negate the advantages of using the low-energy beams (Keller et al., 2009). They also tested whether lowering the energy similarly to the first two studies would result in a clinically significant difference in treatment plans, or whether 6 MV plans, when treated in multiple non-coplanar arcs, would result in equivalent plans. The group compared film measurements in a LUCY 3D QA phantom (Standard Imaging, Inc., Middleton, WI) immobilized in a Brown-Roberts-Wells (BRW) stereotactic head frame for treatment plans created using XKnife^{TM} RT3 treatment planning system (Integra Radionics, Inc., Burlington, MA) with the 1 MV and standard 6 MV setups in a worst-case 18-field scenario using the modified linear accelerator. Improved homogeneity, conformality, and sharper gradients were found for the 1 MV setup.

2.5 Project goals

As discussed in Section 2.4, previous work has indicated that lowering the beam energy from the standard megavoltage range to the orthovoltage range results in the improvement of various plan quality metrics in SRS. Modulation of beam energy, even across a small field, may further serve to create ideal, homogeneous, conformal dose distributions in orthovoltage SRS delivery, but it has not been attempted. Such a system could be beneficial in a variety of SRS treatment applications, as discussed in Section 2.3. The goals of this project were to design, build, model, and characterize an optimized prototype modulated orthovoltage SRS system.

Chapter 3

Film dosimetry methods

3.1 UWMRRC resources

The UWMRRC has several resources of interest to this work related to film dosimetry. Monte Carlo and irradiator systems were both used extensively, and other resources of note are film scanning equipment and a comprehensive machine shop with computer numerical controlled (CNC) tools.

3.1.1 Constant potential kilovoltage x-ray irradiator

The UWMRRC constant potential kilovoltage x-ray system uses a Kimtron (Oxford, CT) Polaris 360 generator and a Comet (Flamatt, Switzerland) 320 tungsten anode tube, housed in a specially designed Hopewell Designs (Alpharetta, GA) tube stand. The target angle is 20°, and the nominal focal spot sizes are 3 mm (small) and 5.5 mm (large). The tube includes 1 mm inherent beryllium filtration, a 2 mm beryllium exit window, and may be additionally filtered using carefully fabricated filter packs consisting of combinations of aluminum and copper. A photograph of the x-ray tube as well as schematics of the tube stand are included in Figure 3.1.

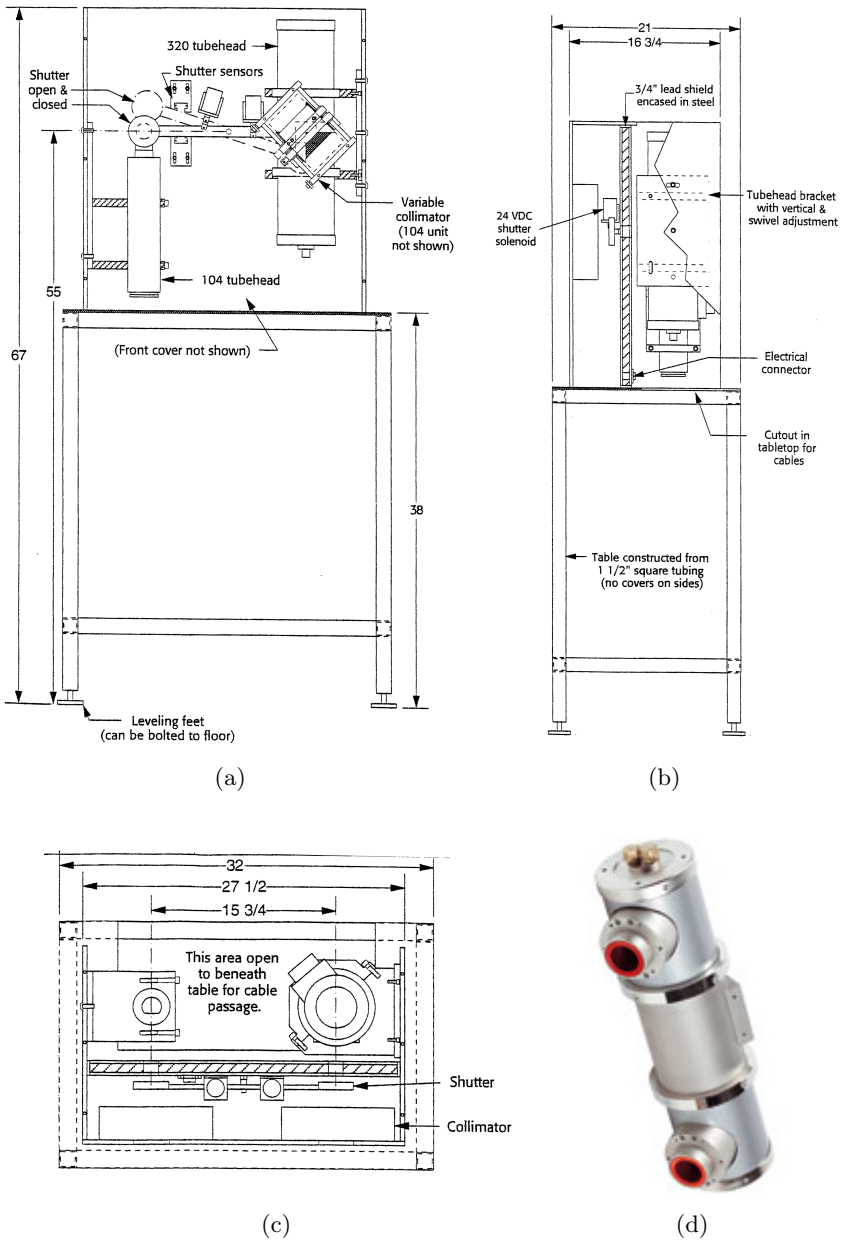

Figure 3.1: Schematics of the UWMRRC kilovoltage x-ray unit tube stand: (a) front view, (b) side view, and (c) top view; and (d) photograph of the Comet 320 tungsten anode tube, courtesy of the manufacturer.

The UWADCL uses beams from the UWMMRC orthovoltage unit that are carefully matched in terms of first half-value layer (HVL), homogeneity coefficient (HC), and tube voltage to corresponding beams at the National Institute of Standards and Technology (NIST). These beams are used as a secondary standard for NIST-traceable calibrations of therapy and diagnostic class ionization chambers. The beam used in this work, denoted using beam code UW250-M, is moderately filtered (M-series), with a tube peak voltage of 250 kVp. The beam has a first HVL of 18.3 mm aluminum, a homogeneity coefficient of 98, and an effective energy of 145 keV (Nunn et al., 2008). Its spectrum has been thoroughly characterized using Monte Carlo simulations and measurements with a low-energy germanium detector (Moga, 2011; Moga and DeWerd, 2010).

3.1.2 Monte Carlo resources

The UWMRRC maintains a high performance computing (HPC) cluster that runs Monte Carlo simulations via a parallelized CPU-based architecture. Most simulations for this work were performed on this cluster using the National Research Council of Canada's Electron Gamma Shower code, EGSnrc (Kawrakow, 2000a,b, 2005; Kawrakow et al., 2010). EGSnrc is a medical physics industry standard and was chosen for this work due to its superior modeling of electron transport physics. As first described by Berger (1963), Condensed History (CH) techniques simulate electron transport by grouping many electron interactions into a single step. A condensed history is sampled by allowing a given step to account for the sum of multiple collisions, and changes in energy and direction for each step are determined by multiple scattering theory probabilities. CH techniques, in turn, are classified as Class I or Class II schemes. Class I schemes use grouping for all events. For these schemes, secondary particle creation above a threshold value must be added retrospectively by the code, independent of "catastrophic" energy losses at any step. An event is deemed "catastrophic" if the particle loses a large fraction of its energy. Two examples of such events are bremsstrahlung processes that create photons with energies greater than a threshold k_c,

and inelastic collisions setting in motion atomic electrons with kinetic energies greater than threshold T_c (Chetty et al., 2007). The lack of correlation between energy loss and secondary particle creation is a disadvantage of Class I schemes, and is the reason a Class II-based code was chosen for this work, in which accurate electron transport is of interest. EGSnrc uses a Class II CH scheme, in which catastrophic events are not grouped into any single step, and the secondary particles above the chosen thresholds are explicitly transported (Kawrakow et al., 2010). The EGSnrc system employs a collection of user codes tailored to specific applications, which will be discussed in the relevant upcoming chapters.

Using the well-characterized spectrum described in Section 3.1.1, a full EGSnrc Monte Carlo model of the UWMRRC orthovoltage unit has been created using EGSnrc. This model was built using the EGSnrc user code BEAMnrc (Rogers et al., 1995), then extensively benchmarked and validated with ionization chamber and thermoluminescent dosimeter measurements in water (Lawless, 2016). The BEAMnrc model was used to create a phase space file immediately downstream of the beam's filter pack, or a file that contains information including particle position, charge, energy, weight, and direction, in a plane of interest (Ma et al., 1997). A rendering of the BEAMnrc model, including the x-ray tube, filtration, and collimation, is included in Figure 3.2.

3.2 Radiochromic film

There is a rich history of dosimetry using measured optical changes of materials caused by the induction of chemical interactions by radiation—see, for example, McLaughlin (1970) and Cameron (1967) for summaries. This work uses radiochromic film, a dosimeter in which coloration is induced directly by the absorption of energetic radiation, without requiring latent chemical, optical, or thermal development processes. The active layer(s) in the film contain radiosensitive monomers that react via solid-state polymerization upon irradiation with ionizing radiation, turning the film red or blue, depending on the configuration and presence of marker dyes (Niroomand-Rad et al., 1998; Williams and Metcalfe, 2011).

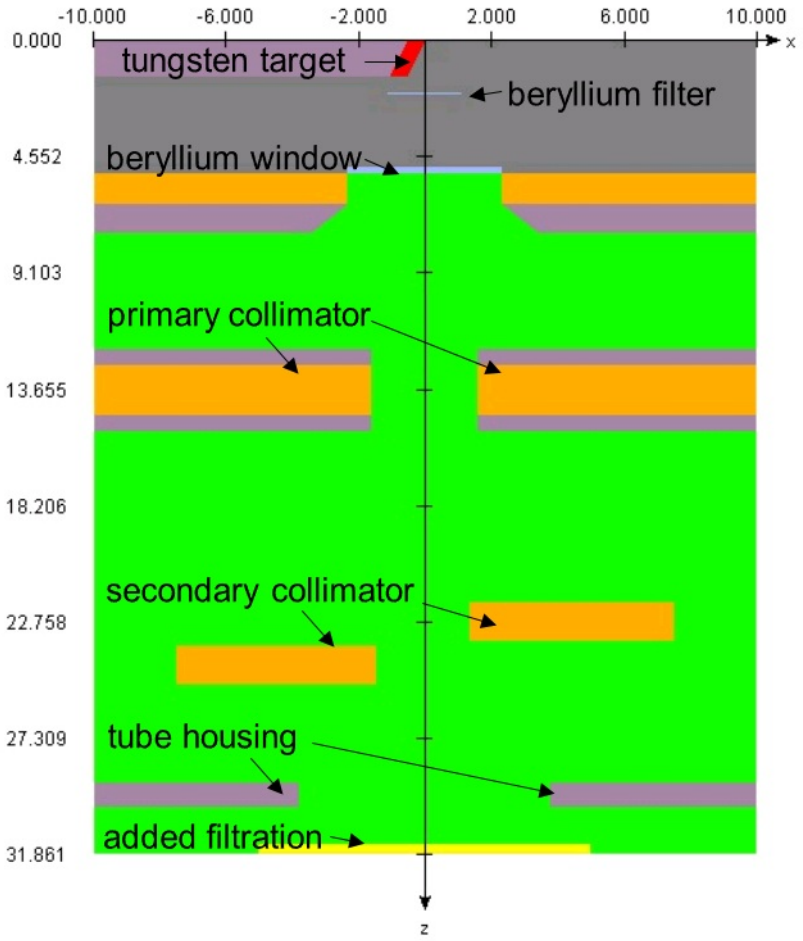

Figure 3.2: Rendering created in BEAMnrc of the UWMRRC Comet 320 tungsten anode x-ray tube, filtration, and collimation. Included dimensions are in centimeters. Model developed and validated by M. J. Lawless, "Development of kilovoltage x-ray dosimetry methods and their application to cone beam computed tomography," Ph.D. thesis, University of Wisconsin, Madison. Copyright 2016, Michael J. Lawless. Model used with permission.

Radiochromic film has been used in a diverse array of applications, including small animal irradiator characterization (Brady et al., 2009; Pidikiti et al., 2009), CT dosimetry (Brady et al., 2010; Tomic et al., 2010), ultraviolet dosimetry (Butson et al., 2000, 2010a), routine linear accelerator quality assurance and quality control (Antypas et al., 2015; Butson et al., 2008), proton and heavy ion dosimetry (Hara et al., 2014; Vatnitsky, 1997), brachytherapy applications for both high (Aldelaijan et al., 2010; Asgharizadeh et al., 2015) and low (Morrison et al., 2014; Schumer et al., 1999) dose rate delivery, and surface dose measurements (Butson et al., 1996, 1999). Ashland, Inc. (Covington, KY) manufactures an assortment of radiochromic films, known commercially as GafChromic® film, for a variety of radiotherapy applications. EBT3 film, the third generation of the External Beam Therapy line, is designed for IMRT patient plan verification. EBT3 film was chosen for this work due to its applicability for this project, most notably because radiochromic film boasts high spatial resolution and requires no development process (Podgorsak, 2005). EBT3 film has a wide, clinically relevant sensitive dose range of 1 cGy–40 Gy, per manufacturer specifications, and may be cut to shapes and sizes of interest. Its near tissue-equivalence and low energy response in the relevant orthovoltage energy range have been previously studied and characterized at the UWMRRC (Rosen, 2015).

Radiochromic film's active layer contains organic molecules called diacytelene monomers, containing two carbon-carbon triple bonds and end groups that affect the packing of the monomers within the crystal lattice (which in turn affect film sensitivity). Absorption of ionizing radiation causes the monomers to undergo a polymerization reaction to reach a lower-energy state (Figure 3.3). The resulting diacetylene polymer chains are colored, allowing radiation dosimetry by measurement of optical properties of the film (Williams and Metcalfe, 2011). The EBT film models contain an active layer using the lithium salt of pentacosa-10,12-diynoate (LiCDA) as the active monomer grown in a "hair-like" configuration (Reinhardt et al., 2012; Rink et al., 2008). Following polymerization, the resulting diacetylene chains turn the film progressively darker blue with increasing dose. Spectropho-

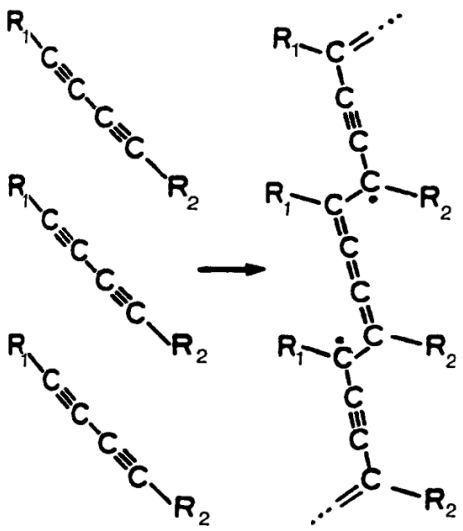

Figure 3.3: Radiation causes microcrystalline diacytelene monomers in radiochromic film to undergo a 1,4 polymerization, resulting in formation of blue polymer chains. End groups are denoted R_1 and R_2. Reprinted with permission from W. L. McLaughlin et al., "Radiochromic solid-state polymerization reaction," in Irradiation of Polymers, ACS Symposium Series. Copyright 1996, American Chemical Society.

tometer measurements have indicated the film has two absorption maxima in the red range of the visible light spectrum, with a primary absorption peak at a wavelength of 636 nm (Butson et al., 2009).

The EBT line has undergone three major geometric iterations: EBT, EBT2, and EBT3 (shown in schematic in Figure 3.4). The original model, EBT, is no longer commercially produced. It was composed a thin surface layer interposed between two symmetric active layers, surrounded by two symmetric layers of protective polyester substrate. The next model, EBT2, is asymmetric, and is composed of an active layer and an adhesive layer, surrounded by two layers of clear polyester substrate of unequal thickenesses. A yellow marker dye was incorporated into the active layer (Borca et al., 2013). The most recent model, EBT3, returns to a symmetric configuration, and is structured as an active layer, nominally 25 µm thick, between two symmetric layers of matte polyester laminate, nominally 125 µm thick (Bekerat et al., 2014).

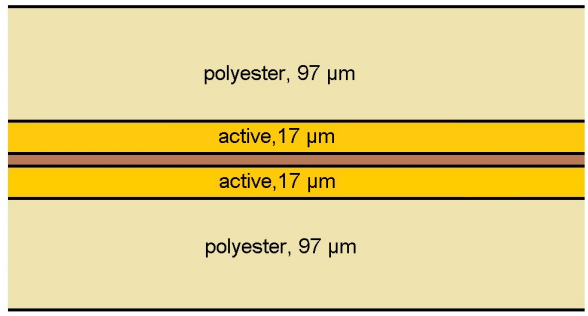

(a)

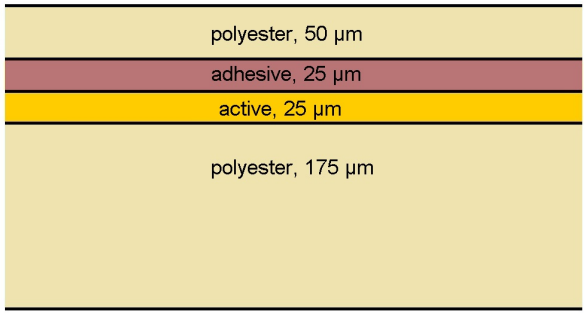

(b)

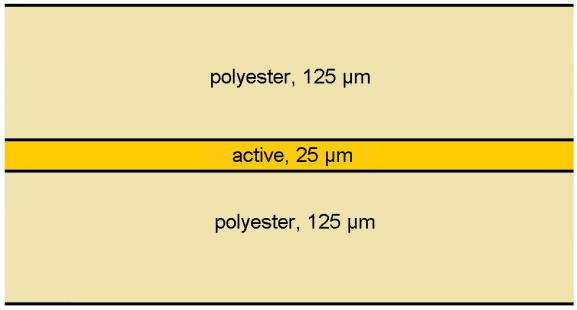

(c)

Figure 3.4: Cross sections of the GafChromic External Beam Therapy line films are shown in schematic for the (a) EBT, (b) EBT2, and (c) EBT3 models.

In addition to the three major geometric configuration model changes, the chemical compositions of the active and structural layers have also been changed (including composition changes within each model). The different versions of the EBT films are summarized in Table 3.1, with stated Z_{eff} values reported by Bekerat et al. (2014) and Rosen (2015). Based on energy response studies (Bekerat et al., 2014), the most recent commercially released version of EBT3 (denoted EBT3-V3) removed the previously included elements nitrogen, sodium, silicon, chlorine, and bromine, and included approximately 7% aluminum. All film measurements included in this work were completed using EBT3-V3.

3.3 Basic film handling methods

Radiochromic film offers many positive characteristics; however, accurate dosimetry requires consistent and meticulous film handling methods as described by the recommendations of the AAPM Radiation Therapy Task Group 55 (Niroomand-Rad et al., 1998).

Latex gloves were worn at all times while handling film to minimize surface contamination. Tweezers and vacuum pickup tools were used for the majority of film handling. All film was from a single batch of the most recent iteration of EBT3 (Lot 11051301). To reduce the effects of ambient light (Andrés et al., 2010; Butson et al., 1998, 2003), films were stored in opaque envelopes at all times when not in use. Temperature and humidity have been shown to affect film response (Girard et al., 2012; Lynch et al., 2006; Rink et al., 2008; Williams and Metcalfe, 2011), so films were stored together in a temperature- and humidity-controlled environment to ensure that all films had a similar thermal history, and environmental conditions were documented during irradiation. Storage and irradiation conditions were consistent with manufacturer recommendations.

Films were cut into segments using sharp scissors to minimize layer separation as recommended by Soares (2006) and Moylan et al. (2013), and film analyses discarded data at least

Table 3.1: Composition of active layers of EBT (Lot 48022-07I), EBT2 (Lot A06161006), EBT3-V1 (Lot A07251102), EBT-V2 (Lot A051512-01), and EBT-V3 (Lot 11051301) and the EBT3 polyester substrate, in mass percent. From Bekeret et al. (2014) and Rosen (2015).

	H	Li	C	N	O	Na	S	Cl	Br	Al	Z_{eff}	Density $\left(\text{g/cm}^3\right)$
EBT	9.4	0.8	57.6	13.2	16.4	-	-	2.6	-	-	6.98	1.1
EBT2	9.7	0.9	58.4	0.1	28.4	0.4	0.2	1.1	0.8	-	9.38	1.2
EBT3-V1	9.7	0.9	58.4	0.1	28.4	0.4	0.2	1.1	0.8	-	9.38	1.2
EBT3-V2	8.9	1.0	61.3	0.1	23.5	0.5	0.01	4.5	-	0.1	7.99	1.2
EBT3-V3	8.8	0.6	51.1	-	32.8	-	-	-	-	6.7	7.26	1.2
EBT3 polyester substrate	4.0	-	63	-	33	-	-	-	-	-	6.64	1.35

1.5 mm from film edges as recommended by AAPM TG 55 (Niroomand-Rad et al., 1998). Klassen et al. (1997) noted stress on the film can affect film response immediately after cutting, and therefore all film segments were cut at least 48 hours prior to use. Radiochromic film polymer chains have a preferred orientation, and therefore an orientation-dependent film response has been noted during the digitization process (Dreindl et al., 2014; Fuss et al., 2007; Klassen et al., 1997; Saur and Frengen, 2008; Zeidan et al., 2006). To ensure consistent alignment of films, segments were immediately marked with numbered fiducials after cutting using a fine-tipped permanent marker to record orientation of the segment with respect to the original sheet. Though film response dependence on film side has been shown to be minimal due to the film's symmetric construction (Borca et al., 2013; Reinhardt et al., 2012), marking the film also ensured consistent alignment with respect to film side.

Samples were cut from randomized positions on film sheets in an effort to reduce effects of film nonuniformity (Reinhardt et al., 2012). The smallest segment film dosimeter used in this work was $(1 \times 1)\,\mathrm{cm}^2$. This was deemed acceptable after consulting the work Moylan et al. (2013), who used a one-way ANOVA analysis to compare films cut to sizes (0.5×0.5), (1×1), (2×2), and $(4 \times 4)\,\mathrm{cm}^2$, and found no measurable difference in film response when edge effects were discarded.

Manufacturer documentation indicates that EBT3 film may be used for in-water measurements, though a thorough characterization of effects of water immersion on EBT3 film has not yet been published. Known humidity effects for EBT3 as well as water penetration at film edges for EBT2 film were of concern for in-water measurements. Aldelaijan et al. (2010) found that short immersion times (approximately 30 minutes) have negligible effect on the change in film optical density (OD) for EBT2 film. However, they did find that as immersion times increase, anticipated dose error can reach 7% for a 3 Gy irradiation, and water penetration effects were noted up to 9 mm at film edges. To avoid these effects, all film samples were placed within vacuum-sealed, air-tight Foodsaver® (Sunbeam Products, Inc., Boca Raton, FL) bags, as described by Rosen (2015), Soares (2009), and Massillon et

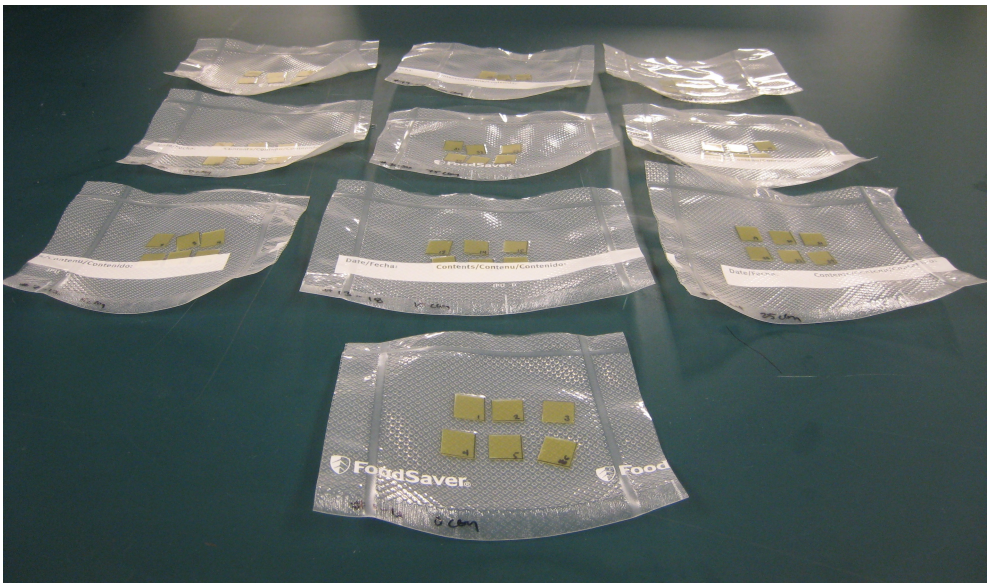

Figure 3.5: Photograph of film samples that were cut and placed in vacuum-sealed, air-tight bags using a commercially available food vacuum sealer.

al. (2013). Film segments cut for calibration irradiation and placed in bags are pictured in Figure 3.5.

Film response following irradiation has been investigated previously for radiochromic film. The initial color autodevelopment of the film, occurring within a few microseconds following radiation, results in the majority of the color development (McLaughlin et al., 1996). Color development continues at an ever-decreasing rate (Cheung et al., 2005; Devic et al., 2010; Niroomand-Rad et al., 1998; Zeidan et al., 2006). Dreindl et al. (2014) found that for a 22-hour interval following irradiation and prior to scanning of EBT3 film, a change of 0.35% was introduced in OD per hour change in interval time, for the dose level at which the effect was the most pronounced (30 cGy). Borca et al. (2013) found variations in net optical density (netOD) in EBT3 measurements between 2.1% and 4.3%, between one and 24 hours following irradiation, and between two and 24 hours changes in netOD were <0.008, for variations in OD $<2.5\%$ for all doses. For doses <2 Gy, netOD stabilized after approximately 30 minutes. For all post-irradiation read-out in this work, film samples were

scanned at least seven days following exposure to assure full development and to minimize change in film response due to small variations in development duration.

3.4 Film scanning

3.4.1 EPSON Expression 10000XL white light flatbed scanner

All flatbed scanning was completed with an EPSON Expression® 10000XL white light flatbed document scanner, S/N 026388 (Epson America, Long Beach, CA) and its associated software, EPSON Scan v.2.20A. All images were acquired in transmission mode and landscape orientation with the film elevated from the glass and positioned in the center of the scan window using a polycarbonate frame. Professional mode was used with all image correction methods, color corrections, and adjustment features turned off, with a scanning resolution of 300 dpi. All images were digitized as 48-bit color depth RGB images (16 bits per color channel), and saved in uncompressed tagged image file format (TIFF).

For all flatbed scanner measurements, five warm-up scans were taken during each scanning session, and then the scanner was allowed to warm up for approximately 30 minutes with the upper transparency raised to ensure stable and reproducible scanner temperature during read out (Devic et al., 2005; Ferreira et al., 2009; Gill and Hill, 2013; Paelinck et al., 2007; Reinhardt et al., 2012; Saur and Frengen, 2008). Though some film methodologies use the averaging of multiple scans of film dosimeters and discarding the initial scans to avoid the warm up effect (Devic et al., 2005; Saur and Frengen, 2008), it was deemed preferable to warm up the scanner consistently prior to film scanning to avoid scanning the film multiple times, which has been shown to affect film response (Martišìkovà et al., 2008; Paelinck et al., 2007).

Films were scanned in landscape orientation, as recommended by the manufacturer. Due to the "hair-like" structure of the monomers (Section 3.2) as well as a preferential orientation of the polymer chains, incident light scatters anisotropically from the film, resulting

in a difference in response based on scan direction (Carrasco et al., 2013; Fuss et al., 2007; Reinhardt et al., 2012). Borca et al. (2013) found a difference of up to 4.5% in netOD between portrait and landscape scanning positions. Consistency in film alignment is therefore important for dosimetric accuracy. Here, "landscape" indicates that the original short side of the film (as determined prior to cutting) is parallel to the long side of the scanner (along the scan direction).

The lateral response artifact (LRA) was of concern for flatbed scanning dosimetry measurements. Along the direction perpendicular to the scan direction, a transmittance decrease has been noted with increasing distances from the center of the light source (Crijns et al., 2013). Nonuniformity of the scanner light source as well as light scattering within the scanner can result in a difference in OD measurement based on film position within the scan window (Lewis and Chan, 2015). To minimize LRA, Lynch et al. (2006) recommend using only the central region of the scanner, where the effect is limited. Therefore, care was taken to position film dosimeters by using the polycarbonate frame as well as custom-made acrylonitrile butadiene styrene (ABS) holders to position films reproducibly in the center of the scan window. One holder consists of 47 circular holes, 1 cm in diameter, and the other consists of 15 openings to accommodate the $(4 \times 4)\,\mathrm{cm}^2$ film segments. The scanning set-up is pictured in Figure 3.6. As recommended by Paelinck et al. (2007), each scan was taken over the entire scan field, even if the film dosimeter was a small fraction of the total field.

In addition to positioning the film reproducibly at the desired scanning position, the ABS holder also served to raise the film a small amount from the scanner glass. Very thin, variable air gaps between the film and scanning glass surface may cause a non-reproducible interference pattern, known as Newton's rings (Butson et al., 2003) when the film is placed directly on the scanning surface. Newton's rings artifacts can result in variations of measured optical density, and therefore can lead to uncertainty in subsequent dosimetry. To prevent these artifacts, it was recommended that previous models of EBT film be scanned using templates, frames, or holders to elevate the film slightly to avoid direct scanner-film contact

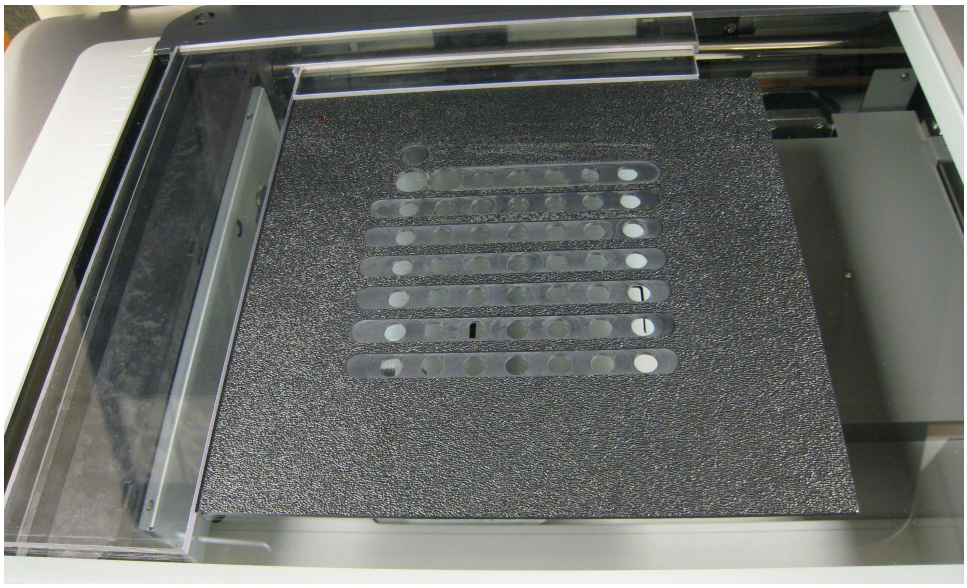

(a)

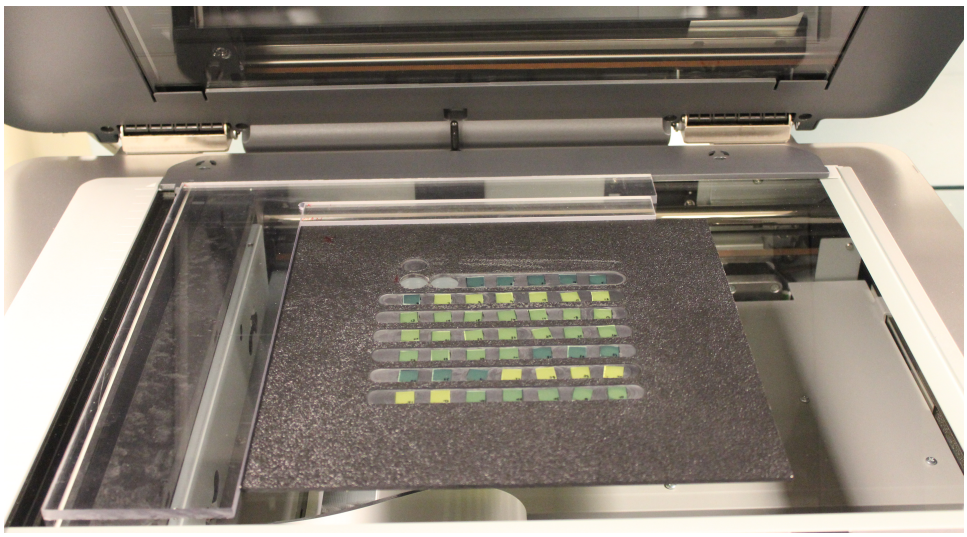

(b)

Figure 3.6: Photograph of the EPSON Expression 10000XL white light flatbed document scanner (a) with the polycarbonate frame and an empty ABS film holder used to position film dosimeters reproducibly in the center of the scan bed. In this orientation, the scanning direction is from left to right. The ABS holder is shown (b) with 47 irradiated $(1 \times 1)\,\mathrm{cm}^2$ film segments in place for scanning.

(Kairn et al., 2010). The current model of EBT film, EBT3, contains a matte polyester substrate with silica treatment on both sides of the active layer. The silica particles introduce a <5 µm gap to the scanner glass, thus minimizing the formation of interference patterns (Dreindl et al., 2014). Although EBT3's film configuration minimizes the formation of Newton's ring artifacts, Moylan et al. (2013) measured EBT3 film response both directly on the scanner glass and raised 0.25 mm using a template. They found a higher standard deviation (2.1%) in film response for the film placed directly on the glass, compared to film raised above the glass (1.2%), and recommended that film be scanned raised a minimal amount above the scan bed.

Previous models of EBT film have shown to be most sensitive using the red channel (Fiandra et al., 2006). Devic et al. (2009) studied optimal dose ranges per color channel for EBT film, and found the red channel was optimal for 0–4 Gy measurements, the dose range for this work. EBT3 similarly exhibits highest absorbency at 636 µm (Sorriaux et al., 2013), and has been shown to be most sensitive in the red channel over a dose range of 0–7 Gy (Borca et al., 2013), and therefore all analyses of flatbed images were completed using the extraction of red channel data.

A scanning resolution of 300 dpi was chosen for this work. Although previous EBT3 publications have used scanning spatial resolutions ranging from 72 to 150 dpi (Borca et al., 2013; Crijns et al., 2013; Evgeniia et al., 2015), Massillon-JL et al. (2012) examined EBT3 response based on scanning resolution. They found that for a given absorbed dose, the degree of energy dependence of the film is lowered with increased spatial resolution. They also concluded that although spatial resolution of 75 dpi is sufficient for most external beam applications, 300 dpi was preferable for measurements including small field SRS, SBRT, and brachytherapy applications to measure regions of high dose gradient accurately.

For each film-scanning session, an open region of the scan bed, as well as neutral density filters with known OD values, were scanned at the beginning of the session and at the end of the session to monitor scanner drift. Also during each session, a scan of a black, opaque

paperboard cut to cover the entire scanning window (aside from the calibration strip) was obtained to quantify background scanner signal.

Film positioning reproducibility was quantified using the ABS holder and polycarbonate frames. Ten scans were taken, with the entire frame set-up removed from the scan bed and the upper transparency lowered and re-raised between each scan. The position of the ABS holder corner differed by at most 1 pixel between the scans, approximately 0.085 mm for the given scanning resolution.

The empty holder was scanned ten times in the center of the scan window to test variability of response as a function of the 47 film slots used on the ABS holder. The average pixel value was found for central, 6 mm-diameter circular regions of interest defined for each of the film slots in the ABS holder. Of the ten scans, the maximum variability of mean pixel value between film slots within any single scan was found to be 0.49%.

3.4.2 UWMRRC prototype Laser Densitometry System

A prototype laser densitometry system (LDS) traceable to primary optical standards was developed at the UWMRRC (Rosen, 2015; Rosen et al., 2015). This system uses point measurements of a diode laser through film suspended in air. The laser is nominally 8 mW power and 635 nm wavelength, and is coupled to a high-sensitivity photodiode to quantify voltage collected following laser transmission though a target. This system was optimized for accurate dosimetry (in contrast to commercially available scanning laser densitometers optimized for throughput), and has been extensively characterized. Its unique construction was designed to mitigate issues with conventional film scanners, such as LRA, film/glass surface interference artifacts, and a low signal-to-noise ratio. Previous work has shown the LDS to achieve superior results for quantitative radiochromic film dosimetry based on physical models of film response compared to standard white light, flatbed document scanners or scanning laser densitometers (Rosen, 2015). Access to the UWMRRC LDS offered the opportunity to compare flatbed data to this innovative new technology.

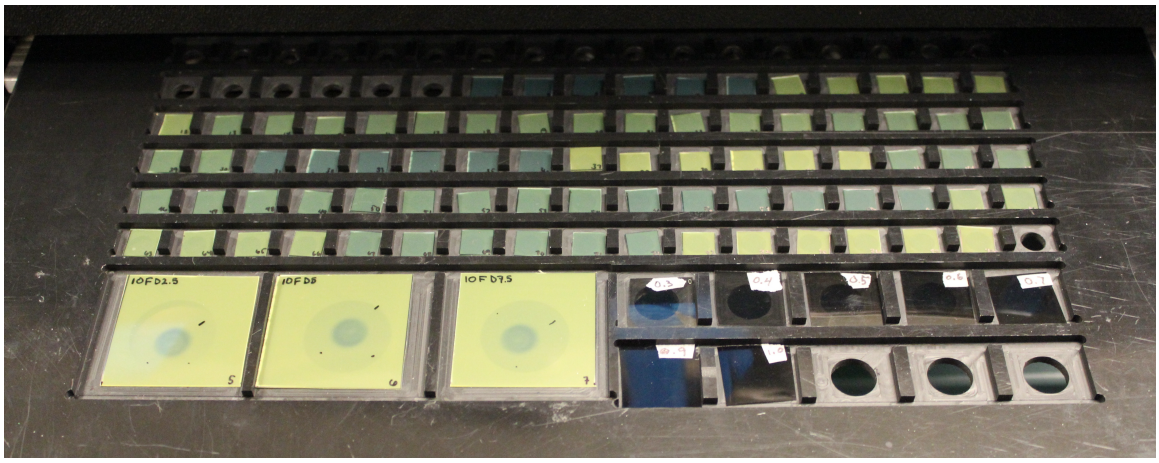

Figure 3.7: Photograph of irradiated EBT3 film dosimeters in (1×1) and $(4 \times 4)\,\mathrm{cm}^2$ segment sizes in a custom ABS film holder along with the known optical density filters prior to insertion into the LDS for scanning.

Similar to the EPSON measurements, film segments were scanned in the LDS were placed in a consistent orientation using a custom ABS film holder, designed to accommodate and reproducibly position both (1×1) cm^2 and (4×4) cm^2 segment sizes free in air (Figure 3.7). Consistent film orientation with the LDS is particularly important: polarization response may be significant based on orientation due to the use of polarized light with a dosimeter with a noted preferred orientation of radiochromic film polymer chains (Rosen, 2015). To quantify system stability, all scans included at least one empty cell at both the beginning and the end of the scan. Additionally, a set of NIST-traceable OD filters were included with every scan in order to create a voltage-to-OD linear calibration for each scan and therefore account for any system drift over time (Matrosic et al., 2016; Rosen et al., 2015). A scanning resolution of 100 µm was used for all LDS measurements in this work.

3.5 Film energy response

The latest version of EBT3 contains an active layer that is relatively water equivalent (Table 3.1), such that the dose absorbed in its active layer from incident high-energy photons is similar to the dose that would be deposited in an equivalent volume of water (Lindsay

et al., 2010). In the orthovoltage energy range, this water equivalence approximation begins to break down due to the differences in film active layer composition layer compared to water, and this absorbed-dose energy response can be taken into account using either analytical calculations or Monte Carlo techniques (Sutherland and Rogers, 2010; Villarreal-Barajas and Khan, 2014). In addition to absorbed-dose energy dependence, an intrinsic energy response has been reported for radiochromic film models (Bekerat et al., 2014) as well as other solid-state and chemical dosimeters (Anton and Büermann, 2015; Davis et al., 2003; Nunn et al., 2008; Reed et al., 2014). For radiochromic film, this intrinsic effect is likely due to solid state processes that are not taken into account in a Monte Carlo absorbed-dose energy dependence determination, such as the polymerizing efficiency within the active layer (Hermida-López et al., 2014). The absorbed-dose and intrinsic energy dependence together can be used to determine the total energy dependence of a dosimeter, which has been studied for radiochromic film models (Brown et al., 2012; Butson et al., 2010b; Ebert et al., 2009; Rink et al., 2007). Hammer et al. (2017) and Rosen (2015) quantified the absorbed-dose, intrinsic, and total energy dependence of the most recent iteration of EBT3 film, the iteration that was used in this work. The work of Hammer et al. is currently in preparation. Here, the intrinsic response is defined as follows:

$$k_{\mathrm{bq}} = \frac{M_{\mathrm{film}}(Q)}{D_{\mathrm{film}}(Q)}, \tag{3.1}$$

where a radiation beam of some beam quality Q results in the absorbed dose to film, $D_{\mathrm{film}}(Q)$, and $M_{\mathrm{film}}(Q)$ is the measured film response, noting that k_{bq} is defined here inversely compared to Sutherland and Rogers (2010), Bekerat et al. (2014), and Hermida-López (2014). The absorbed-dose energy response is defined as follows:

$$f(Q) = \frac{D_{\mathrm{med}}(Q)}{D_{\mathrm{film}}(Q)}, \tag{3.2}$$

where $D_{\mathrm{med}}(Q)$ is the absorbed dose in a reference medium for the same beam quality. A reference beam quality, Q_{ref}, delivers the same dose as the beam quality Q to the medium, and may be used to define the relative absorbed-dose energy response, $f_{\mathrm{rel}}(Q)$:

$$f^{\mathrm{rel}}(Q) = \frac{f(Q)}{f(Q_{\mathrm{ref}})} = \frac{D_{\mathrm{med}}(Q)/D_{\mathrm{med}}(Q_{\mathrm{ref}})}{D_{\mathrm{film}}(Q)/D_{\mathrm{film}}(Q_{\mathrm{ref}})}. \tag{3.3}$$

The total energy dependence of the film, $S(Q)$, is defined as follows:

$$S(Q) = \frac{k_{\mathrm{bq}}(Q)}{f(Q)} = \frac{M_{\mathrm{film}}(Q)}{D_{\mathrm{med}}(Q}. \tag{3.4}$$

Finally, the relative total energy dependence, $S^{\mathrm{rel}}(Q)$, is defined as follows:

$$S^{\mathrm{rel}}(Q) = \frac{S(Q)}{S(Q_{\mathrm{ref}})} = \frac{M_{\mathrm{film}}(Q)/M_{\mathrm{film}}(Q_{\mathrm{ref}})}{D_{\mathrm{med}}(Q)/D_{\mathrm{med}}(Q_{\mathrm{ref}})}. \tag{3.5}$$

Thirteen NIST-matched kilovoltage beams used by the UWADCL from the UWMRRC orthovoltage unit (Section 3.1.1), ^{137}Cs, and ^{60}Co, were used in that work to evaluate k_{bq}, f^{rel}, and S^{rel} for EBT3-V3 film. The intrinsic energy response was measured directly, and the absorbed-dose energy response was calculated using Monte Carlo methods. A summary of their findings is included in Table 3.2 and Figure 3.8. Considering these results, adding thicknesses of attenuating material to the UW250-M beam will result in beam hardening (as discussed in Section 5.1.1), though to a low enough degree that any change in energy response of the film within a modulated field is within the uncertainty of the energy response determination.

Table 3.2: Intrinsic, absorbed-dose and total energy response of EBT3-V3 relative to ^{60}Co, determined by Hammer et al. (2017). Uncertainty fork_{bq} values is the standard deviation of the measured mean film response. Uncertainty in f^{rel} values is the propagated statistical uncertainty from Monte Carlo simulations at the $k = 1$ level, and uncertainty in S^{rel} values is the uncertainties from k_{bq} and f^{rel} values added in quadrature.

Effective energy (keV)	UWMRRC beam quality	Intrinsic energy response (k_{bq})	Absorbed-dose energy response (f^{rel})	Total energy response (S^{rel})
11.5	UW-20M	0.822 ± 1.9%	0.988 ± 0.3%	0.812 ± 1.9%
15.5	UW-30M	0.898 ± 1.6%	0.977 ± 0.4%	0.877 ± 1.6%
19.8	UW-40M	0.934 ± 2.1%	0.974 ± 0.4%	0.910 ± 2.1%
22.4	UW-50M	0.954 ± 1.6%	0.972 ± 0.5%	0.928 ± 1.7%
26.9	UW-60M	0.973 ± 2.2%	0.965 ± 0.6%	0.939 ± 2.3%
32.7	UW-100L	0.957 ± 1.5%	0.960 ± 0.7%	0.918 ± 1.6%
33.5	UW-80M	0.958 ± 1.2%	0.956 ± 0.8%	0.916 ± 1.4%
42.1	UW-100M	0.959 ± 1.9%	0.954 ± 0.8%	0.915 ±2.1%
49.9	UW-120M	0.941 ± 1.2%	0.946 ± 0.8%	0.890 ± 1.5%
67.0	UW-150M	0.934 ± 0.9%	0.950 ± 0.7%	0.887 ± 1.1%
88.6	UW-100H	0.947 ± 0.8%	0.960 ± 0.7%	0.909 ± 1.1%
99.8	UW-200M	0.947 ± 2.2%	0.971 ± 0.7%	0.920 ± 2.3%
145	UW-250M	0.966 ± 2.1%	0.993 ± 0.8%	0.959 ± 2.3%
662	^{137}Cs	1.000 ± 1.8%	1.009 ± 0.4%	1.009 ± 1.9%

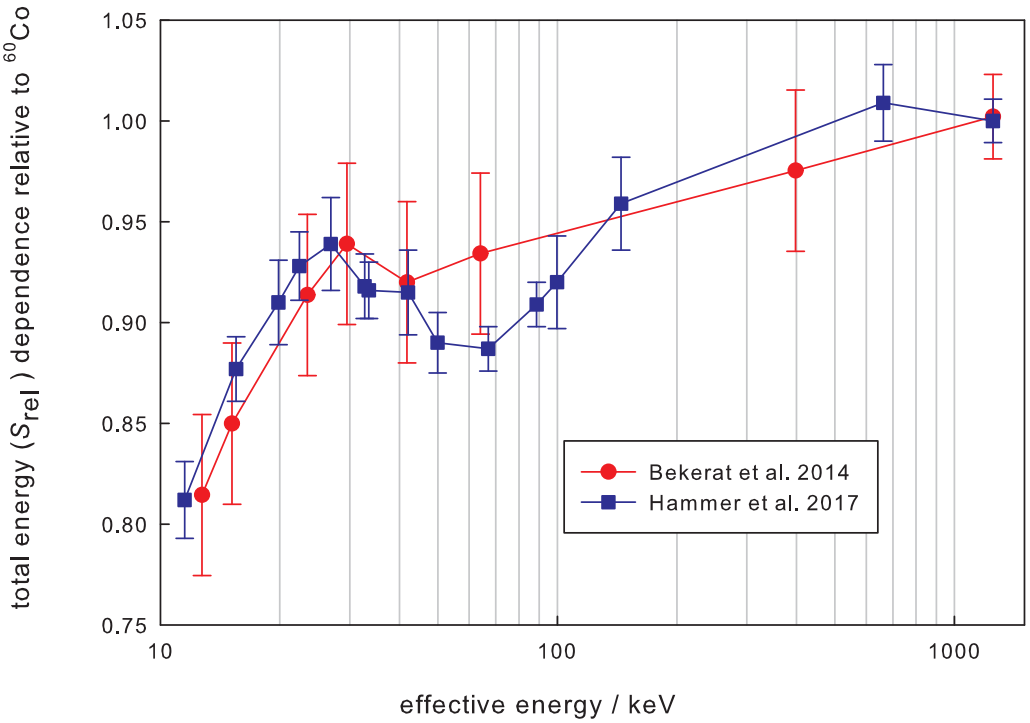

Figure 3.8: Comparison of the Hammer et al. (2017) results of the total energy response relative to ^{60}Co for EBT3-V3 to those of Bekerat et al. (2014) for similar beams. Error bars for Hammer et al. represent uncertainty from intrinsic and absorbed-dose uncertainties added in quadrature, and error bars for Bekerat et al. represent the uncertainties listed in that publication.

3.6 Film calibration

3.6.1 Film response models

Transmission of light through an absorbing material is dependent on material thickness, wavelength- and temperature-dependent optical constants of the material, and angle of incidence and polarization of the incoming light (Zhang et al., 1997). If ρ is the reflectance (dependent on the real part of the material's index of refraction), and τ is the internal transmittance (dependent on material thickness, light wavelength, and the imaginary part

of the material's index of refraction), then the external transmittance, T, may be written as follows:

$$T = (1 - \rho)^2 \tau. \tag{3.6}$$

The optical density quantifies the ability of the medium to transmit light, and is defined:

$$OD = -\log_{10} T. \tag{3.7}$$

In the case of film, OD is defined as the common logarithm of the ratio of light transmitted through a densitometer with no film present, I_0, to the light transmitted through a film, I:

$$OD = \log_{10} \left(\frac{I_0}{I} \right). \tag{3.8}$$

A decrease in transmitted light through the film (either by reflection or absorption) is indicated by an increase in optical density. Subtracting the OD of an unirradiated film from an irradiated film increases the precision of radiochromic film dosimetry (Paelinck et al., 2007). Of interest to film dosimetry is the quantity net optical density:

$$netOD = OD_{\text{exposed}} - OD_{\text{unexposed}}, \tag{3.9}$$

where $OD_{\text{unexposed}}$ and OD_{exposed} represent the optical densities of the film before and after exposure, respectively (Devic et al., 2004; Williams and Metcalfe, 2011). If unirradiated control films are used, the quantity ΔnetOD may be defined:

$$\begin{aligned} \Delta netOD &= netOD - netOD_{\text{control}} \\ &= (OD_{\text{exposed}} - OD_{\text{unexposed}}) - (OD_{\text{control, after}} - OD_{\text{control, before}}) \end{aligned}, \tag{3.10}$$

where $netOD_{\text{control}}$ is the net optical density of the control films, and $OD_{\text{control, before}}$ and $OD_{\text{control, after}}$ represent the optical density of the control films before and after exposure of the experimental films, respectively (Aldelaijan et al., 2010). To relate Equation 3.10 to

averaged pixel value (over a central region of interest, or ROI), $\Delta netOD$ may be written:

$$\Delta netOD = \log_{10}\left(\frac{PV_{\text{unexposed}} - PV_{0,\,\text{before}}}{PV_{\text{exposed}} - PV_{0,\,\text{after}}}\right) - \log_{10}\left(\frac{PV_{\text{control,\,before}} - PV_{0,\,\text{before}}}{PV_{\text{control,\,after}} - PV_{0,\,\text{after}}}\right), \tag{3.11}$$

where measured pixel values are abbreviated as $PV_{\text{unexposed}}$ for the unexposed film, PV_{exposed} for the exposed film, $PV_{\text{control,\,before}}$ for the control film before exposure of the experimental films, $PV_{\text{control,\,after}}$ for the control films after exposure of the experimental films, $PV_{0,\,\text{before}}$ for the background scanner signal measured before exposure of the experimental films, and $PV_{0,\,\text{after}}$ for the background scanner signal measured after exposure of the experimental films (Devic et al., 2005; Devic, 2011; Fiandra et al., 2006; McCaw, 2015; Sorriaux et al., 2013). Imaging processing and analysis was completed using MATLAB to extract average pixel values from a central ROI.

All film was calibrated in the center of $(10\times10)\,\text{cm}^2$ well-characterized, uniform radiation fields, which were large in comparison to film size. The UWADCL holds a NIST-traceable secondary standard for air kerma in the UW250-M x-ray beam, a $3.6\,\text{cm}^3$ active volume spherical Exradin model A3 chamber (Standard Imaging, Inc., Middleton, WI). The air-kerma rate was measured using the secondary standard ionization chamber, and Monte Carlo techniques were then used to calculate absorbed dose-to-water per unit air kerma, both in air and at 5 cm depth in water at 100 cm from the source, in a source-to-axis distance (SAD) irradiation geometry.

A variety of models have been proposed to relate film response to either dose-to-film or dose-to-water (here, dose will be denoted D, and various constants in these models will be denoted a, b, c, and d). One of these original models was inspired by analytical expressions describing radiographic film response, in which radiation interacts with microscopic silver halide grains (usually AgBr) to form a latent image on radiographic film. The latent image is then reduced and fixed into a usable image through a chemical development process. The model is based on the basic assumptions that all grains have the same probabilistic area

of interaction, that there is a uniform distribution of grains dispersed on the film surface, and that a single hit by a particle is sufficient to render a grain developable (Kathren, 1987; Shani, 1991; Yeo and Kim, 2004). This "single hit" model has been used to describe radiochromic as well as radiographic film response (van Battum and Huizenga, 2006; Rosen, 2015):

$$netOD = OD_{\max}\left(1 - e^{-aD}\right). \tag{3.12}$$

Here, $netOD$ is related to the optical density at saturation (a theoretical maximum optical density resulting from infinite dose) as well as a measure of film sensitivity.

A very different format is suggested by Azorín et al. (2014) and Lewis et al. (2012), who use an invertible, rational function:

$$netOD = a + \frac{b}{D - c}. \tag{3.13}$$

The authors point out that the function is monotonic and does not require large numbers of calibration points to create a calibration curve in a dose region of interest, unlike some models. Further, calibration curves of this format do not oscillate between values the way that polynomial fits may, consistent with the fundamental properties of film. Nevertheless, polynomial-fitted calibration curves are prevalent in the literature. Carrasco et al. (2013) use a third order polynomial fit:

$$D = a(netOD)^3 + b(netOD)^2 + c(netOD) + d. \tag{3.14}$$

To avoid non-physical oscillation between values, the authors use 24 points in addition to the point corresponding to the unirradiated film to establish their fitting parameters. Evgeniia et al. (2015) use an exponential form:

$$netOD = a\left(1 - e^{-bD}\right) + c\left(1 - e^{-dD}\right). \tag{3.15}$$

Finally, a variety of studies (Borca et al., 2013; Devic, 2011; Devic et al., 2004, 2009, 2012; Ferreira et al., 2009; Martišìkovà et al., 2008; McCaw, 2015; Reinhardt et al., 2012, 2015; Sorriaux et al., 2013) use response curves of the general form:

$$D = a(netOD) + b(netOD)^c, \tag{3.16}$$

and Papaconstadopoulos et al. (2014) use this same general form with the quantity, $\triangle$netOD:

$$D = a(\triangle netOD) + b(\triangle netO)^c, \tag{3.17}$$

where a and b are free parameters, and c is a problem-dependent parameter. The abundance of examples in the literature specifically for radiochromic film response, including detailed uncertainty analyses, promoted the use of this form for the current project.

3.6.2 Dose-to-water per air kerma simulations

Previous work at the UWMRRC included the design and construction of a custom thin-window water phantom for use with the orthovoltage unit (Lawless, 2016), which was used for all in-water film irradiations. Six $(1 \times 1)\,\mathrm{cm}^2$ film samples were irradiated together in air-tight, vacuum-sealed packets in a $(10 \times 10)\,\mathrm{cm}^2$ field at each calibration dose level at 5 cm depth in a 100 cm SAD irradiation geometry. Monte Carlo methods were used to determine the irradiation time for each set-up. As discussed previously, the UWADCL UW250-M beam is traceable to NIST air-kerma standards, and can be measured precisely using an A3 ionization chamber in air. Previous work at the UWMRRC related dose to the active layer of film in air to air kerma, with the film suspended in air, contained in vacuum-sealed packets (Rosen, 2015). That work was completed using Monte Carlo N-Particle Transport Code (MCNP), versions 5 and 6 (X-5 Monte Carlo Team, 2005; X-6 Monte Carlo Team, 2014), and found a conversion coefficient of 1.087 ± 0.003 dose-to-film in air per unit air kerma.

For this work, the quantity of interest was dose-to-water (in water). To determine dose-to-water per unit air kerma, similar methods were used as those described for determining dose-to-film in air per unit air kerma. MCNP6 was used for continuity with previous work. First, the UWMRRC custom orthovoltage water phantom was modeled as a $(30 \times 30 \times 30)\,\mathrm{cm}^3$ block of water in vacuum, with the front face of the phantom accommodating a thin window modeled as a polymethyl-methacrylate (PMMA) 9 cm-radius right circular cylinder, 0.146 cm thick, to match the machining specifications of the phantom (ignoring any bowing effects of the window for simplicity). A spherical tally cell of radius 0.955 cm was placed at 5 cm depth and sized to represent an A3 chamber with an inner wall diameter of 1.91 cm. A point source was defined using the measured spectrum for the UW250-M beam (Moga, 2011) as a cone projecting a spherical field of radius 5 cm at 100 cm from the source to achieve a field with an area/perimeter ratio equal to the area/perimeter ratio of the square $(10 \times 10)\,\mathrm{cm}^2$ field available with the UWMRRC orthovoltage unit (Lim, 2006). Vacuum was specified outside of the phantom because the measured spectrum was corrected to in-vacuum values.

A *F8 (energy-weighted pulse height) tally in the photon and electron modes was used to tally energy deposited in the tally cell, normalized per starting particle, to find dose to the water tally volume. For the following simulation, the tally cell material was set to air, and all other materials were specified as vacuum space. The same source specifications were used. An F6 (track length estimate of energy deposition) tally in the photon mode was used to tally energy per unit mass, normalized per starting particle, to find air kerma to the air tally volume. The number of particles run was chosen to find relative errors of less than 0.1%. The photon and electron cut-off parameters were set to 1 keV for both simulations. The conversion coefficient determined with MCNP6 was found to be 1.038 ± 0.001 dose-to-water in water per unit air kerma (with the stated uncertainty indicating the statistical uncertainty of the simulations at the $k = 1$ level).

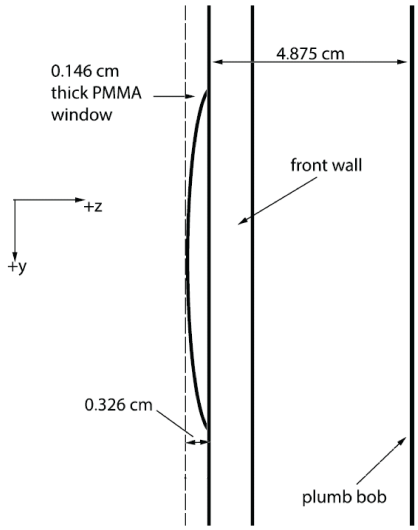

Figure 3.9: Cross-sectional diagram of the entrance side of the thin-window water phantom used in this work, including positioning plumb bob offset and window bowing. Reprinted with permission from M. J. Lawless, "Development of kilovoltage x-ray dosimetry methods and their application to cone beam computed tomography," Ph.D. thesis, University of Wisconsin, Madison. Copyright 2016, Michael J. Lawless.

In addition to the simulations completed using MCNP6, the dose-to-water in water per unit air kerma was also found using EGSnrc for consistency with the other simulations completed in this work and to avoid the approximations taken using MCNP6. For this application, the DOSRZnrc user code (Rogers et al., 2011) was used to tally air kerma in an in-air geometry and dose-to-water in water. Instead of approximating the source as a point source with energies sampled from a measured spectrum, projected to an equivalent cone, the validated EGSnrc model phase space was used as a source to take into account the actual beam dimensions, and the water phantom was modeled to include deviations from nominal dimensions based on machining tolerances and window bowing. Water pressure from the filled phantom caused the thin entrance window to bow outward, with a maximum deviation of 0.326 cm (Lawless, 2016), as illustrated in Figure 3.9. The conversion coefficient determined with EGSnrc was found to be 1.112 ± 0.003 dose-to-water in water per unit air

kerma (with the stated uncertainty included as the total uncertainty of the simulations at the $k = 1$ level, as described in the following section). This was the value used for this work.

3.6.3 Calibration of ΔnetOD to dose-to-water values

Using the Monte Carlo-defined conversion factors to relate air kerma to dose-to-water, films were irradiated to known dose-to-water values at depth, as shown in Figure 3.10 and 3.11. Calibration curves are included in Figures 3.12 and 3.13.

3.6.4 Uncertainty analysis

3.6.4.1 Dose-to-water calculation uncertainty

Uncertainty in the air-kerma measurement was acquired from the University of Wisconsin Radiation Calibration Laboratory (UWRCL) uncertainty budgets for therapy-class ionization chamber calibrations (UWRCL, 2016). Major sources of uncertainty in the dose-to-water per air-kerma factor calculated with EGSnrc include the statistical uncertainty associated with the simulations as well as the uncertainty introduced by the electron stopping powers, the photon interaction cross sections, and the photon spectra used in the original validated BEAMnrc model (Muir and Rogers, 2010; Rogers and Bielajew, 1990; Zink and Wulff, 2012).

To quantify the uncertainty introduced by uncertainty in the electron stopping powers, the mean excitation energy, I, for each material was varied. For high-Z materials, such as tungsten, the uncertainty in I may be 1–10% (ICRU Report 37, 1984; Zink and Wulff, 2012). The ESTAR program (Berger et al., 2005) was used to adjust the I value by 10% for all simulated materials, and used to generate both modified density corrections and a new PEGS file (Kawrakow et al., 2010) with adjusted collision stopping powers. Simulations were repeated with the adjusted I values, assuming a triangular distribution to estimate the uncertainty based on the electron stopping powers.

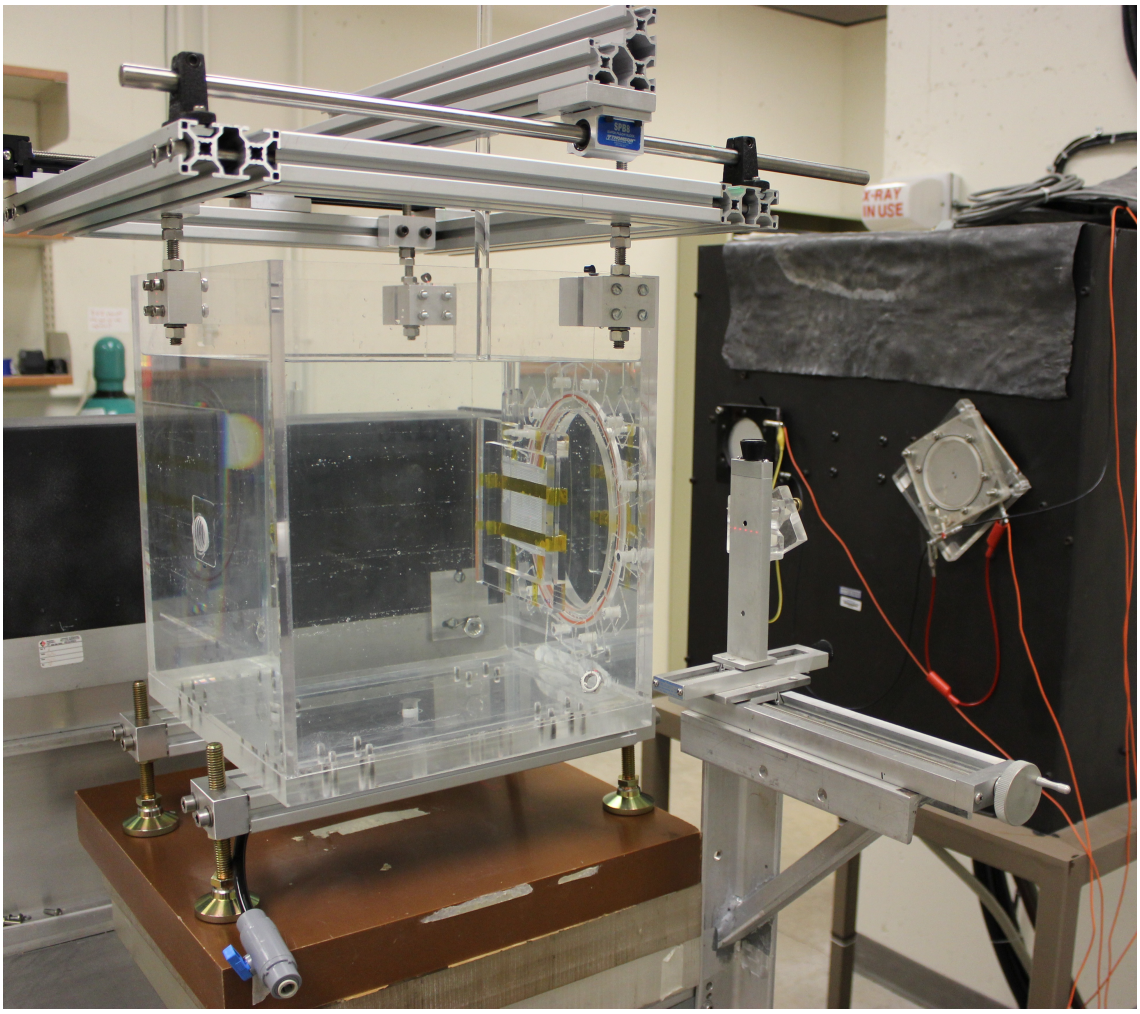

Figure 3.10: Photograph of the irradiation geometry for the calibration of EBT3 film in water with the UW250-M beam using the UWMRRC thin-window water phantom. The films were placed at 5 cm depth, 100 cm SAD, positioned using hanging plumb bobs and wall and ceiling laser alignment systems.

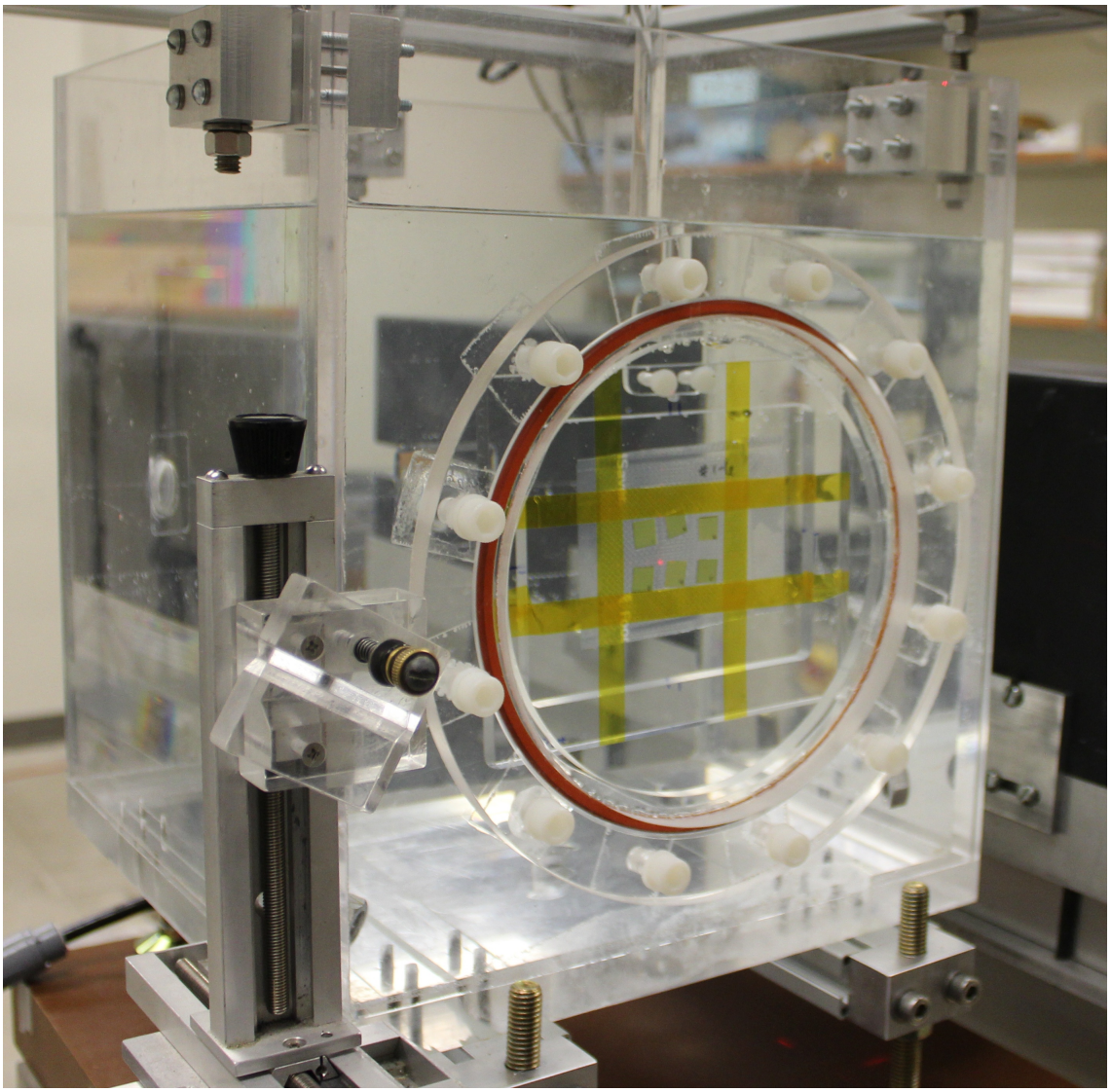

Figure 3.11: Photograph of the irradiation geometry for the calibration of EBT3 film in water with the UW250-M beam using the UWMRRC thin-window water phantom. For all calibration irradiations, six $(1 \times 1)\,\mathrm{cm}^2$ film samples were placed in air-tight, vacuum-sealed packets, suspended in the water phantom using a PMMA holder and Kapton tape.

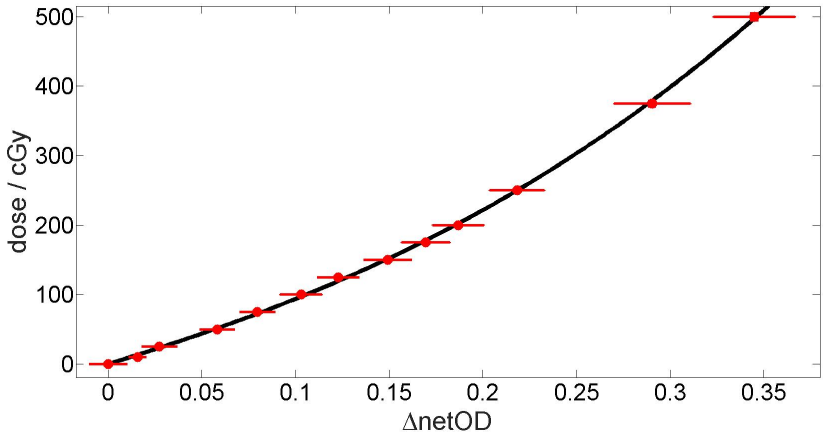

Figure 3.12: EBT3 calibration data used in this work with the EPSON scanner. Error bars represent the calculated full uncertainty at the $k = 2$ level. A curve of the form from Equation 3.17 is included.

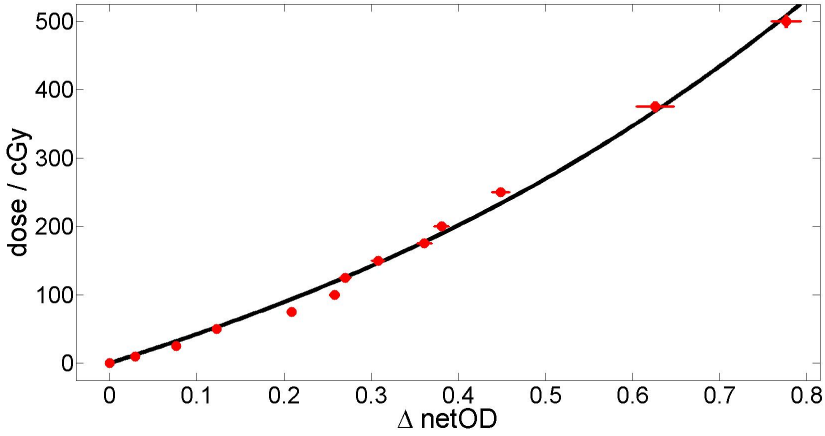

Figure 3.13: EBT3 calibration data used in this work with the LDS. Error bars represent the calculated full uncertainty at the $k = 2$ level. A curve of the form from Equation 3.17 is included.

Table 3.3: Sample uncertainty budget for the Monte Carlo-determined dose-to-water values. All values are expressed in percent.

Parameter	Type A	Type B
air-kerma measurement		0.45
statistical computational uncertainty	0.24	
electron stopping powers		0.05
photon cross sections		0.04
photon spectra		0.08
quadratic sum	0.24	0.46
A and B quadratic sum	0.52	
Total combined uncertainty	0.52% ($k = 1$)	
Expanded total uncertainty	1.04% ($k = 2$)	

Uncertainty in the photon interaction cross sections is estimated to be 1–5% in the energy range of interest (Hubbell, 1999; Muir and Rogers, 2010; Rogers and Bielajew, 1990; Storm and Israel, 1970). Photon cross sections were therefore scaled by 5% and compared to the results with the XCOM cross-section library. The deviation between the two dose-to-kerma ratios was used to estimate the uncertainty based on photon interaction cross sections, and a triangular distribution was assumed.

To examine the uncertainty introduced by the photon spectra, the spectrum of the validated full BEAMnrc model of the orthovoltage unit was tabulated using the BEAMDP (BEAM Data Processor) program (Ma and Rogers, 1995). A point source was simulated with two different spectra: first, sampled from the spectrum derived from the full BEAMnrc model, and second, sampled from the high-purity germanium spectrometer-measured spectrum discussed in Section 3.1.1. The difference between the two resulting conversion factors was used to estimate the uncertainty due to the photon spectrum, and a triangular distribution was assumed. A tabulated uncertainty budget summarizing the uncertainty involved in the dose-to-water calculation is included in Table 3.3, following the methodology described in NIST Technical Note 1297 (Taylor and Kuyatt, 1994).

Table 3.4: Sample uncertainty budget for EBT3 film and LDS scanning system read out. All values are expressed in percent.

Parameter	Type A	Type B
beam uniformity		0.10
film positioning		0.58
post-exposure development duration		0.19
scanning orientation		0.40
film and scanner uniformity	0.45	0.55
quadratic sum	0.45	0.92
A and B quadratic sum	1.02	
Total combined uncertainty	1.02% ($k = 1$)	
Expanded total uncertainty	2.05% ($k = 2$)	

3.6.4.2 EBT3 film uncertainty

In addition to the uncertainty in determining the delivered dose-to-water values, there exists uncertainty associated with the radiochromic film and scanning systems. As discussed in Section 3.3, meticulous film-handling methods were used to minimize uncertainty introduced by the film measurements. Sources of uncertainty include variation in beam flatness, film positioning, post-exposure autodevelopment duration, scanning orientation, film and scanner uniformity, and beam uniformity. The beam uniformity was acquired from the UWRCL uncertainty budget for therapy-class ionization chamber calibrations (UWRCL, 2016). To estimate repeatability of the film positioning during irradiation and precision of alignment systems, measured PDDs of the UW250-M beam were used (Lawless, 2016) with an assumed precision of ± 1 mm and a rectangular distribution. Within the dose range of interest and following seven days of autodevelopment, uncertainty due to changes in post-exposure autodevelopment duration of up to three days was estimated based on the work by Borca et al. (2013), and a rectangular distribution was assumed. Film scanning rotational dependence, inter- and intra-film uniformity, and scanner measurement uncertainty have been previously characterized by Rosen et al. (2015) and Hammer et al. (2017) for the

LDS, and by McCaw (2015) for the EPSON. A sample tabulated uncertainty budget summarizing the uncertainty involved in the EBT3/scanner system measurements is included in Table 3.4.

Chapter 4

Orthovoltage Dose Gradient Index analyses

As noted in Section 2.2, the steepness of dose gradients outside of an SRS target volume may be quantified by the Dose Gradient Index (DGI):

$$DGI = \frac{Vol_{50\%\,\mathrm{Rx}}}{Vol_{100\%\,\mathrm{Rx}}}, \tag{4.1}$$

where $Vol_{50\%\,\mathrm{Rx}}$ is the volume encompassed by the 50% prescription isodose surface, and $Vol_{100\%\,\mathrm{Rx}}$ is the volume encompassed by the 100% prescription isodose surface. Previous work by Bender (2014) has examined the trade-off between prescription isodose and DGI in a standard 6 MV linear accelerator SRS delivery. This chapter similarly examines such a trade-off in orthovoltage SRS. This chapter contains work that was originally published in Medical Physics (Fagerstrom et al., 2016) and is reproduced here with permission.

4.1 Dose-spread kernel generation

4.1.1 Point energy-deposition kernels

Monte Carlo simulations for this work were performed using EGSnrc, and energy-deposition kernels (EDKs) were generated using the EDKnrc user code. In the simulations, monoenergetic photon collisions were forced at the center of a 60.0 cm-radius sphere of water. A series of 48 cones (separated by a polar angle of 3.75°) and 24 radial shells were used to mark boundaries for 1152 voxels based on the EDKnrc user code. The shell thickness was smallest near the origin and largest at the sphere's boundary to have finest resolution near the regions of highest dose gradient. The innermost shell radial boundaries were placed at 0.002 cm, 0.01 cm, 0.05 cm, and 0.1 cm, and the outermost shell radius boundaries were placed at 20.0 cm, 30.0 cm, 40.0 cm, and 60.0 cm. Finer resolution near the point of interaction was used compared to that used in previous kernel generation studies (Alaei et al., 1999; Mackie et al., 1988; Mainegra-Hing et al., 2005) in order to avoid volume averaging effects near the point of interaction, requiring running additional particles to achieve acceptable statistics in the reduced-volume voxels.

Photon and electron kinetic energy cut-off values (PCUT and ECUT) were set to 1 keV, and PEGS4 material data files were set to include an energy range down to 1 keV, and included cross sections for Rayleigh scattering as well as density corrections and radiative stopping powers from ICRU Report 37 (1984). The XCOM library (Berger et al., 2010) was used for photon interaction cross sections. Bound Compton scattering, photoelectron angular sampling, Rayleigh scattering, atomic relaxations, and electron impact ionization were all turned on for all simulations to increase simulation accuracy. The bremsstrahlung angular sampling was set to use the entire modified Koch and Motz equation (Koch and Motz, 1959) instead of the simplified version using only the first term. All other parameters were set to default values. The total fractional energy deposition within voxel (i, j) was

defined as the following:

$$\epsilon(i,j) = \frac{E_{\text{dep}}(i,j)}{N_0 h\nu_0}, \tag{4.2}$$

where $E_{\text{dep}}(i,j)$ is the total energy deposited in voxel (i,j), and N_0 is the total number of histories run, and $h\nu_0$ is the energy of each primary photon (Mainegra-Hing et al., 2005). Considering the low energy range of interest and the size of the water phantom, a negligible fraction of the incoming beam's energy was able to escape the sphere. The denominator in Equation 4.2 approximates the total energy deposited within the sphere, and $\epsilon(i,j)$ approaches the energy fraction deposited within voxel (i,j). Using the above parameters, EDKs were generated from 10 keV to 250 keV, in 10 keV increments.

Graphical representations of kernels generated in a previous version of EGS, EGS4, have been published by Mackie et al. (1988) and Alaei et al. (1999), and these results were compared to those found in this study. Mackie and Alaei both represented their kernels in isoline format with units of cGy/photon-MeV, normalized to the energy of incident photons interacting at the origin. Because voxels had variable volumes in the study, it was desired to normalize by the voxel (i,j) volume for each value of $\epsilon(i,j)$ in Equation 4.2. The volume for each voxel was calculated analytically using a series of stacked, truncated spherical cones, according to the following:

$$\begin{aligned} \text{volume}(i,j) &= \tfrac{2}{3}\pi \left[(\cos\theta_{i-1} - \cos\theta_i) \left(r_j^3 - r_{j-1}^3 \right) \right], \\ \theta_i &= 0^\circ,\ 3.75^\circ,\ 7.5^\circ,\ 11.25^\circ,\ \ldots,\ 180^\circ, \\ r_j &= 0,\ 0.002,\ 0.01,\ 0.05,\ \ldots,\ 60.0\,\text{cm}. \end{aligned} \tag{4.3}$$

Along with values for the phantom's water density, volume(i,j) was used to calculate volume-normalized kernel values, $\kappa(i,j)$, in the desired units to compare with previously published values. The 100 keV kernel in isoline format, compared to Mackie's kernel, is included in Figure 4.1.

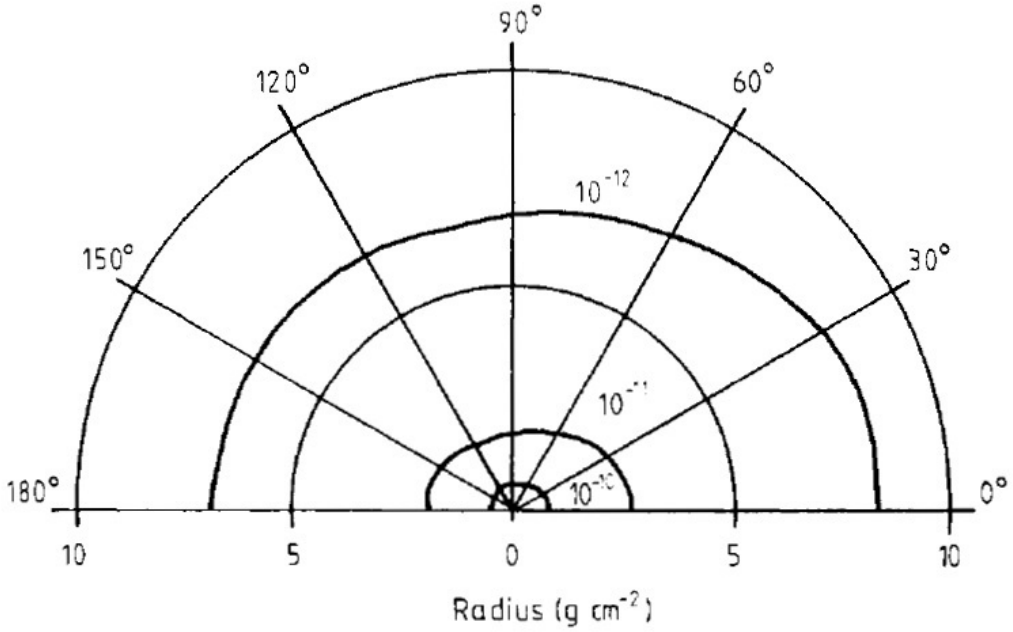

(a)

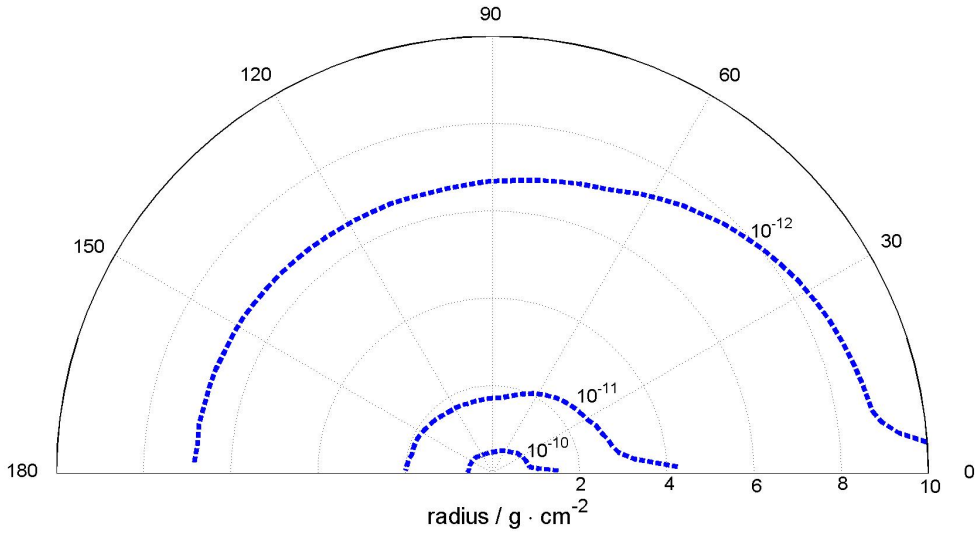

(b)

Figure 4.1: Comparison of 100 keV kernels in isoline format in units of cGy/photon-MeV, normalized to the energy of incident photon interacting at the origin calculated by (a) Mackie et al. (1988) and (b) this work. The incident beam direction is 0°. (a) Reprinted with permission from T. R. Mackie et al., "Generation of photon energy-deposition kernels using the EGS Monte Carlo code," Physics in Medicine and Biology, 33 (1), 1–20, 1988. Copyright 1988, Institute of Physics and Engineering in Medicine, IOP Publishing.

4.1.2 Rayleigh scattering

The newly calculated isolines differ from the previously published isolines with the inclusion of "tails" peaked in the forward beam direction at small angles. These tails were found for other modeled kernels within the energy range of interest. After modeling 20 keV, 100 keV, and 250 keV kernels with and without Rayleigh scattering included in the EDKnrc simulations, the tails were determined to be the result of including Rayleigh scattering in the model (see Figure 4.2). A 10 MeV kernel was also modeled for completeness, and was found to have a similar shape as Mackie's published high-energy kernels, with no tails present (Figure 4.3). Both Mackie and Alaei state that they did not include Rayleigh scattering in their kernel modeling. A study by Mainegra-Hing et al. (2005) revealed that while the inclusion of Rayleigh scattering in a low-energy kernel model does not affect the primary component of the kernel, it increases the scatter component by three to five times and therefore should be included in the kernel.

The atomic cross section for Rayleigh scattering is related to medium of interaction and incoming photon energy:

$$\frac{\sigma_{\mathrm{R}}}{\rho} \propto \frac{Z}{(h\nu)^2}. \tag{4.4}$$

Due to competing Compton and photoelectric interactions, trends based solely off of Z and $h\nu$ are not immediately obvious, though for low Z materials, Rayleigh scattering becomes more pronounced with decreasing photon energy (Attix, 1986). Rayleigh scattering is elastic, with photons interacting with a whole atom as opposed to the Thomson (elastic) limit of Compton scattering, with photons only interacting with free charged particles in the medium. In Rayleigh scattering, the incoming photon loses negligible energy and the interacting atom recoils with minimal imparted kinetic energy in order to preserve conservation of momentum, and the photon is deflected at a small angle (Kissick and Fakhraei, 2016). Fano (1953) reports that for 100 keV photons, 60–70% of Rayleigh scattering angles are less than 30° for lead ($Z = 82$), 20° for iron ($Z = 26$), and 15° for aluminum ($Z = 13$).

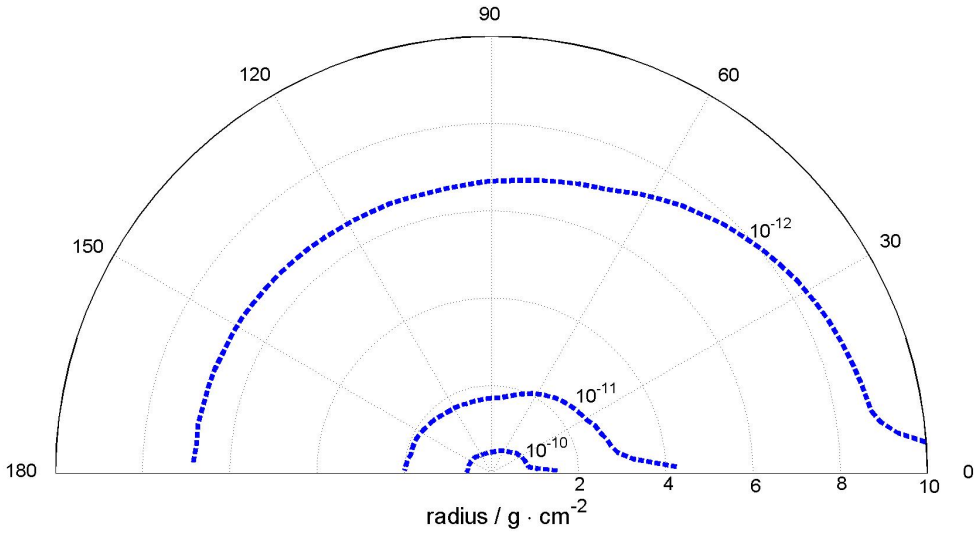

(a)

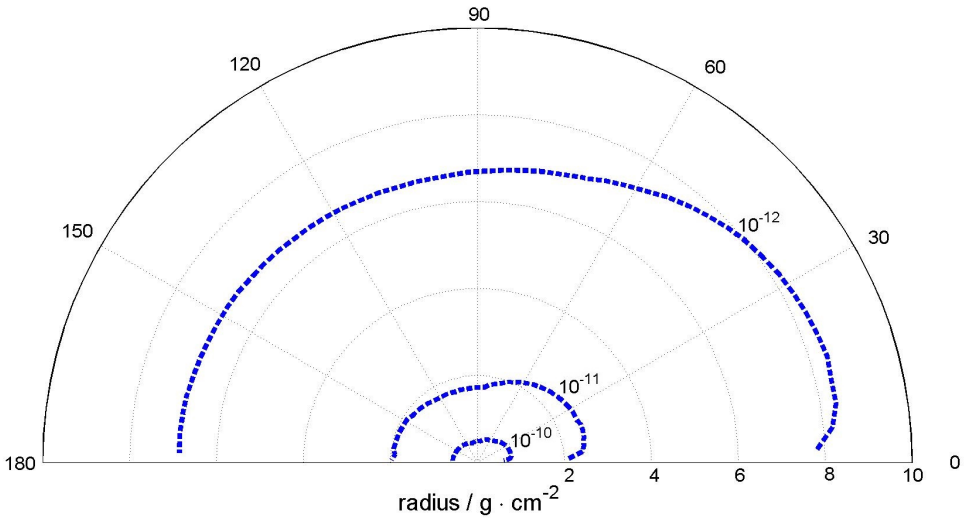

(b)

Figure 4.2: Comparison of 100 keV kernels in isoline format in units of cGy/photon-MeV, normalized to the energy of incident photon interacting at the origin modeled (a) with Rayleigh scattering and (b) without Rayleigh scattering. The incident beam direction is 0°.

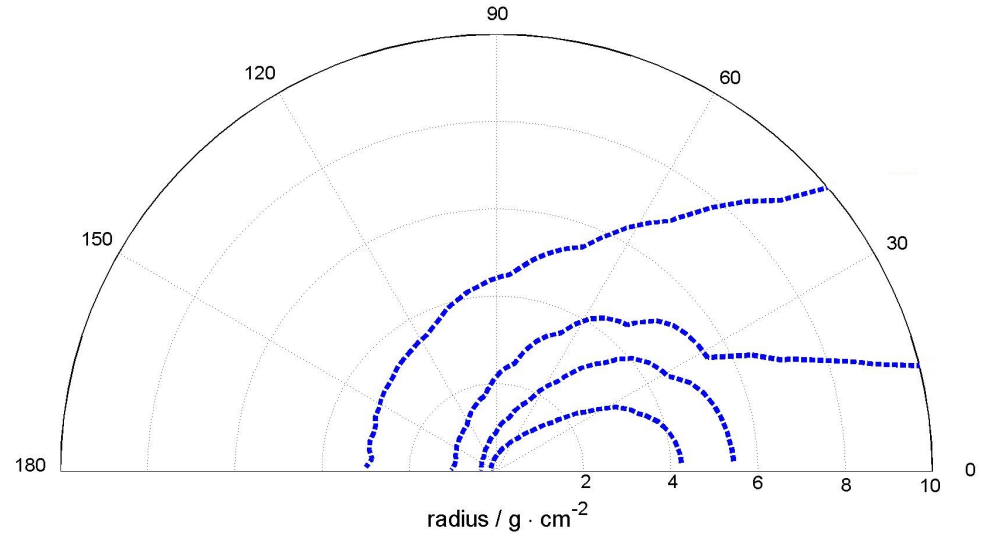

(a)

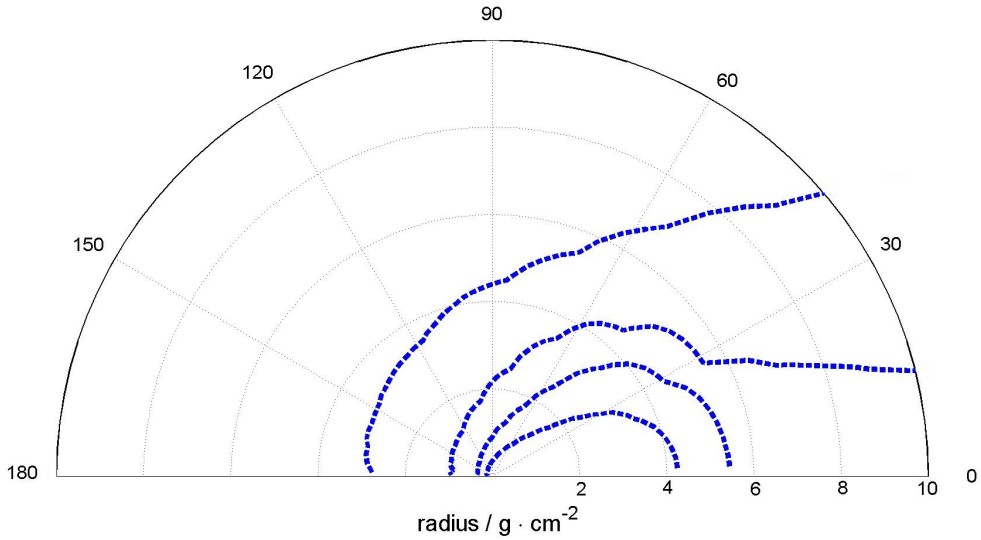

(b)

Figure 4.3: Comparison of 10 MeV kernels in isoline format in units of cGy/photon-MeV, normalized to the energy of incident photon interacting at the origin modeled (a) with Rayleigh scattering and (b) without Rayleigh scattering. The incident beam direction is 0°.

The forward-peaked nature of Rayleigh scattering explains the tails of Figures 4.1 and 4.2. Because Rayleigh is physically happening, the kernels simulated including this effect were used.

4.1.3 Pencil kernels

It was desired to convert the polar coordinates from the EDKnrc simulations into three-dimensional Cartesian coordinates for a subsequent convolution with a TERMA vector. This conversion was accomplished using a MATLAB script that defined a three-dimensional Cartesian grid with values of x, y, and z spanning from -60 cm to +60 cm and running through all points on the grid to complete a two-dimensional interpolation from kernel values based on corresponding (r, θ) values. These Cartesian three-dimensional kernels can be visualized in two dimensions in isoline format, or in three dimensions in isosurface format. Examples of representative formatted kernels are included in Figures 4.4 and 4.5.

The variation in shape of the kernels based on energy may be explained by the varying probabilities of different physical processes and kinematics based on energy (Attix, 1986). In this energy range and in water, there are competing processes of photoelectric and Compton scattering interactions. If a photoelectric event takes place, the angle of the emitted photoelectron relative to the direction of the incident photon is near 90° for low energies and becomes more forwardly directed with increasing energies. The resulting shell vacancy may result in the emission of an Auger electron or fluorescence photon emission, both of which are emitted isotropically. If a Compton scattering event takes place, the angles of the emitted photon and electron relative to the direction of the incident photon are also energy-dependent. In the low energy limit, there is Thomson scattering resulting in the electron emitted at 90° and the scattered photon at 0°. At higher energies, the fraction of the incident photon's energy given to the recoiling electron compared to that given to the scattered photon is dependent on energy. Furthermore, the differential Klein-Nishina cross section per unit angle for both the photon and electron is dependent on energy.

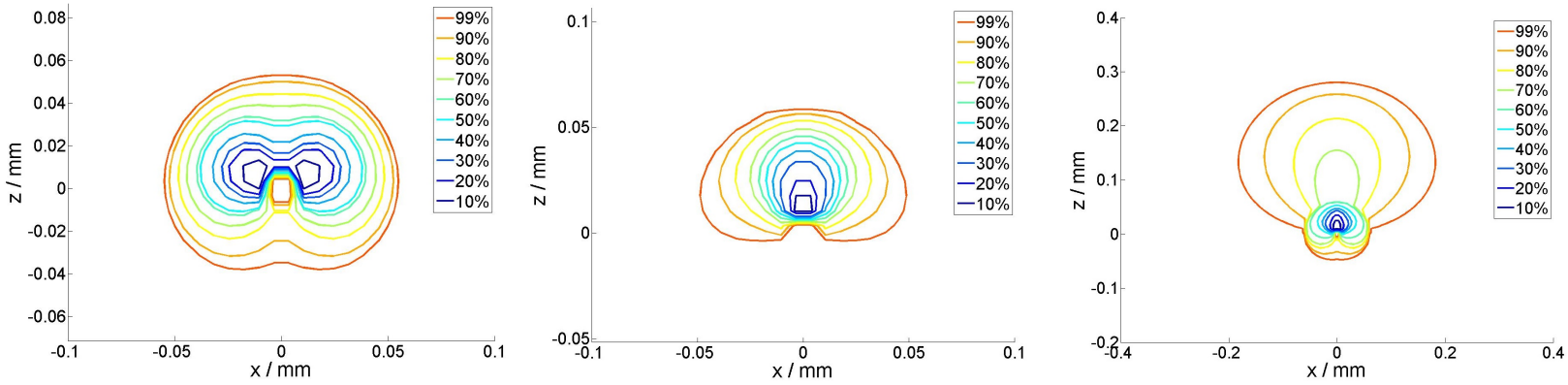

Figure 4.4: Two-dimensional isoline values of unitless kernels (κ) for (a) 20 keV incoming photons, (b) 100 keV, and (c) 250 keV. The point of interaction is at $(x, y, z) = (0, 0, 0)$ and the beam axis is along $+z$. Each isoline represents a fraction of the total dose encompassed (for example, the 20% line encompasses the region in which 20% of the total dose is deposited for that kernel). Note the change in scale between figures.

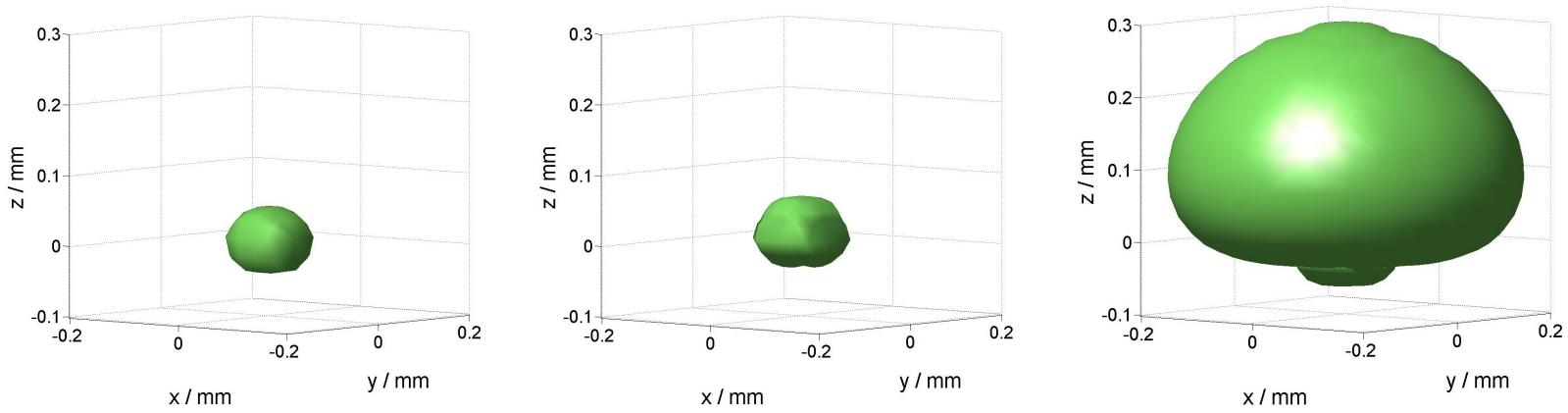

Figure 4.5: Three-dimensional isosurface representation of unitless kernels (κ) for (a) 20 keV incoming photons, (b) 100 keV, and (c) 250 keV. The point of interaction is at (x, y, z) = (0, 0, 0) and the beam axis is along $+z$. The same isosurface value (encompassing 75% of the total dose deposited for each kernel) was used to generate the contours for each plot.

For the pencil-beam calculations, pencil kernels were used instead of the previously described point kernels. Pencil kernels describe energy deposition in a semi-infinite medium from a point monodirectional beam (Ahnesjö and Aspradakis, 1999). Pencil kernels were generated from the EDKnrc simulation results by convolving the point kernels with TERMA vectors using a built-in MATLAB function *convn* to generate pencil-beam kernels in a $(120 \times 120 \times 120)\,\mathrm{cm}^3$ cube of water. Values for TERMA were found by multiplying the primary energy fluence by the mass attenuation coefficient: $\Psi\,(\mu/\rho)$, using NIST values for mass attenuation coefficients in water (Hubbell and Seltzer, 2004). Examples of pencil-beam kernels at a depth of $z = 5\,\mathrm{cm}$, visualized at $y = 0\,\mathrm{cm}$, are included in Figure 4.6.

4.2 Dose Gradient Index calculations

For simplicity, this work concentrates on a true 4π, isotropic dose delivery from all angles of a beam incident on spheres of water (with radii of 5.0, 7.5, and 10 cm), resulting in spherical dose distributions. For such a distribution, DGI, as defined in Equation 4.1, may then be written,

$$DGI = \left(\frac{R_{50\%\,\mathrm{Rx}}}{R_{100\%\,\mathrm{Rx}}} \right)^3, \tag{4.5}$$

where $R_{50\%\,\mathrm{Rx}}$ is the distance between the isocenter and the surface at which dose falls to 50% of the prescription dose and $R_{100\%\,\mathrm{Rx}}$ is the distance between the isocenter and the prescription isodose surface.

The isotropic dose distribution was approximated by calculating a distribution from a single beam, rotating the distribution, and summing for a cumulative distribution. The dose distribution from a single beam was calculated using a pencil kernel convolved with fluence from an open SRS cone collimator (assuming a point source) in a sphere of water. The distribution was rotated using a three-dimensional affine rotational transformation,

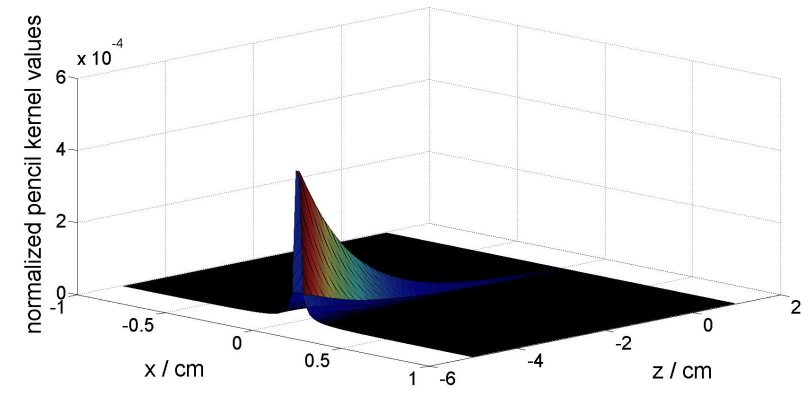

(a)

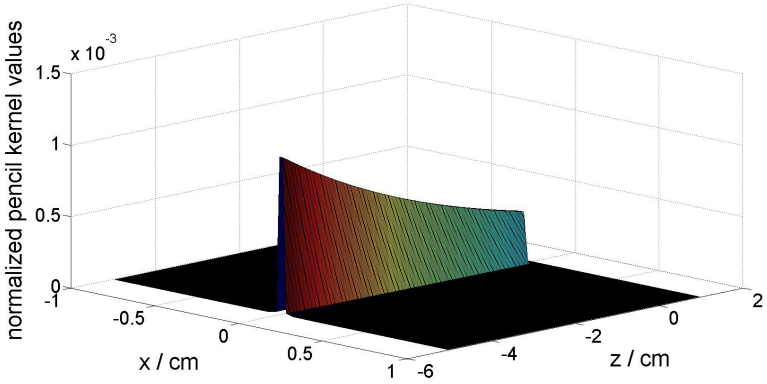

(b)

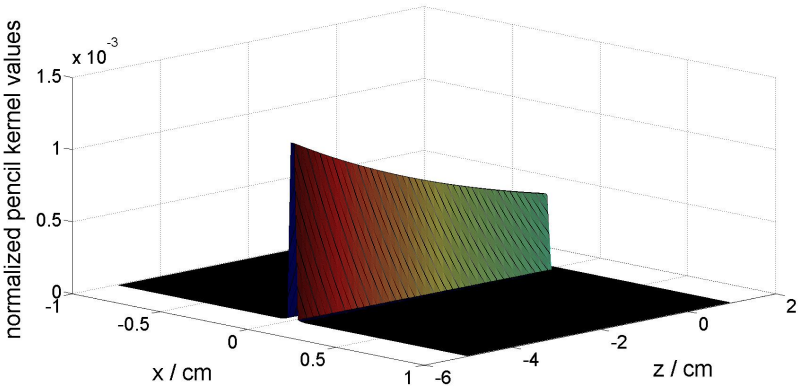

(c)

Figure 4.6: Pencil-beam kernels at 5 cm depth along the central axis $y = 0$, normalized to total J/kg with the beam axis along $+z$, isocenter at $(x, y, z) = (0, 0, 0)$ and the surface located at $z = -5$. Examples are shown for (a) 20 keV, (b) 100 keV, and (c) 250 keV incoming photons.

described by the transformation matrices:

$$T_\phi = \begin{bmatrix} 1 & 0 & 0 \\ 0 & \cos\phi & -\sin\phi \\ 0 & \sin\phi & \cos\phi \end{bmatrix}, \quad T_\theta = \begin{bmatrix} \cos\theta & -\sin\theta & 0 \\ \sin\theta & \cos\theta & 0 \\ 0 & 0 & 1 \end{bmatrix} \tag{4.6}$$

where T_θ and T_ϕ represent rotations in θ about the z axis and rotations in ϕ about the x axis, respectively (Arfken, 1970; Goldstein, 1980). Combining these two transformations into a single step, the transformation matrix may be written as follows:

$$T_{\text{rot}} = T_\phi T_\theta = \begin{bmatrix} \cos\theta & -\sin\theta & 0 \\ \cos\phi\sin\theta & \cos\phi\cos\theta & -\sin\phi \\ \sin\phi\sin\theta & \sin\phi\cos\theta & \cos\phi \end{bmatrix}, \tag{4.7}$$

which can be used to transform a position vector such that

$$T_{\text{rot}} \begin{bmatrix} x \\ y \\ z \end{bmatrix} = \begin{bmatrix} x' \\ y' \\ z' \end{bmatrix}. \tag{4.8}$$

The system of equations may be written as follows:

$$\begin{aligned} x' &= x\cos\theta - y\sin\theta \\ y' &= x\cos\phi\sin\theta + y\cos\phi\cos\theta - z\sin\phi \\ z' &= x\sin\phi\sin\theta + y\sin\phi\cos\theta + z\cos\phi. \end{aligned} \tag{4.9}$$

Uniformly spaced values for ϕ and θ cannot be generated for use with Equation 4.9 to create a uniform 4π distribution (uniformly spaced ϕ and θ would overcount the angles near the poles of the axes of rotation). One way to approximate a uniform distribution of points on a sphere is to borrow methods from Monte Carlo sampling. A cumulative distribution

function (CDF), F of the random variable X, can be defined for any real number x as the probability X is less than or equal to x:

$$F(x) = P\{X \leq x\}. \tag{4.10}$$

If X is a continuous random variable, the CDF can be expressed as the integral of the probability density function (PDF) f:

$$F(a) = P\{X \in (-\infty, a]\} = \int_{-\infty}^{a} f(x)dx. \tag{4.11}$$

If the CDF is invertible, then a random variable X can be generated from the CDF F by generating a uniform $[0, 1)$ random variable U, setting $X = F^{-1}(U)$ and solving (Lemieux, 1972; Ross, 2002). Solving for ϕ and θ in this application is an invertible problem. Here, the probability that a point on a unit sphere lies on a given cone defined by the solid angle Ω is $P(\Omega)d\Omega$, which may be normalized over the entire sphere (with surface area 4π):

$$\begin{gathered} d\Omega = \sin\phi d\phi d\theta \\ \int_\phi \int_\theta P(\Omega)d\Omega = 1 \\ P(\Omega) = \tfrac{1}{4\pi} \\ P(\Omega)d\Omega = \tfrac{1}{4\pi}\sin\phi d\phi d\theta \\ P(\phi,\theta)d\phi d\theta = \tfrac{1}{4\pi}\sin\phi d\phi d\theta, \end{gathered} \tag{4.12}$$

which may be rewritten:

$$\begin{gathered} P(\phi) = \int_0^{2\pi} P(\phi,\theta)d\theta = \tfrac{\sin\phi}{2} \\ P(\theta) = \int_0^{\pi} P(\phi,\theta)d\phi = \tfrac{1}{2\pi}. \end{gathered} \tag{4.13}$$

The CDFs of these functions may be written

$$\begin{gathered} F(\phi) = \int_0^{\phi} P(\phi)d\phi = \int_0^{\phi} \left(\tfrac{\sin\phi}{2}\right) d\phi = \tfrac{1-\cos\phi}{2}, \\ F(\theta) = \int_0^{\theta} P(\theta)d\theta = \int_0^{\theta} \left(\tfrac{1}{2\pi}\right) d\theta = \tfrac{\theta}{2\pi}. \end{gathered} \tag{4.14}$$

Now instead of a single random variable U, two random variables $U \in [0,1)$ and $V \in [0,1)$ may be generated such that $U = F(\phi)$ and $V = F(\theta)$. Inverting the CDFs, the following expressions for ϕ and θ are derived as follows:

$$\begin{aligned} F^{-1}(U) = \phi = \cos^{-1}(1-2U), \\ F^{-1}(V) = \theta = 2\pi V. \end{aligned} \tag{4.15}$$

Values for ϕ and θ were generated using Equation 4.15, then used with Equation 4.9 to rotate the dose distribution from a single beam around the sphere. Examples of composite dose distributions created through this method are shown in Figure 4.7. Profiles were taken through these calculated dose distributions to find values for $R_{50\%\,\mathrm{Rx}}$ and $R_{100\%\,\mathrm{Rx}}$ in Equation 4.5 and to calculate DGI for a range of prescription isodose choices. Finally, this entire process was adjusted slightly to increase calculation efficiency. Instead of taking stationary profiles throughout a cumulative dose distribution created by rotating and summing dose from a single beam, the dose from a single beam was held stationary and profiles through isocenter were rotated and summed using the same distribution of values for ϕ and θ.

A range of calculation grid resolutions was examined between 1 and 0.08 mm. No change in results was found for resolutions $\leq$0.2 mm, so all reported results were calculated with a grid resolution of 0.2 mm. Similarly, a range of number of profile projections was examined between 1,000 and 250,000. No change in results for calculated DGI analysis was found for $\geq$100,000 projections, so this was the value used.

4.2.1 SpekCalc 250 kVp spectrum calculation

To include a scenario other than dose distributions resulting from purely monoenergetic beams, it was desired to complete the same analysis using a moderately filtered 250 kVp beam. The open-source program SpekCalc (Poludniowski, 2007; Poludniowski and Evans, 2007; Poludniowski et al., 2009) v.1.1 was used for the theoretical calculation of a photon spectrum based on user-defined x-ray unit parameters and added filtration. The program

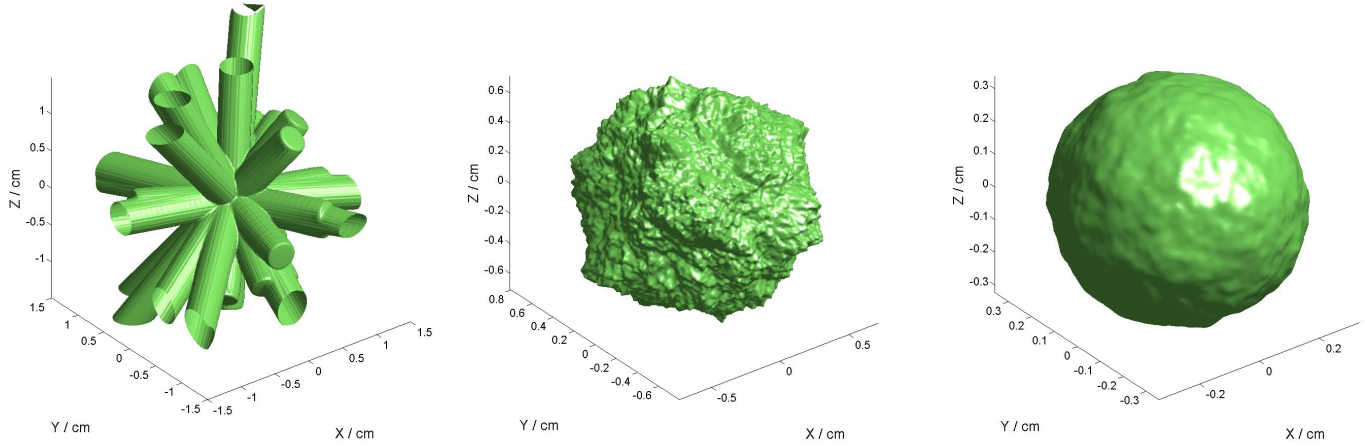

(a) (b) (c)

Figure 4.7: Simple approximation of 4π, isotropic delivery geometry from a 100 keV beam collimated by a 4 mm cone and rotated around a 5 cm-radius sphere of water. The initial pencil-kernel calculation was completed assuming point sources with a Cartesian spacing of 0.08 mm. A simplistic test case of only sixteen beams is pictured for visualization (a) and a more accurate case of 1,000 beams is compared (b). For both figures, the same isosurface value (5% maximum dose) is plotted. Finally, the central figure is replotted at 20% maximum dose (c), the lowest isosurface to be analyzed in this work.

uses deterministic equations to model bremsstrahlung productions combined with numerically precalculated electron distributions, to generate spectra for tungsten anode x-ray tubes with potentials 40–300 kVp and anode angles 6°–30°. User-defined parameters include peak energy, minimum energy, energy bin size, anode angle, and filtration thickness, with ten different materials available for filtration (air, beryllium, aluminum, copper, tin, tungsten, tantalum, water, titanium, and graphite). Using parameters based on the UWMRRC's orthovoltage unit, a photon spectrum emitted from the unit was tabulated to use as a realistic example of an orthovoltage bremsstrahlung photon spectrum. This generated spectrum had an effective energy of 142 kVp and a half-value layer of 18.2 mm aluminum. A total pencil kernel was generated by weighting the contribution from each of the monoenergetic 10–250 keV kernels based on their fractional intensity within the spectrum.

4.3 DGI analysis

Dose distributions were obtained by convolving fluence through circular cones with the generated orthovoltage pencil-beam kernels to calculate dose from a single beam in a spherical water phantom, as described previously. Composite dose distributions and composite dose distribution profiles approximating 4π isotropic delivery geometry were determined using three-dimensional affine rotational transformations. These composite dose distributions can be generated based on cone aperture size, beam energy, and radius of spherical phantom (for which the isocenter was placed at the center). The trade-off between the DGI (Equation 4.1) and prescription isodose was examined for cones ranging between 4 mm to 18 mm in diameter for monoenergetic 4π delivery, for orthovoltage energies ranging from 20 keV to 250 keV, at phantom radii of 5.0, 7.5, and 10 cm. Profiles with the polyenergetic 250 kVp spectrum as well as the monoenergetic 1 MeV beams at the same depths were also calculated to compare the monoenergetic orthovoltage delivery geometries to a realistic orthovoltage spectrum and to a megavoltage configuration. Some examples of kilovoltage configurations are included in Figure 4.8, configurations with the 1 MeV case are included in Figure 4.9,

Table 4.1: Summary of optimized DGI results including the hypothetical lower limit DGI for the specified prescription value.

Energy (keV)	Cone size (mm)	Rx resulting minimum DGI (%)	DGI for hypothetical distribution at specific Rx	Minimum DGI
20	4	64.8	1.90	4.27
20	10	74.1	1.98	4.06
20	16	80.1	2.19	4.29
120	4	64.8	1.89	1.99
120	10	87.1	1.73	1.93
120	16	89.9	1.74	1.93
220	4	62.5	1.89	1.89
220	10	88.0	1.73	1.75
220	16	93.6	1.72	1.73

and configurations with the 250 kVp case are included in Figure 4.10. For each beam energy and cone size, there is a value for prescription isodose resulting in a minimum DGI value. For the kilovoltage configurations included in Figure 4.8, the minimum DGI for 20 keV occurred with the 10 mm cone (DGI = 4.06), the minimum DGI for 120 keV occurred with the 10 mm cone (DGI = 1.93), and the minimum DGI for 120 keV occurred with the 16 mm cone (DGI= 1.73). For the 1 MeV configurations in Figure 4.9, the minimum DGI occurred with the 16 mm cone (DGI = 1.85) and for the 250 kVp configurations in Figure 4.10, the minimum DGI occurred with the 16 mm cone (DGI = 1.74). A summary of the monoenergetic orthovoltage results is included in Table 4.1.

The trade-off between DGI and prescription isodose in orthovoltage energies was found to be dependent on both field size and energy. Values for DGI were calculated for all energy, cone size, and phantom size configurations; however, it is noted that for low-energy beams treating deep-seated targets, maximum doses are achieved closer to the surface than at the isocenter in 4π isocentric delivery. For example, the 20 keV treatments of the 10 cm-radius sphere results in an isodose near the sphere periphery that is approximately 3.3 times the intensity of the dose at isocenter. This configuration is clearly not practical nor applicable

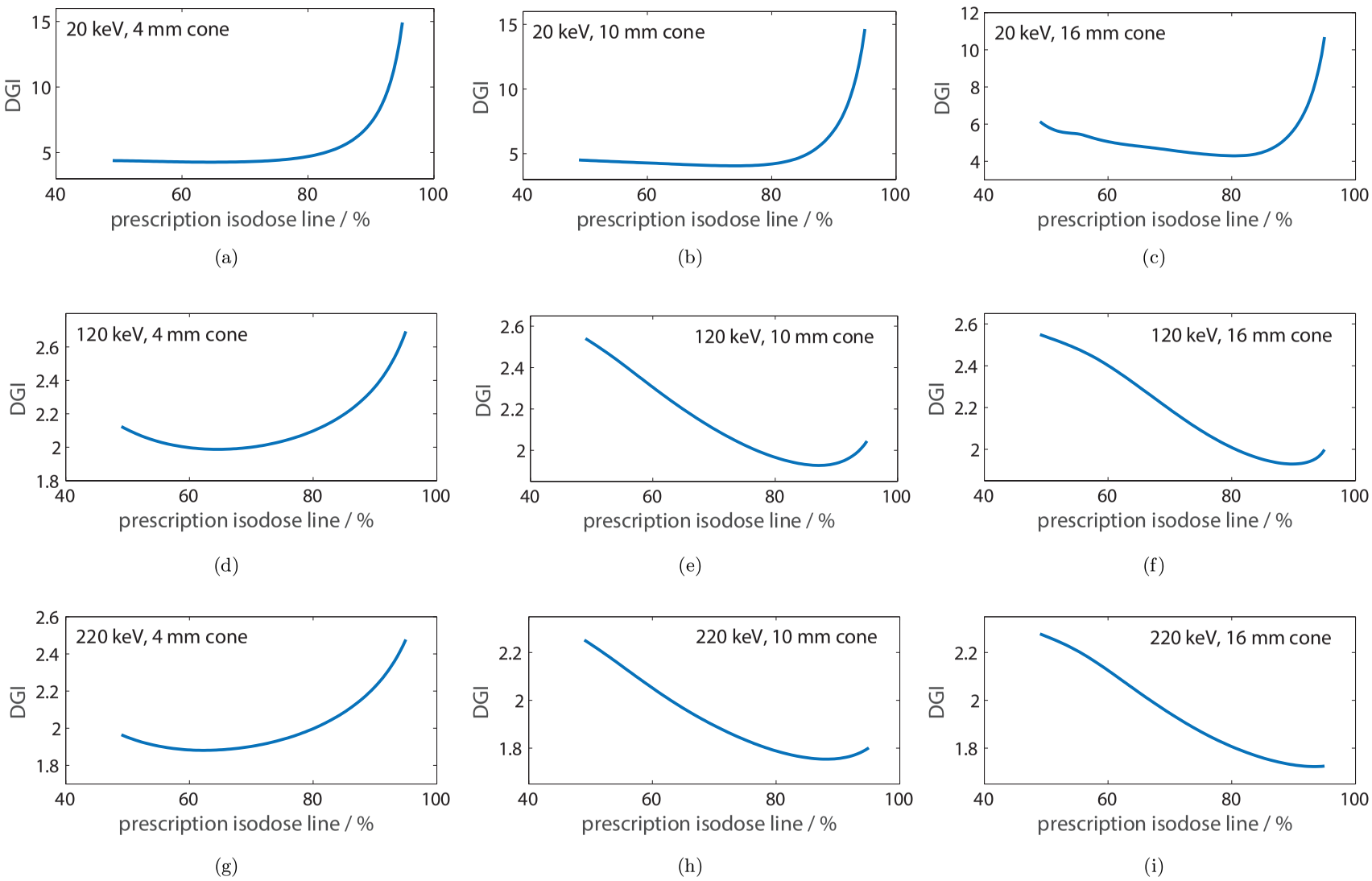

Figure 4.8: Trade-off between DGI and prescription isodose for 20 keV [top row: (a)–(c)], 120 keV [center row: (d)–(f)], and 220 keV [bottom row: (g)–(i)] monoenergetic beams collimated by a 4 mm cone [left column: (a), (d), (g)], 10 mm cone [center column: (b), (e), (h)], and 16 mm cone [right column: (c), (f), (i)], for 4π isotropic delivery about a 7.5 cm-radius sphere of water. Results were the same for the 5 cm- and 10 cm-radius spheres of water when analyzing the central isocentric volumes.

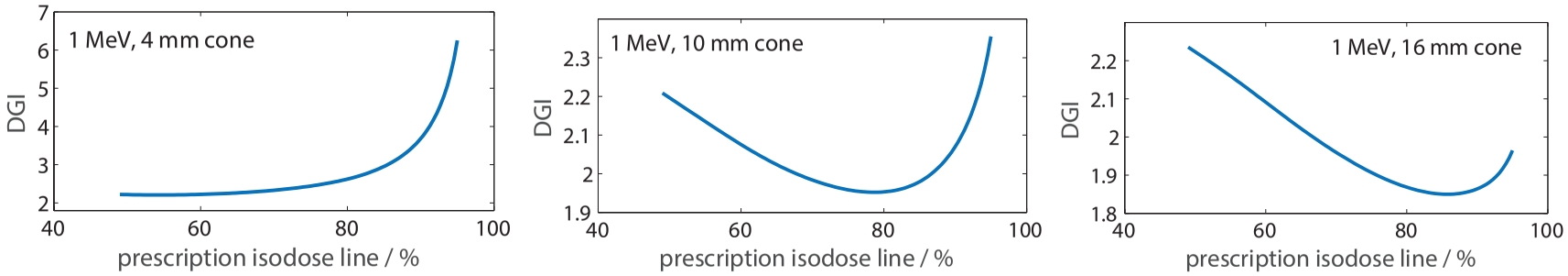

(a) (b) (c)

Figure 4.9: Trade-off between DGI and prescription isodose for 1 MeV monoenergetic beams collimated by a (a) 4 mm cone, (b) 10 mm cone, and (c) 16 mm cone, for 4π isotropic delivery about a 7.5 cm-radius sphere of water. Results were the same for the 5 cm- and 10 cm-radius spheres of water when analyzing the central isocentric volumes.

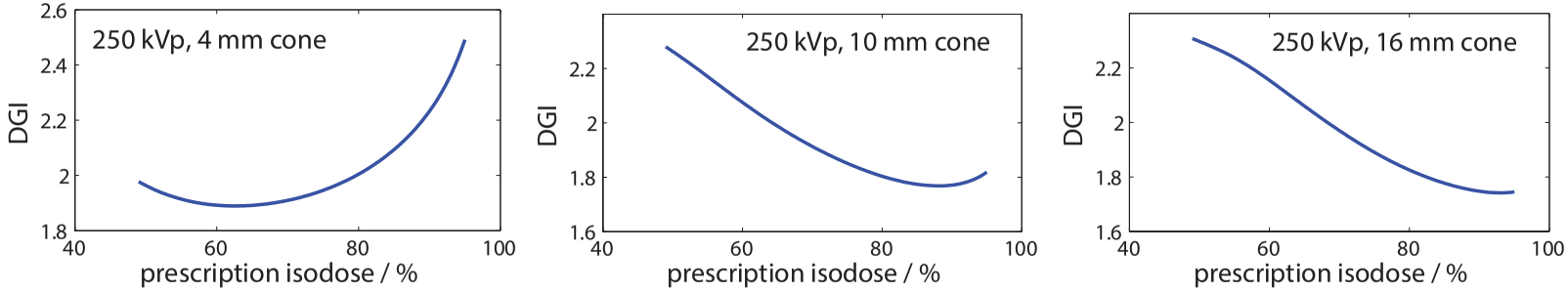

(a) (b) (c)

Figure 4.10: Trade-off between DGI and prescription isodose for polyenergetic 250 kVp beams collimated by a 4 mm cone (a), 10 mm cone (b), and 16 mm cone (c), for 4π isotropic delivery about a 7.5 cm-radius sphere of water. Results were the same for the 5 cm- and 10 cm-radius spheres of water when analyzing the central isocentric volumes.

for SRS treatment delivery in terms of hot spots and integral dose necessitated by the target coverage goals. Impracticable configurations are easily flagged using the described computational framework. Low energies with relatively high depths were studied in order to examine the extremes of the system. When ignoring peripheral dose and analyzing only the central isocentric volume, no difference in the relationship between DGI and prescription isodose was detected at different phantom sizes (and therefore different depths).

4.4 Evaluation of DGI study

For all configurations examined, there existed a prescription isodose at which the first derivative of the DGI function was zero and at which the second derivative was positive, indicating that a local minimum existed. This result indicates that for orthovoltage isocentric treatments, there exists an optimal value for prescription isodose choice in terms of dose gradients. This optimal value is dependent on both the energy and collimation configuration, regardless of the size of the spherical water phantom in which the dose was delivered. Considering the desire for these sharp gradients (Section 2.2), future orthovoltage SRS systems should be designed keeping in mind that dose gradients can be maximized based on basic parameters as described by this computational framework.

4.4.1 Idealized hypothetical collimator-beam combination

It is possible to calculate an idealized dose distribution from a hypothetical collimator-radiation beam combination that produces a perfect rectangular function dose distribution at isocenter, representing an absolute physical lower limit. This calculation accounts for attenuation of the beam through the spherical medium as well as the 4π treatment delivery geometry using the same mathematical formalism described earlier. This theoretical system was used to analyze the calculated DGI results of the more realistic, physical system.

The hypothetical collimator/radiation beam combinations that produce perfect rectangular function dose distributions at isocenter represent the absolute physical lower limits of

the system. Approximating a 4π geometry using 250,000 beam projections, the DGI values for these hypothetical treatment geometries were calculated for a range of prescription values. For every prescription value resulting in a minimum DGI value, the DGI for the hypothetical lower limit distribution was calculated for the same prescription value, and these results are included in Table 4.1 for comparison.

4.4.2 Comparison with Leksell Gamma Knife

For perspective, one may examine published results for the Leksell Gamma Knife (Elekta AB, Stockholm, Sweden). Multiple Gamma Knife models are in use today: U, B, C, 4C, and Perfexion®. These units use approximately 200 ^{60}Co sources, collimated to form circular beams with diameters of 4, 8, 14, 16, or 18 mm, depending on the model (Flickinger and Niranjan, 2015). A number of planning studies have been completed using the Gamma Knife treatment planning software package, Leksell GammaPlan (LGP), examining, among other parameters, DGI. For example, studies using Perfexion (with varied LGP versions) planned for treatment sites including vestibular schwannomas (Lindquist and Paddick, 2007; Yomo et al., 2010), meningiomas (Kaul et al., 2015; Lindquist and Paddick, 2007), skull-base tumors (Nakazawa et al., 2014), benign lesions (Bhatnagar et al., 2009), metastases (Bhatnagar et al., 2009; Kayalilar et al., 2013), and epilepsy (Hwang and Ma, 2011). These studies used between five and 40 patients, and reported DGI values ranging from 2.47 to 3.45.

In the work originally proposing the definition of DGI (Paddick and Lippitz, 2006), the authors examined 58 consecutive treatment plans (LGP v.5.32) for Gamma Knife B/C patients at a single institution over a one-year period. They found a mean DGI of 2.83, with a range of 2.4 to 3.3. They also examined 50 arbitrarily selected patients treated for vestibular schwannoma and calculated the optimal prescription isodoses to minimize DGI. They found DGI values of 2.63, 2.60, 2.37, and 2.34 for collimator sizes of 4, 8, 14, and 18 mm, respectively. Finally, a comprehensive study of 200 patient plans generated by a

single planner was conducted to examine differences in plans using different Gamma Knife models and LGP versions (Paddick, 2013). The lowest DGI values were found for plans generated with the institution's most recent versions of software and hardware (LGP v.10.1 and Perfexion), with a mean DGI value of 2.72.

4.4.3 Other SRS gradient metrics

It is noted that DGI is not the only index to quantify SRS dose fall-off. As examples, Meeks et al. (1998) described a decision tree used for SRS treatment planning, examining, among other metrics, the distance between the prescription isodose surface to half of the prescription isodose surface (e.g., the distance between the 95% isodose surface and the 47.5% isodose surface). Hong et al. (2011) examined SRS patient plans treated using high resolution mMLCs. The study created a set of retrospective treatment plans generated by increasing beam margins about the PTV in 0.5 mm increments. One of the metrics studied by Hong et al. was similar to the metric described by Meeks et al.: the difference in distance between the equivalent sphere radius of 50% of prescription dose-covered volumes and prescription dose-covered volumes.

4.4.4 Expansion on previous work

To date, there is a single published study (Bender, 2014) examining the trade-off between DGI and prescription isodose in SRS, which showed that the relationship between DGI and prescription isodose is dependent on field size in the megavoltage energy range. That work was completed using a 6 MV standard cone-based linear accelerator calculation with data fit to an analytical approximation. The increased interest in SRS delivered using orthovoltage energies (Keller et al., 2007, 2009; O'Malley et al., 2006) motivated the examination of this relationship in the orthovoltage range. This work expanded on previously published methods by using Monte Carlo methods to derive pencil kernels, and then using these updated kernels to examine a range of beam energies in the orthovoltage range. For every

combination of beam energy, collimation, and spherical phantom size, there existed a local minimum value of DGI as a function of prescription isodose choice when examining the central treatment volume at the sphere isocenter. Examining the trade-off between DGI and prescription isodose choice may be useful for designing future SRS systems in the orthovoltage energy range. This work has described the computational and mathematical processes resulting in a system on which SRS gradients may be optimized. In the following chapter, a prototype system is designed and characterized, and then the resulting system is analyzed for dose gradients using the described methodology.

Chapter 5

System design with optimization and Monte Carlo methods

This chapter describes the design of collimator and filter assemblies for use with an orthovoltage SRS system. A pencil-beam model, similar to the one described in Equation 2.2 in Section 2.4.1, was used to calculate dose distributions using the UW250-M beam. Kernels for the model were generated using Monte Carlo methods. A Genetic Algorithm search heuristic was used to optimize the spatial distribution of added tungsten filtration to approach rectangular function dose distributions at depth. Optimizations were performed for depths of 2.5, 5.0, and 7.5 cm, with cone sizes of 5, 6, 8, and 10 mm. In addition to the single-beam profiles, 4π spherical isocentric irradiation geometries were modeled to assess dose at 0.07 mm depth for the low energy beams in order to examine a surrogate quantity for skin dose. Based on the results of the optimization, circularly symmetric tungsten filters were designed to modulate the orthovoltage beam across the apertures of SRS cone collimators. For each depth and cone size combination examined, the beam flatness along with the 80–20% and 90–10% penumbrae were calculated for both standard, open cone-collimated beams as well as for the optimized, filtered beams. For all configurations tested, the modulated beams were able to achieve improved penumbra widths and flatness statis-

tics at depth. The dose at 0.07 mm depth in the 4π isocentric irradiation geometries was higher for the modulated beams compared to unmodulated beams; however, the modulated dose at 0.07 mm depth remained $\leq 0.025\%$ of the central, maximum dose. Finally, the 4π distributions were used to complete a DGI analysis, similar to the one described in Chapter 4.

5.1 Revised pencil-beam formalism

As discussed in Section 2.4.1, previous work by Bender (2014) with SRS fluence modulation indicated the possibility of optimizing 6 MV linear accelerator photon fluence for SRS dose distributions approaching rectangular functions. Dose profiles in the plane perpendicular to the beam axis were calculated using pencil- and source-kernel terms without including leakage through the collimator. Distributions were calculated for both modulated and open cones, as shown in Figure 5.1. Photon fluence was removed based on spatial position using concentric hypodermic tubing of varying lengths and diameters inserted into linear accelerator SRS cones. The resulting dose distributions were modulated to approach rectangular function dose distributions. The modulated cones showed an increase in profile uniformity within the irradiated volume, as well as a steeper dose gradient, determined by the length of the 80–20% penumbra. The pencil beam model used in this previous work (Equation 2.2) relied on the approximation that the photon fluence at any given spatial position incident on a modulated cone either traversed the cone aperture without interacting, or was absorbed in the cone or modulating material completely. To include scatter effects introduced by a filter, the current work modified the pencil beam formalism as follows:

$$\begin{aligned} K_t^{\text{total}}(x,y,z) &= \int_{-\infty}^{\infty}\int_{-\infty}^{\infty} K^{\text{source}}(x',y',z) \times K_t^{\text{beamlet}}(x-x',y-y',z)dx'dy', \\ D(x,y,z) &= \sum_{t=t_{\min}}^{t_{\max}} \int_{-\infty}^{\infty}\int_{-\infty}^{\infty} F_t(x',y',z) \times K_t^{\text{total}}(x-x',y-y',z)dx'dy', \end{aligned} \tag{5.1}$$

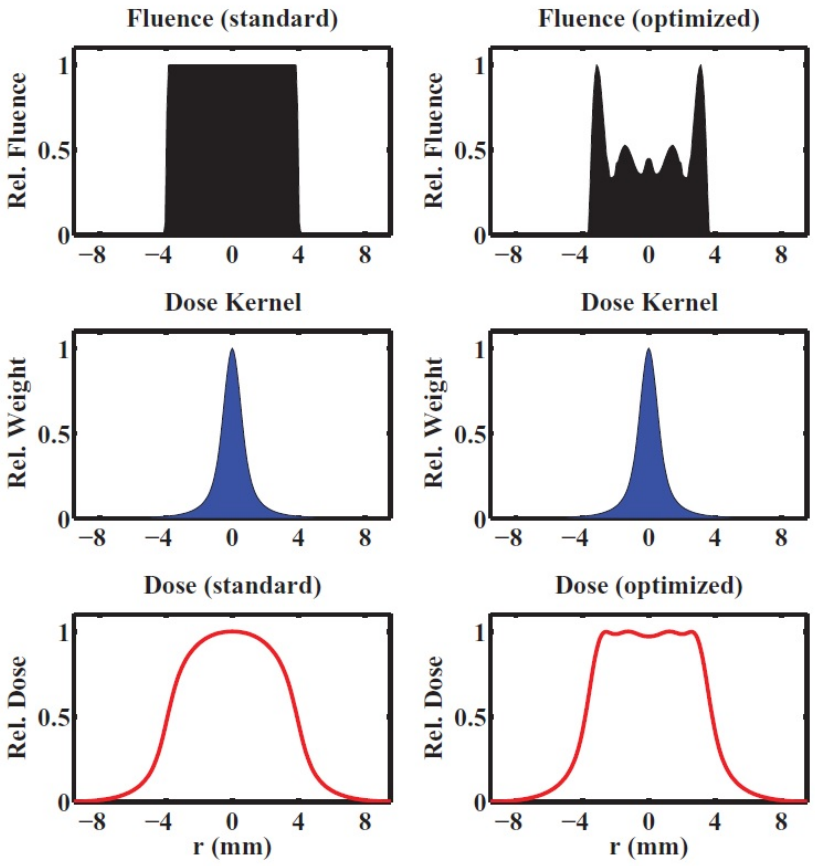

Figure 5.1: Example of a 6 MV, 8 mm cone calculation from previous work. The left column shows the initial open cone fluence, the calculated combined source and pencil kernel term at depth, and the resulting dose distribution. The right column shows the analogous fluence, kernel, and dose distribution for a modulated (fluence-optimized) cone. Reprinted with permission from E. T. Bender, "Increasing dose gradient and uniformity in small fields using modulation: Theory and prototypes for cone-based stereotactic radiosurgery," Medical Physics, 41, 051706, 2014. Copyright 2014, American Association of Physicists in Medicine.

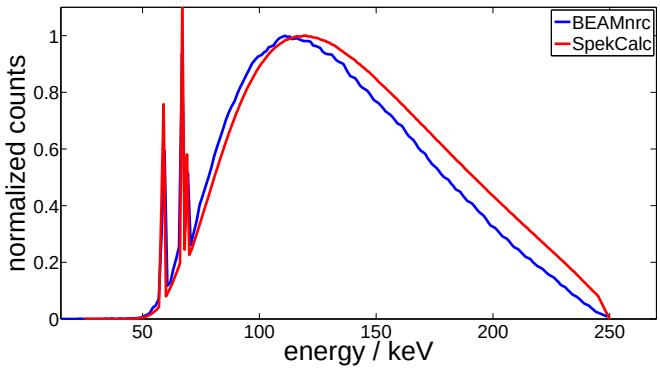

Figure 5.2: Photon spectra of the UW250-M beam simulated with the validated EGSnrc model in BEAMnrc (blue) and approximated using the SpekCalc program (red) at the plane immediately downstream of the filter pack.

where t is an index indicating the thickness of attenuating material at a given position, K_t^{total} is the total dose spread kernel, K^{source} is a source-blurring kernel, K_t^{beamlet} is a beamlet kernel, D is the resulting dose distribution, and F_t is a photon fluence distribution. Values for terms included in Equation 5.1 were determined using methods described in the following sections, and then this pencil beam formalism was used in an optimization routine to find spatially variant tungsten filtration patterns. This pencil beam calculation was chosen due to its relative efficiency compared to Monte Carlo, since optimizing using a solution space determined with Monte Carlo simulations was prohibitively computationally expensive. The filter designs calculated by the optimization routine were inserted into cone collimators in a Monte Carlo model of the x-ray beam. Simulations of standard (open) cones, as well as modulated cones, were used to compare the resulting dose distributions for a modulated and unmodulated orthovoltage stereotactic radiosurgery system.

5.1.1 Orthovoltage x-ray spectra

The UWMRRC's constant potential kilovoltage x-ray system was described in Chapter 3.1.1. To determine the effect of adding small amounts of tungsten to the UW250-M beam on resulting energy fluence, first, the open-source program SpekCalc (Poludniowski, 2007; Polud-

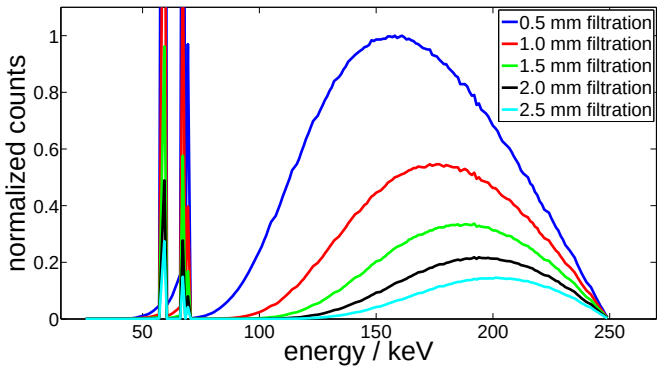

Figure 5.3: Photon spectra of the UW250-M beam following filtration through thicknesses of epoxy-infiltrated bonded tungsten ranging from 0.5 to 2.5 mm.

niowski and Evans, 2007; Poludniowski et al., 2009) v.1.1 (described in Section 4.2) was used for the theoretical calculation of photon spectra based on parameters of the UWMMRC orthovoltage unit and the UW250-M beam. Specific parameters included a tube potential of 250 kVp, target angle of 20°, and beam filtration of 0.99 mm aluminum, 3.22 mm copper, and 3 mm beryllium. The photon beam was also transported through 31.86 cm of air to approximate the spectrum at the same plane at which the phase space was tallied in the validated EGSnrc model described in Section 3.1.2. Next, the spectrum of the phase space generated by the validated EGSnrc model was tallied using the BEAMDP utility. These two spectra are shown in Figure 5.2. While the SpekCalc spectrum accomplishes a reasonable approximation of the validated model spectrum, the two results differ to an extent that it was deemed preferable to use the more accurate Monte Carlo model to examine the effects of added filtration material.

To modulate the beam, the filtration material was modeled as a homogeneous mixture of a bonded tungsten, infiltrated with epoxy (4% organic material and 96% tungsten by weight, with density of 11.2 g/cm^3) based upon information available from the prototyping firm RP+M (Avon Lake, Ohio) commissioned by this work, as well as an independent compositional analysis, described in Section 6.2. Using the EGSnrc user code DOSRZnrc (Rogers et al., 2011), particles were transported from the validated EGSnrc model primary

phase space through different thicknesses of attenuating material, and secondary phase spaces were tallied at 62.5 cm from the focal spot. The BEAMDP utility was again used to tabulate the phase space photon spectra for various filtration thicknesses, and these results are included in Figure 5.3. As an attenuating, high-density material, epoxy-infiltrated bonded tungsten was found to change the resulting fluence and energy fluence significantly without requiring large thicknesses, so the material was deemed appropriate for this work.

5.1.2 Pencil beam model kernel generation

Values for the input kernels K^{source} and K_t^{beamlet} in Equation 5.1 were generated using computational methods. Beamlet kernels (K_t^{beamlet}) were modeled using the EGSnrc user code DOSRZnrc. A point source was simulated emitting energies sampled from the primary phase space from the benchmarked BEAMnrc model. The point source was modeled to emit a square-collimated beam, (0.2×0.2) mm^2 at 100 cm from the source, incident on a given thickness of epoxy-infiltrated bonded tungsten. A cylindrical water phantom (radius 25 cm, height 30 cm) was modeled with the cylinder's axis parallel to the beam axis, with 95 cm between the source and the phantom surface. Dose was tallied at 5 cm depth with concentric cylindrical ring voxels, with radial boundaries spaced evenly 0.02 mm apart, and with shell height of 0.25 mm. Simulations were run for filter thicknesses of 0.5 to 5 mm, in 0.5 mm increments. Photon cross-section enhancement was used as a variance reduction technique for the tally cells within the plane of interest after it was determined that the technique did not significantly alter the simulation results. Transport parameters were the same as previously described. 5×10^9 particles were run for each simulation. The resulting dose distributions were used as beamlet kernels, indexed by thickness of attenuating material t, in Equation 5.1.

The source-blurring kernel term, K^{source}, from Equation 5.1, was determined using dose distributions derived from the EGSnrc Monte Carlo model and from the summed contributions of beamlet kernels. First, a circularly symmetric, variable-thickness epoxy-infiltrated

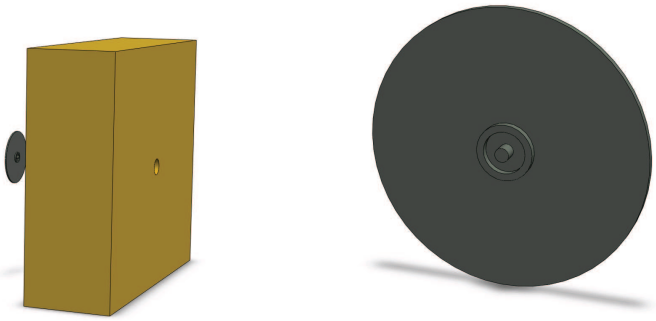

(a) (b)

Figure 5.4: Renderings in three-dimensional Computer Aided Design software of (a) an optimized epoxy-infiltrated bonded tungsten filter ready to be inserted into a 3.175 cm-thick leaded brass collimator, and (b) a close-up view of the ring pattern on the filter.

bonded tungsten filter was inserted into the aperture of the leaded brass collimator within the Monte Carlo model (Figure 5.4). Particles were transported from the primary phase space through the collimator and filter assembly to a water phantom, and dose from the modulated field was tallied at 5 cm following the same methods as previously described. Next, a corresponding dose distribution was calculated from the beamlet kernel contributions by selecting the beamlet kernels based on the filter thickness at that point along the beam path, and summing the contribution from all kernels. Finally, the source-blurring kernel was determined by using a Lucy-Richardson deconvolution (Lucy, 1974; Richardson, 1972) of the two distributions. This process is illustrated in Figure 5.5. Following optimization of filter geometry using the Genetic Algorithm search heuristic, dose-to-water distributions were calculated using Monte Carlo methods (to be detailed in Sections 5.2 and 5.3). Based on these results, the input filter geometry was adjusted, and the process for generating K^{source} was repeated iteratively.

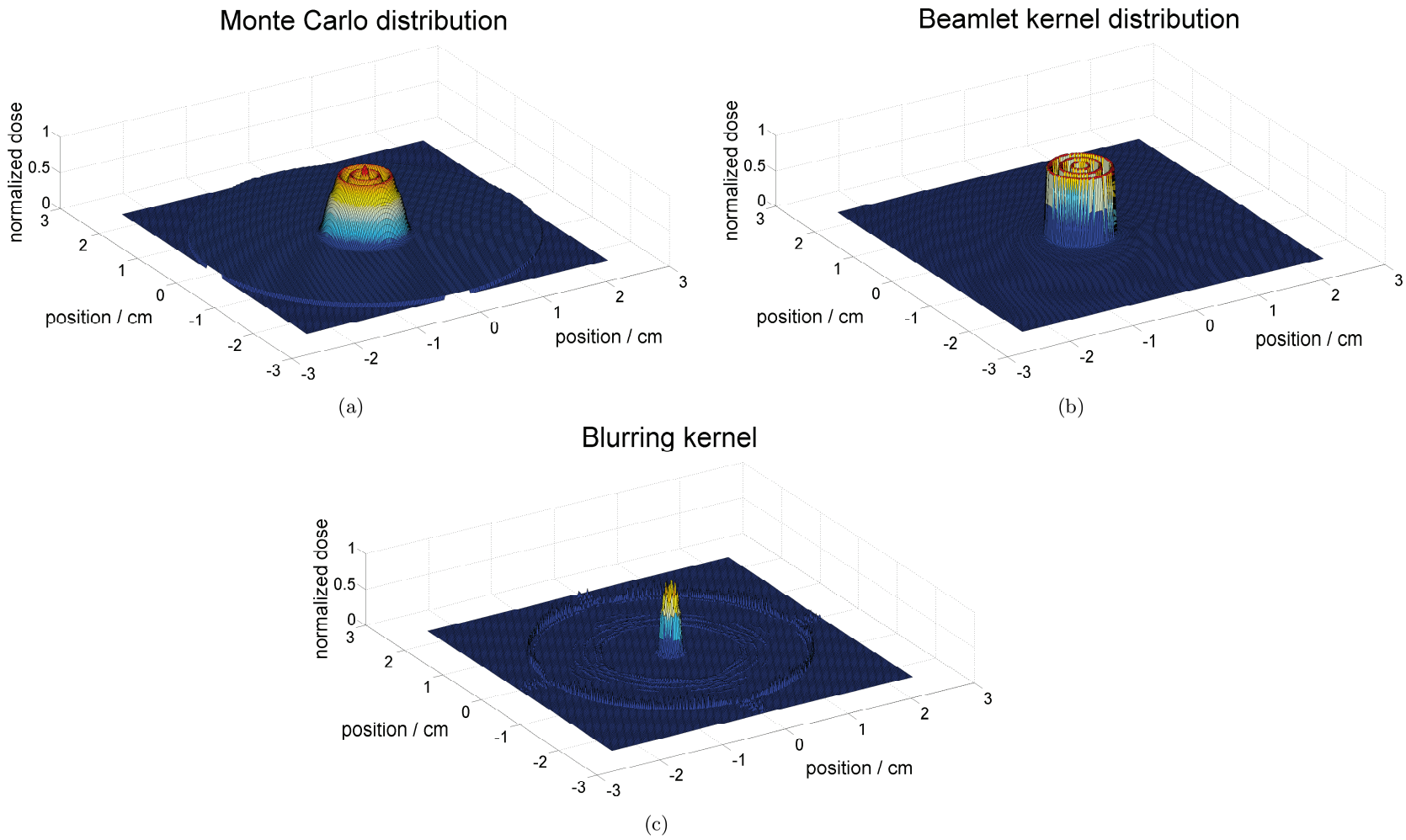

Figure 5.5: Three-dimensional representations of the steps to determine a source-blurring kernel: (a) a dose distribution from a modulated field is simulated using the EGSnrc Monte Carlo model, (b) a corresponding dose distribution resulting from the same irradiation geometry is generated by summing the beamlet kernel contributions, and (c) the source-blurring kernel is found by deconvolving the beamlet kernel distribution from the full Monte Carlo distribution.

5.2 Mathematical optimization methods

The model described and used in Chapter 4 was used to optimize a pencil beam-derived design. The primary goal in optimization mathematics may be summarized as finding the "best" option from all available options. In general, this involves minimizing some real-valued objective function f, (or equivalently, maximizing f by minimizing $-f$) given a set of decision variables that are part of a constraint set:

$$\begin{aligned} &\text{minimize} \quad f(\vec{x}) \\ &\text{subject to} \quad \vec{x} \in \Omega. \end{aligned} \tag{5.2}$$

The objective function, $f : \mathbb{R}^n \to \mathbb{R}$, uses the vector $\vec{x} = [x_1, x_2, x_3, ..., x_n]^T$ of feasible solutions, made up of independent variables that represent a subset of $\mathbb{R}^n$. This is an example of a constrained problem, because the decision variables must be contained within the feasible set Ω. For the special case that the feasible set is expanded such that $\Omega = \mathbb{R}^n$, the problem is unconstrained (Chong and Żak, 2001).

The feasible set may be convex, meaning the set contains all line segments between each pair of its points (Pedregal, 2004). For example, a set K in $\mathbb{R}^n$ is convex if for every pair of vectors $\vec{x}, \vec{y} \in K$, the segment joining them is also contained in K:

$$t\vec{x} + (1-t)\vec{y} \in K, \quad t \in [0,1]. \tag{5.3}$$

Similarly, the objective function f is convex if its epigraph (the set of points on or above the graph of f) forms a convex set. If both the feasible set and the objective function are convex, then the local minimum is also the global minimum. In real-world problems, however, both the feasible set and objective function may not be convex, and there may be multiple local minima along with the single global minimum (Chong and Żak, 2001). In this case, if the real-valued function $f : \mathbb{R}^n \to \mathbb{R}$ is on the set $\Omega \subset \mathbb{R}^n$, then a local

minimum exists at $\vec{x^*}$, where $\vec{x^*} \in \Omega$. For this local minimum, there exists some $\varepsilon > 0$ such that $\left\|\vec{x} - \vec{x^*}\right\| < \varepsilon$ and $f(\vec{x^*}) \leq f(\vec{x})$ on some region around $\vec{x^*}$.

5.2.1 Previous high-energy fluence modulation optimization

Previous work (Bender, 2014) described in Section 2.4.1 optimized the position of needles within a linear accelerator SRS cone to approximate a rectangular function dose distribution using MATLAB's optimization tools. In many of MATLAB's optimization routines, an objective function is minimized subject to inequality and equality constraints that are real-valued functions (Güler, 2010). These problems may be written:

$$\begin{aligned} \text{minimize} \quad & f(\vec{x}) \\ \text{subject to} \quad & \vec{h}(\vec{x}) = 0 \\ & \vec{g}(\vec{x}) \leq 0, \end{aligned} \tag{5.4}$$

where $f : \mathbb{R}^n \to \mathbb{R}$, $x \in \mathbb{R}^n$, as well as $\vec{h} : \mathbb{R}^n \to \mathbb{R}^m$, $\vec{g} : \mathbb{R}^n \to \mathbb{R}^p$, and $m \leq n$ (Chong and Żak, 2001). For nonlinear problems, the objective function, the constraints, or both are permitted to be nonlinear.

In MATLAB's notation, optimization routines find the minimum of the problem specified by:

$$\min_{\vec{x}} f(\vec{x}) \text{ such that } \begin{cases} A \cdot \vec{x} \leq \vec{b} \\ Aeq \cdot \vec{x} = \overrightarrow{beq} \\ \overrightarrow{lb} \leq \vec{x} \leq \overrightarrow{ub} \end{cases}, \tag{5.5}$$

where $\vec{b}$ and $\overrightarrow{beq}$ are vectors, A and Aeq are matrices, and $f(\vec{x})$ is a function that returns a scalar (The MathWorks, Inc., 2000).

The work described in Section 2.4.1 used a fluence optimization with MATLAB's *fmincon* routine (The MathWorks, Inc., 2012), a routine that handles a type of nonlinear pro-

gramming (NLP) called constrained nonlinear multivariable optimization. Two major approaches to solving problems of this type are penalty methods and sequential quadratic programming (SQP) methods. Penalty methods convert the constrained problem to an unconstrained problem, and impose either penalties for constraint violations or barrier terms to prevent exiting the feasible region (Forst and Hoffmann, 2010). SQP methods are algorithms that convert the problem into a series of quadratic optimization problems, which are easier and less computationally expensive to solve than the original problem. The *fmincon* routine used in the work of Bender (2014) employed the "Active Set" algorithm, which uses SQP methods.

Like many optimization algorithms, *fmincon*'s SQP algorithm is based on finding numerical solutions to the Karush-Kuhn-Tucker (KKT) system of equations. The KKT Theorem supposes that f, $\vec{h}$, and $\vec{g}$ from Equation 5.4 are continuously differentiable at $\vec{x^*}$ (i.e., let f, $\vec{h}$, $\vec{g} \in C^1$). If $\vec{x^*}$ is a regular point (a point $\vec{x^*}$ is *regular* if the gradients of the constraints, $\nabla h_1(\vec{x^*})$, ..., $\nabla h_m(\vec{x^*})$, and $\nabla g_1(\vec{x^*})$, ..., $\nabla g_j(\vec{x^*})$, are linearly independent) and if $\vec{x^*}$ is a local minimum satisfying the constraints given by $\vec{h}$ and $\vec{g}$, then there exists a Lagrange multiplier vector $\vec{\lambda^*} \in \mathbb{R}^m$ and a KKT multiplier vector $\vec{\mu^*} \in \mathbb{R}^p$ such that

$$\begin{gathered} \vec{\mu^*} \geq \vec{0}, \\ \nabla f(\vec{x^*}) + \vec{\lambda^*}^T \nabla \vec{h}(\vec{x^*}) + \vec{\mu^*}^T \nabla \vec{g}(\vec{x^*}) = \vec{0}^T, \\ \vec{\mu^*}^T \vec{g}(\vec{x^*}) = 0. \end{gathered} \tag{5.6}$$

Previous work by Bender (2014) minimized the integral of absolute deviations between a pencil beam-calculated dose distribution and a rectangular function over a finite field size, and optimized using 6 MV beam fluence, and without having to track energy fluence specifically. The current work also optimized using MATLAB's optimization tools, but the assumption regarding continuously differentiability of the KKT Theorem breaks down under the current framework. Therefore, an altogether different class of optimization technique was pursued and executed.

5.2.2 Genetic Algorithm search heuristic

Three broad types of search and optimization techniques may be used for optimization problems, classified as calculus-based, enumerative (or exhaustive), and random (Goldberg, 1989; Haupt and Werner, 2007). Calculus-based methods involve the study of gradients, and enumerative methods evaluate the objective function at every possible point within a search space. As discussed in the previous section, this work sought to optimize using decision variables restricted to be discrete. Calculus-based methods were therefore deemed inappropriate for an inherently discontinuous and non-differentiable problem, and enumerative methods were abandoned for lack of efficiency. Therefore, random search algorithms, which incorporate stochastic processes in their execution, were chosen for this work. Because of the discrete variable restriction, integer programming (IP) methods were investigated. These methods generally include branch-and-bound algorithms, branch-and-cut routines, and heuristics (Pachamanova and Fabozzi, 2010). A Genetic Algorithm (GA) search heuristic is a type of IP-randomized search algorithm based on basic tenants of natural selection and genetics (Sivanandam and Deepa, 2008). The method was first proposed by Holland (1975) as a type of evolutionary computation—an algorithm that imitates living beings to solve optimization problems (Gen and Cheng, 2000). GAs have been employed in a variety of applications, including problems in computer science, biology, engineering, finance, and social sciences (Davis and Steenstrup, 1987; Goldberg, 1989).

Using GAs, a population of potential solutions evolves iteratively under given constraints to find optimal solutions using the basic concept of survival of the fittest. Each iteration of the population is termed a generation, and the "fitness" of each solution in a given generation is measured. The fittest solutions (those that minimize the objective function) are used preferentially to form the subsequent generation based on chosen rules of selection ("elitism"), recombination ("crossover"), and mutation (Najim et al., 2004; Reeves and Rowe, 2003; Whitley, 1994). Because they do not require taking derivatives of an objective function,

GAs are able to optimize problems involving discrete variables and objective functions with discontinuities (Hamilty and Rahmat-Samii, 1999; Haupt and Haupt, 2004).

Although gaining in popularity in part due to their suitability for a variety of applications, GAs are not without their own set of limitations. First, if the search space is smooth and unimodal, gradient-search methods tend to outperform GAs in terms of efficiency. In addition, solutions in GAs are only graded in comparison to other known solutions and therefore stop criteria (aside from explicitly stated restrictions from the user such as number of generations) are not usually clear. Further, GAs cannot guarantee a provable, globally optimal solution (Melanie, 1999). Therefore, if the space is small, exhaustive search methods are preferable; however, when given certain conditions on the problem domain, GAs do tend to converge on globally optimal solutions (or close to them) even when handling large and complicated search spaces (Davis and Steenstrup, 1987). Although all optimization methods perform better with objective functions that are relatively fast to compute, GAs in particular perform poorly with cumbersome objective functions due to the replacement of some or all of each population at each generational iteration and the subsequent evaluation of all offspring (Whitley, 1994). For this reason, GAs converge slowly when computed serially—though in a parallel computing environment, each processor may evaluate separate functions simultaneously (Haupt and Haupt, 2004; Messac, 2015).

5.2.3 Filter optimization routine at the UWMRRC

Initial work was completed optimizing on monoenergetic fluence, with the calculation grid size equal to the resolution of the spatial energy steps. This is analogous to traditional intensity modulated radiation therapy (IMRT) inverse planning, for which fluence intensity profiles are optimized, using user-defined penalties and constraints, to produce a desired dose distribution. Dose is calculated based on the fluence intensity profiles and evaluated; if it is satisfactory, MLC leaf-sequencing files are generated to convert the ideal fluence to deliverable MLC segments and the final dose distribution is calculated (Chui et al., 2001).

This final step may result in a degradation of the optimized plan to the deliverable plan. Instead of this two-step optimization/conversion process, plans may be optimized directly based on MLC settings, as with, for example, the "Direct Machine Parameter Optimization" routine (Hårdemark et al., 2004) available with Pinnacle treatment planning software. This process avoids optimizing and approving a plan, only to have the plan fail final evaluation following conversion to deliverable MLC settings. A comparable process was completed for this project: instead of optimizing dose distributions based on energy fluence, dose profiles were optimized directly based on filtration thicknesses.

For this application, it was unnecessary to specify equality and inequality constraints (aside from upper and lower bounds on $\vec{x}$), and the terms were omitted. MATLAB's *ga* routine, designed for GA optimization, was used for this work. In MATLAB notation, the terms in Equations 5.4 and 5.5 start at seed position $\overrightarrow{x_0}$ and the routine searches for a minimum $\vec{x}$ for the function $f(\vec{x})$, with a set of lower and upper bounds on $\vec{x}$ designated by $\overrightarrow{lb}$ and $\overrightarrow{ub}$, respectively. The user may specify algorithm preferences using an *options* parameter, such as the termination tolerance on the function value, the termination tolerance on $\vec{x}$, the maximum number of function evaluations allowed, etc. Finally, the *IntCon* parameter was used to require that specified variables take integer values (the calculated kernel datasets). Due to the stochastic nature of GAs, slightly different results are expected for each run, so multiple runs were completed to build confidence in the result (Messac, 2015). The objective function for the routine was a sum of squares of the differences between the calculated pencil beam dose distribution at depth and a rectangular function dose distribution from a single beam. The optimization was run for cone sizes of 5, 6, 8, and 10 mm at 5.0 cm depth. Calculations were completed with the collimator plane (distal from the source) positioned at 62.5 cm from the source. The optimization was constrained to allow for changes in filter thicknesses a minimum of 0.5 mm in the plane perpendicular to the beam axis, projected to the collimator plane. The pencil beam optimization was assumed to be nondivergent (no

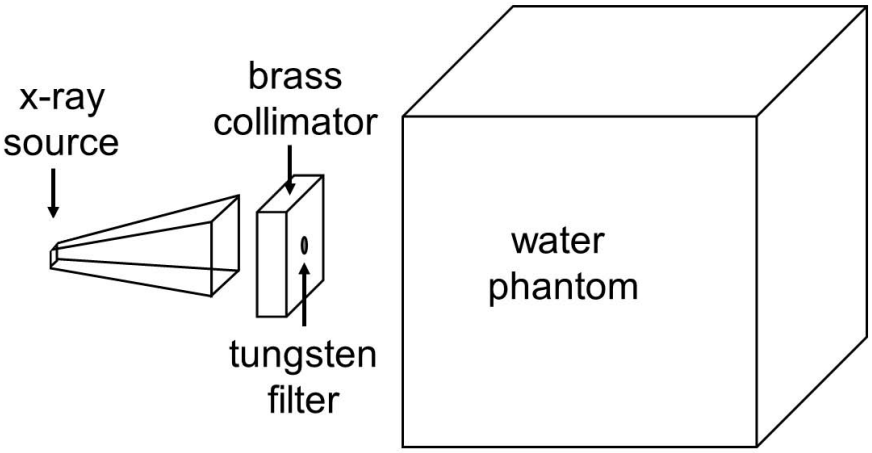

Figure 5.6: Monte Carlo simulation geometry for single beam dose-to-water distributions. 250 kVp photons from the orthovoltage unit are transported through a leaded brass collimator that accommodates a variable-thickness bonded tungsten filter, and dose to water is tallied in a water phantom in a 100 cm SAD irradiation geometry

kernel tipping). Optimal filter designs were then used to find simulated dose distributions in water.

5.3 Simulated dose distributions in water

A simple schematic Monte Carlo geometry used in this work is included in Figure 5.6. BEAMnrc was used to transport particles from the primary phase space through a 3.175 cm-thick cone collimator with various aperture diameters using the FLATFILT component module. The collimator material was modeled as a homogeneous mixture of a leaded brass alloy (by weight, composed of 61.5% copper, 2% lead, and 36.5% zinc, with density of 8.47 g/cm^3) based on information from the manufacturer (Sequoia Brass & Copper, Inc., Hayward, CA). The collimator was simulated either as open or as modulated with the optimized filter design found through GA optimization. Secondary phase spaces were tallied in air downstream of the collimator. These phase spaces were used as sources for simulations

in which dose to water was tallied at depth in water phantoms. Simulated geometries included single-beam profiles, as well as 4π distributions.

5.3.1 Simulated single-beam profiles

The EGSnrc user code DOSRZnrc was used to simulate a water phantom at 100 cm SAD, for dose planes at 2.5, 5.0, and 7.5 cm depths. For three depths, simulations were run for the filtered cones, as well as for unfiltered (open, unmodulated) cones. Dose was tallied in concentric cylindrical ring voxels, with radial boundaries spaced evenly 0.25 mm apart, and each voxel at a height of 0.25 mm. Photon cross-section enhancement was used as a variance reduction technique for the tally cells within the plane of interest. Transport parameters were consistent with those previously described, except 3×10^9 histories were run. Simulated dose distributions were analyzed for beam profile flatness and penumbra widths. Examples of calculated dose profiles at depth are included in Figure 5.7. For each depth, cone size, and filtration combination, the 80–20% and 90–10% penumbrae were calculated, as well as the profile flatness as defined by AAPM's code of practice for radiotherapy accelerators (Nath et al., 1994):

$$F = \frac{M - m}{M + m} \times 100\%, \tag{5.7}$$

where M and m are the maximum and minimum dose values, respectively, defined for the central 80% of the beam width as measured from the profile full width at half maximum (FWHM). Summaries of these flatness and penumbra results are included in Tables 5.1 and 5.2. For all configurations tested, the modulated beams achieved improved penumbra widths and flatness statistics at depth compared to the open, standard beams. The attempt to form a very sharp gradient using optimization techniques has been shown in other radiotherapy systems to produce an oscillation or ringing pattern (Kissick et al., 2007) as a result of the Gibbs phenomenon (Gibbs, 1898, 1899). This pattern was noted in the optimized profiles, visible in Figure 5.7.

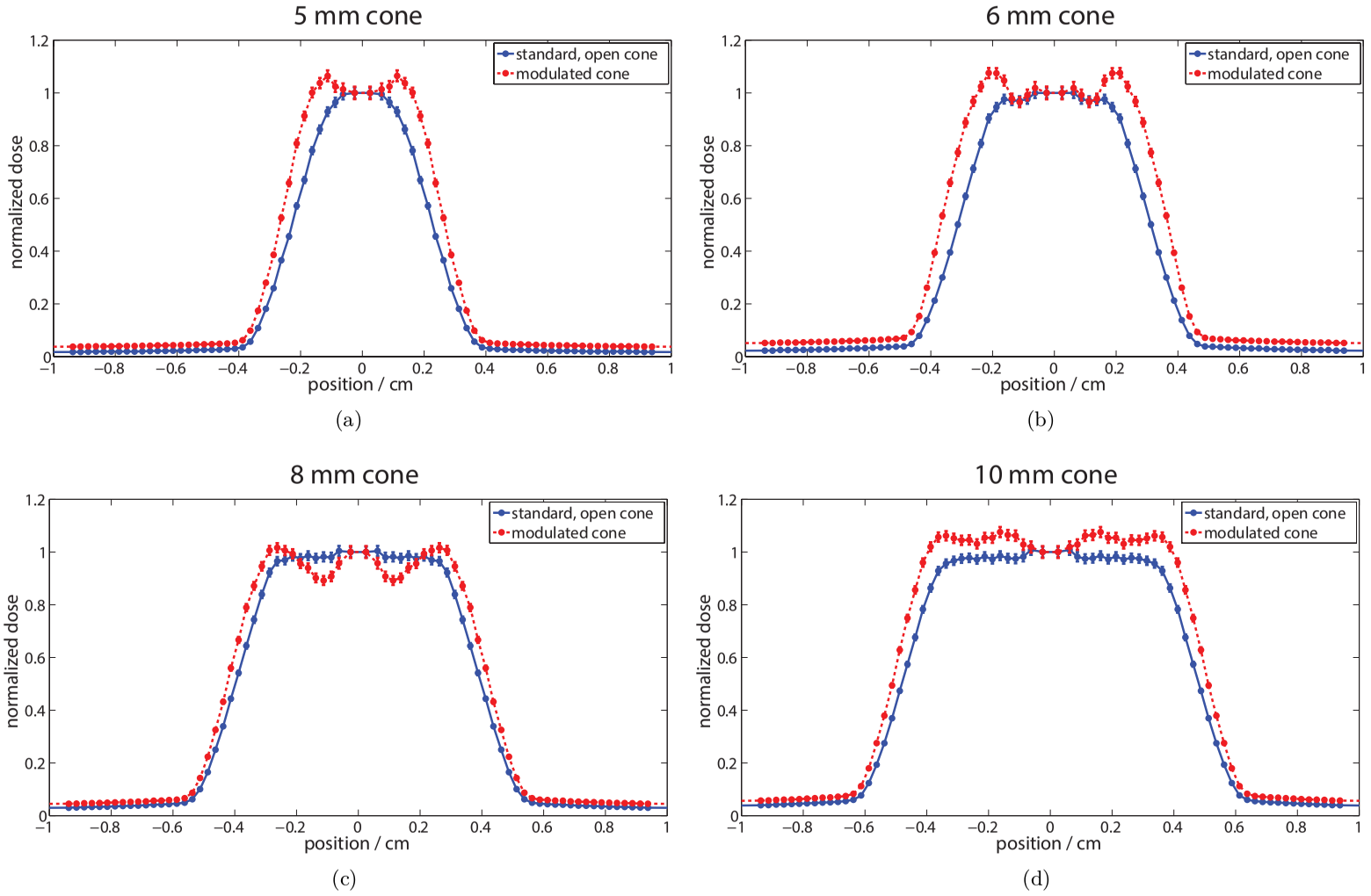

Figure 5.7: Single-beam dose profiles calculated with EGSnrc, normalized to the central axis dose, at 5.0 cm depth for (a) 5 mm, (b) 6 mm, (c) 8 mm, and (d) 10 mm cones. Standard (open) distributions are shown as a solid blue line, and modulated (filtered) distributions are shown as a dashed red line. Error bars represent the calculated full uncertainty at the $k = 1$ level.

5.3.2 TrueBeam single-beam profiles

To compare the simulated orthovoltage profiles with analogous linear accelerator data, the Integrated Conical collimator Verification and Interlock (ICVI) system conical collimators representative beam data for Eclipse treatment planning system were downloaded from the MyVarian application (Varian Medical Systems, Inc., Palo Alto, CA). This data set was acquired from multiple TrueBeam linear accelerators using an EDGE diode detector (Sun Nuclear, Inc., Melbourne, FL) in an IBA Blue water phantom (IBA Dosimetry GmbH, Schwarzenbruck, Germany) and is meant to represent average TrueBeam SRS profiles.

Penumbra and flatness statistics were calculated using this data for 6 MV beams with cone collimators of diameters 5, 7.5, and 10 mm, at 5 cm depth and 100 cm source-to-surface distance (SSD). These results are included in Table 5.3. Though the cone sizes and irradiation geometries are not exactly the same as those simulated in the orthovoltage cases (with slight variations in SSD and cone sizes), the modulated orthovoltage beams achieve superior penumbra and flatness statistics compared to the linear accelerator values.

5.3.3 Simulated 4π distributions in water

Because SRS treatments are rarely delivered in a single-beam geometry, simulations were performed in an isotropic, 4π irradiation geometry. Surface dose is of concern for an orthovoltage system compared to a high-energy linear accelerator or ^{60}Co beam, so dose was tallied in this geometry to examine dose at very shallow depths.

The egspp EGSnrc C++ class library was used to model a 10 cm-radius sphere of water in air, irradiated by the standard beam and the modulated beam using secondary phase space

Table 5.1: Single-beam penumbra statistics for modeled beam profiles at 2.5, 5.0, and 7.5 cm depths. Beams were simulated incident on a large cylindrical water phantom in a 100 cm SAD irradiation geometry. Simulations were run for standard (open) cones, as well as for modulated cones with optimized filters included in the model.

		80%–20% penumbra			90%–10% penumbra		
Cone size	depth	standard	modulated	percent	standard	modulated	percent
(mm)	(cm)	(mm)	(mm)	improvement	(mm)	(mm)	improvement
5	2.5	1.48	1.25	16	2.15	1.83	15
6	2.5	1.50	1.28	15	2.11	1.90	10
8	2.5	1.54	1.36	12	2.18	2.05	6
10	2.5	1.54	1.40	9	2.26	2.02	11
5	5.0	1.50	1.26	16	2.18	1.85	15
6	5.0	1.52	1.30	15	2.15	1.94	10
8	5.0	1.55	1.39	11	2.20	2.08	5
10	5.0	1.55	1.42	9	2.29	2.08	9
5	7.5	1.50	1.27	16	2.12	1.86	15
6	7.5	1.53	1.31	14	2.20	1.98	10
8	7.5	1.58	1.40	11	2.24	2.12	5
10	7.5	1.56	1.44	8	2.32	2.16	7

Table 5.2: Single-beam flatness statistics for modeled beam profiles at 2.5, 5.0, and 7.5 cm depths. Beams were simulated incident on a cylindrical water phantom in a 100 cm SAD irradiation geometry. Simulations were run for standard (open) cones, as well as for modulated cones with optimized filters included in the model.

Cone size (mm)	depth (cm)	standard (%)	modulated (%)	percent improvement
5	2.5	18.3	12.63	31
6	2.5	13.5	9.80	27
8	2.5	10.3	8.74	15
10	2.5	7.38	4.57	38
5	5.0	18.3	12.9	30
6	5.0	13.7	10.0	26
8	5.0	10.2	8.38	18
10	5.0	7.20	4.57	37
5	7.5	17.9	12.8	29
6	7.5	13.7	10.3	25
8	7.5	10.5	8.01	24
10	7.5	7.32	4.98	32

Table 5.3: Single-beam penumbra and flatness statistics for Varian TrueBeam ICVI SRS representative data for Eclipse taken at 5.0 cm depth, 100 cm SSD irradiation geometry. Cone sizes of 5, 7.5, and 10 mm are included.

Cone size (mm)	80–20% penumbra (mm)	90–10% penumbra (mm)	flatness (%)
5	1.39	2.45	15.3
7.5	1.60	2.95	13.0
10	1.74	3.30	9.71

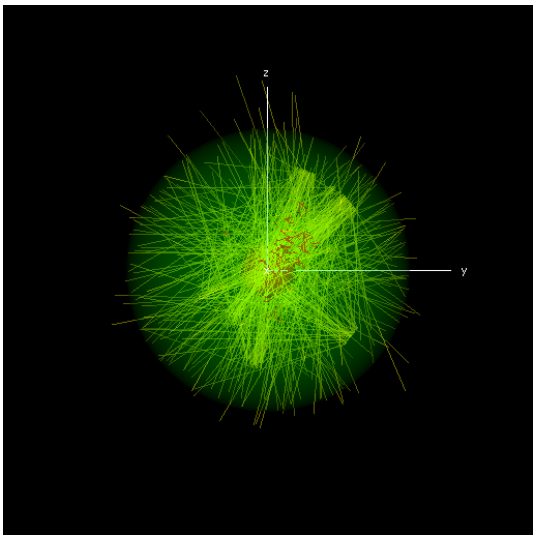

Figure 5.8: An example of an initial simulation used to approximate 4π geometry is shown using the EGSnrc C++ geometry viewer egs_view, with particle tracks turned on for visualization. The figure illustrates a simplified case with ten beam angles incident on isocenter for visual clarity, though initial work with translated and rotated phase spaces used 200 beam angles. Finalized distributions were simulated integrating over all possible angles for a true 4π geometry.

Table 5.4: Dose at 0.07 mm depth in a simulated 4π irradiation geometry of a 10 cm-radius spherical water phantom, in a 100 cm SAD irradiation geometry. Simulations were run for standard orthovoltage beams, modulated orthovoltage beam with optimized filters, and standard ^{60}Co beams. The dose at 0.07 mm is reported as a percentage of the isocenter dose, which was the point of maximum dose for all irradiation configurations.

Cone size (mm)	standard ^{60}Co (% isocenter dose)	standard orthovoltage (% isocenter dose)	modulated orthovoltage (% isocenter dose)
5	0.00021	0.0058	0.017
6	0.00037	0.0066	0.021
8	0.00057	0.0076	0.016
10	0.00081	0.0088	0.017

sources described previously. To compare with a higher energy source, a collimated ^{60}Co source was simulated as well, using an energy spectrum from the data of Mora et al. (1999). The water sphere was divided into concentric spherical shell voxels, with an inner sphere at a radius of 0.025 cm delineating the isocenter voxel, and spherical shell boundaries placed at 0.025 cm radial intervals. An additional boundary was placed at a radius of 9.986 cm within the 10 cm-radius spherical water phantom, to tally dose to a voxel with an average depth of 0.07 mm from the surface (denoted $D_{0.07\,\mathrm{mm}}$). Transport parameters were consistent with those previously described, except 5×10^{10} histories were run. Initial runs were completed with 200 phase spaces distributed about the water phantom uniformly, as described in Chapter 4 and pictured in Figure 5.8. These simulations were repeated, integrating over all possible beam angles for a true 4π irradiation geometry. Sample simulated 4π dose distributions are included in Figure 5.9.

One concern with using orthovoltage energies in a prototype stereotactic radiosurgery system is high dose at shallow depths. With conventional SRS megavoltage energies, there exists a skin-sparing effect resulting from a dose buildup region near the surface. To examine this phenomenon in the context of the 4π irradiation geometry, $D_{0.07\,\mathrm{mm}}$ was tallied in a 10 cm-radius spherical water phantom. The depth 0.07 mm was chosen because it has been used as a surrogate for the basal skin layer, (ICRP Publication 60, 1991; ICRU Report 39, 1985) and has previously been used interchangeably with surface dose (Akbas et al., 2016; Chen et al., 2010; Kry et al., 2012). Values for dose at 0.07 mm depth from a 4π isocentric irradiation geometry of a 10 cm radius sphere are included in Table 5.4. The mean dose within this shell voxel (averaged over all cone sizes) was $0.007\% \pm 0.001\%$ of the isocenter dose for the standard, open orthovoltage irradiation simulations, and $0.018\% \pm 0.002\%$ of the isocenter dose for the modulated, filtered simulations. The ^{60}Co simulations achieved the lowest dose within this voxel at $0.00049\% \pm 0.00026\%$. For every cone size, the modulated cones had higher dose at 0.07 mm depth than either the ^{60}Co or the orthovoltage

unmodulated cones; however, for every cone size, the modulated cone $D_{0.07\,\mathrm{mm}}$ values were $\leq 0.025\%$ of the isocenter dose, which was the voxel of maximum dose in the simulations.

In order to compare profile statistics from a modulated and an unmodulated 4π distribution, a new open 4π simulation was run with a revised cone size in order to compare distributions that both irradiate the same volume to 90% of the isocenter dose, assuming maximally conformal coverage of a spherical target with the exact same radius of the 90% isodose volume. The modulated 5 mm cone was compared to this new distribution. Both profiles irradiated a radius of 2.183 mm to the 90% isodose value, as seen in Figure 5.10.

The 80–20% penumbra was improved by 7% (2.858 mm compared to 2.649 mm), and the flatness was improved by 9% (17.26% compared to 15.67%) for the assumed maximally conformal 4π distributions.

5.4 Simulated dose distributions in bone and tissue material

5.4.1 Simulated single-beam dose to bone and tissue material

O'Malley et al. (2006) examined the ratio of dose to bone and dose to tissue using Monte Carlo simulations of a simplified cylindrical geometry irradiated by monoenergetic photons ranging in energy from 100 keV to 1 MeV. Their simulated phantom was composed of two semicylinders: one composed of tissue equivalent material and one of bone equivalent material as defined by ICRU Report 44 (1989). They modeled photons incident on the cylinder along the cylinder's axis, and tallied dose deposited at 5 cm depth to a 1 cm-thick disc in order to compare dose to bone versus dose to tissue.

Similar simulation work was completed here. The same composition for tissue and bone was used in DOSRZnrc (by weight, tissue was modeled as 10.5% hydrogen, 45.6% carbon, 2.7% nitrogen, and 60.2% oxygen, with a density of 1.03 g/cm^3, and bone was modeled as 4.6% hydrogen, 19.9% carbon, 4.1% nitrogen, 43.5% oxygen, and 18.7% calcium, with a

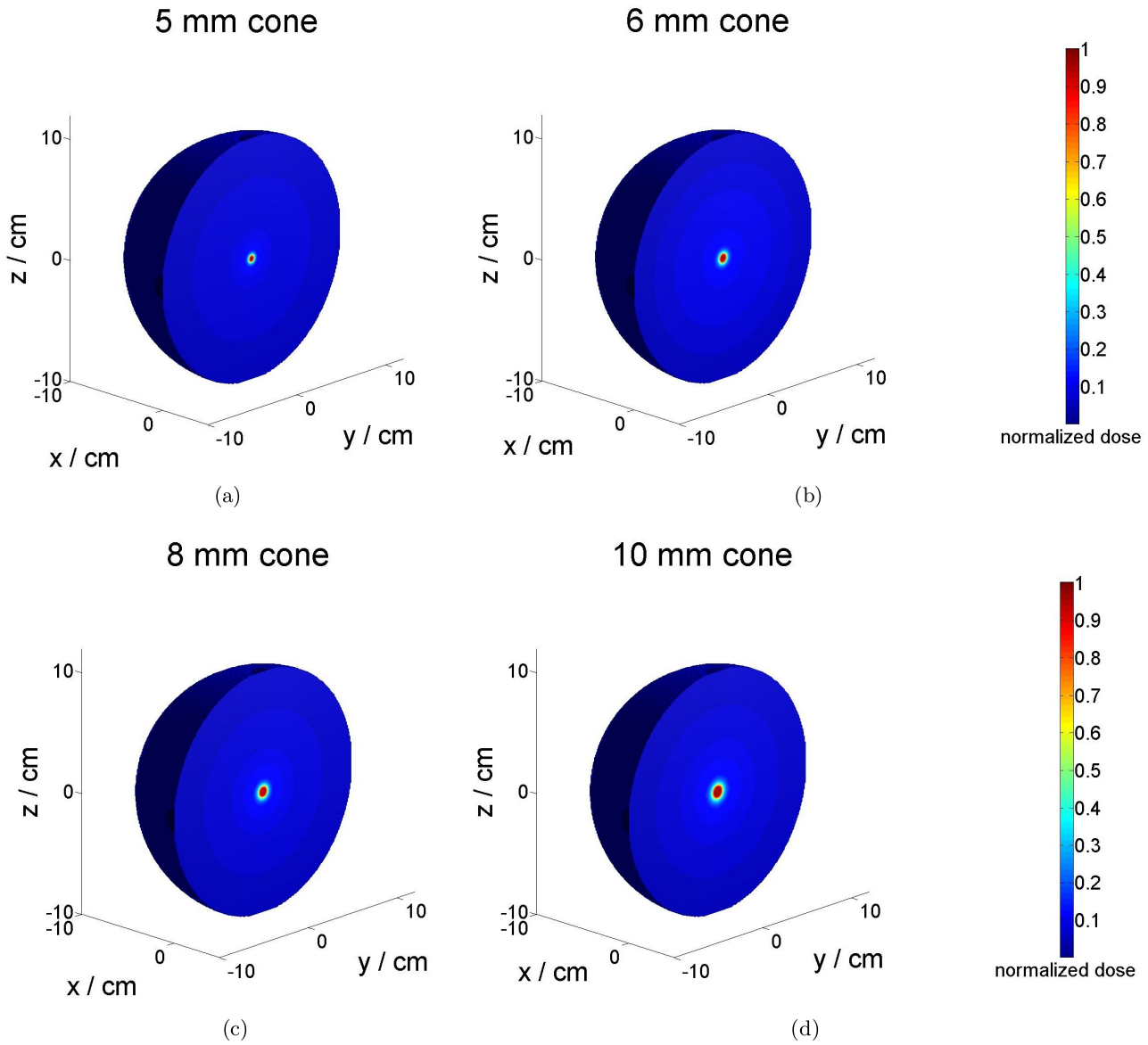

Figure 5.9: Cross-sectional views of three-dimensional dose distributions computed in EGSnrc for a 10 cm-radius sphere of water irradiated from an isocentric 4π geometry. Dose values are normalized to the maximum dose per starting particle. Pictured are distributions derived from modulated (filtered) cones for cone sizes of (a) 5 mm, (b) 6 mm, (c) 8 mm, and (d) 10 mm.

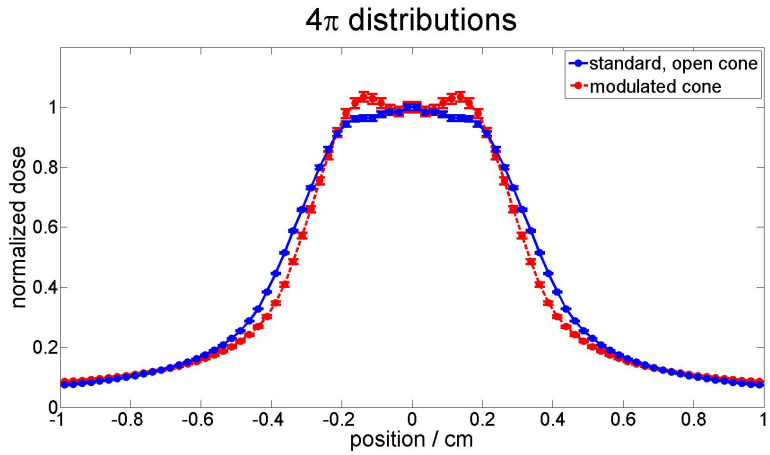

Figure 5.10: Dose profiles, normalized to the central axis dose, through a 10 cm sphere of water irradiated by an isocentric 4π beam geometry. The standard (open) distribution is shown as a solid line, and represents a profile from a cone size chosen to match the 90% isocenter dose radius of the 5 mm modulated (filtered) cone, which is shown as a dashed line. Error bars represent the calculated full uncertainty at the $k = 1$ level.

density of 1.68 g/cm). A point source was simulated emitting monoenergetic photons, photons with energies sampled from the primary phase space from the benchmarked BEAMnrc model of the 250 kVp beam, or photons with energies sampled from ^{60}Co spectrum data. For the monoenergetic photon simulations, beam energies of 100 keV to 1 MeV, in 100 keV increments, were simulated to verify the results of O'Malley et al., as well as 125, 150, 175, and 250 keV monoenergetic photons. A single 2.5 cm-radius cylinder of either tissue or bone material was used in each simulation order to avoid interface effects associated with a composite semicylinder phantom. The phantom was modeled with the cylinder's axis parallel to the beam axis, at 95 cm from the phantom surface. Transport parameters were the same as previously described.

Results are included in Figure 5.11. Though O'Malley et al. did not specify all the details of their simulation geometry, the qualitative shape of their results is similar to the results found here, with the ratio of dose deposition in bone to that in tissue rapidly decreasing with increasing beam energy, reaching a plateau at approximately 200 keV. This work confirms the findings of the previously published work, with the UW250-M beam falling

within the steep fall-off region of the bone-tissue dose ratio curve. Because the UWMRRC orthovoltage unit is maintained and NIST-matched only up to 250 kVp (with an effective energy of 145 keV), the maximum beam energy available was chosen for this work. A higher energy beam (with an effective energy beyond the steep portion of the bone-tissue dose ratio curve) would be preferable, and could be designed using the methodology described here, but the UW250-M beam was chosen because it was usable for measurements.

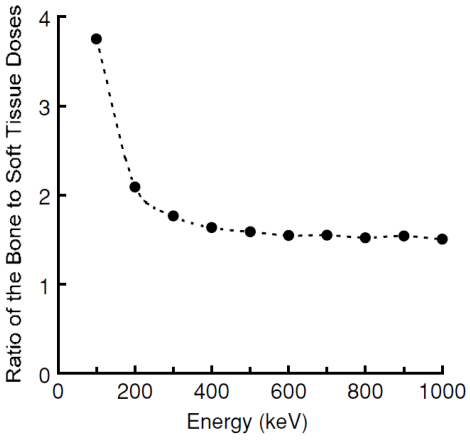

(a)

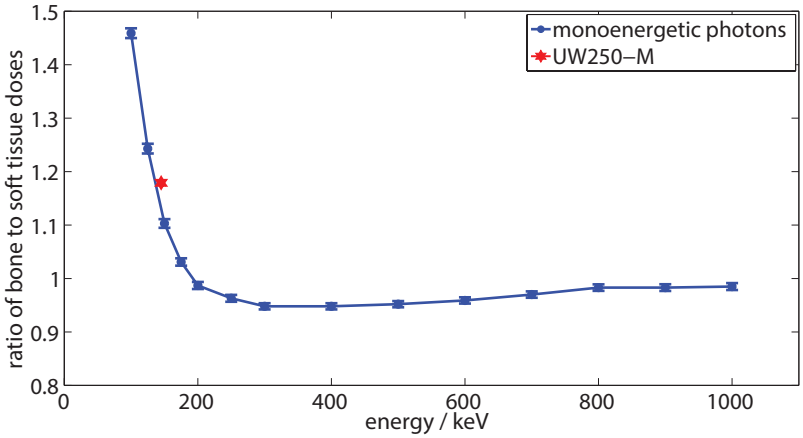

(b)

Figure 5.11: Bone to soft tissue dose deposition ratio as a function of incident photon energy. (a) Previously published results from O'Malley et al. (2006). Reprinted with permission from L. O'Malley et al., "Improvement of radiological penumbra using intermediate energy photons (IEP) for stereotactic radiosurgery," Physics in Medicine and Biology, 51 (10), 2537–2548, 2006. Copyright 2006, Institute of Physics and Engineering in Medicine, IOP Publishing. (b) Results from this work, with values normalized to those from ^{60}Co. Monoenergetic photon simulations are shown with solid blue circle markers and the UW250-M beam is shown with a red star marker positioned at its effective energy of 145 keV. Error bars represent the propagated statistical uncertainty associated with the Monte Carlo simulations.

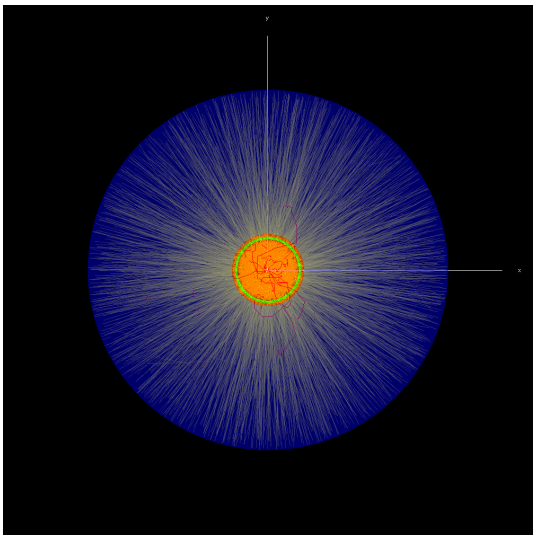

Figure 5.12: A cross section of the simulation used to approximate 4π geometry is shown using the EGSnrc C++ geometry viewer egs_view, with particle tracks turned on for visualization. The phantom is composed of tissue material, shown in red, and a 7 mm-thick spherical shell of bone material, shown in green, and the surrounding material is air, shown in blue. Photon tracks are shown in yellow and electron tracks are shown in red.

5.4.2 Simulated 4π distributions in bone and tissue material

To investigate the effect of sequentially positioning tissue and bone material along the beam path (such as would be the case when treating tissue downstream of bone), a 10 cm-radius spherical phantom was simulated using the egspp EGSnrc C++ library. The phantom was composed of tissue material but with a 7 mm-thick spherical shell of bone material placed 8 mm from the phantom surface in order to create a spherical scalp, skull, and brain geometry approximation (Li et al., 2007), as shown in Figure 5.12. The 10 mm modulated beam secondary phase space was used to simulate irradiation of the phantom in a 4π irradiation geometry, and dose to bone was tallied, as well as dose to tissue in the central 2.5 mm radius sphere. The ratio of dose deposited to the bone shell to dose deposited to tissue in the central focal target volume was found to be 0.0320 ± 0.0003. For small animal applications, it is noted that the treatment volume would be considerably

smaller and the skull thinner, with rat skull thicknesses approximately 0.5–1 mm, and mouse skull thicknesses approximately 0.2 mm (Cook, 1965; O'Reilly et al., 2011).

5.5 Uncertainty analysis

Similar to the uncertainty analysis included in Section 3.6.4, sources of uncertainty in the dose-to-water values (per starting particle) of the reported dose distributions calculated with EGSnrc include the statistical uncertainty associated with the simulations, as well as the uncertainties introduced by the electron stopping powers, the photon interaction cross sections, and the photon spectra used in the original validated BEAMnrc model (Muir and Rogers, 2010; Rogers and Bielajew, 1990; Zink and Wulff, 2012). Following the same methodology as previously described, the mean excitation energy, I, for each simulated material was varied by 10% using the ESTAR program to generate both modified density corrections and a new PEGS file with adjusted collision stopping powers. Simulations were repeated with the adjusted I values. Photon cross sections were scaled by 5% in the BEAMnrc and DOSRZnrc simulations, and compared to the results with the XCOM cross-section library. Finally, a point source with a spectrum either derived from the full BEAMnrc validated model, or measured with the high-purity germanium spectrometer (Section 3.1.1), was simulated in DOSRZnrc incident on an unfiltered leaded brass collimator, and dose to water was tallied in a water phantom. The maximum difference between the two resulting dose distributions was used to estimate the uncertainty due to photon spectra. For all cases, the maximum observed differences between simulation results found using the transport parameters used in this work, and those found by parameters used to quantify uncertainty, were used to estimate uncertainty, and triangular distributions were assumed. A sample uncertainty budget is included in Table 5.5.

Table 5.5: Sample uncertainty budget for the Monte Carlo-determined dose-to-water values. All values are expressed in percent.

Parameter	Type A	Type B
statistical computational uncertainty	0.54	
electron stopping powers		1.4
photon cross sections		0.40
photon spectra		0.55
quadratic sum	0.54	1.6
A and B quadratic sum	1.7	
Total combined uncertainty	1.7% ($k = 1$)	
Expanded total uncertainty	3.4% ($k = 2$)	

5.6 DGI analysis

Chapter 4 included an analysis of the trade-off between prescription isodose and dose gradients for theoretical 4π dose distributions created using monoenergetic orthovoltage beams and a realistic 250 kVp x-ray spectrum calculated with SpekCalc. A similar analysis may be performed using the 4π dose distributions calculated using the full EGSnrc model, and shown in Figure 5.9. As stated in Equation 4.1, the dose gradient index is the ratio of the 50% prescription isodose volume to the 100% prescription isodose volume. The relationship between prescription isodose and DGI for the orthovoltage Monte Carlo-calculated 4π dose distributions is included in Figure 5.13. As was found in Chapter 4, for all configurations examined, there existed a prescription isodose at which the first derivative of the DGI function was zero and at which the second derivative was positive, indicating that a local minimum existed. These results are summarized in Table 5.6. For all cone sizes, the DGI for the modulated cones was less than that for the unmodulated cones for all prescription isodose values >70%.

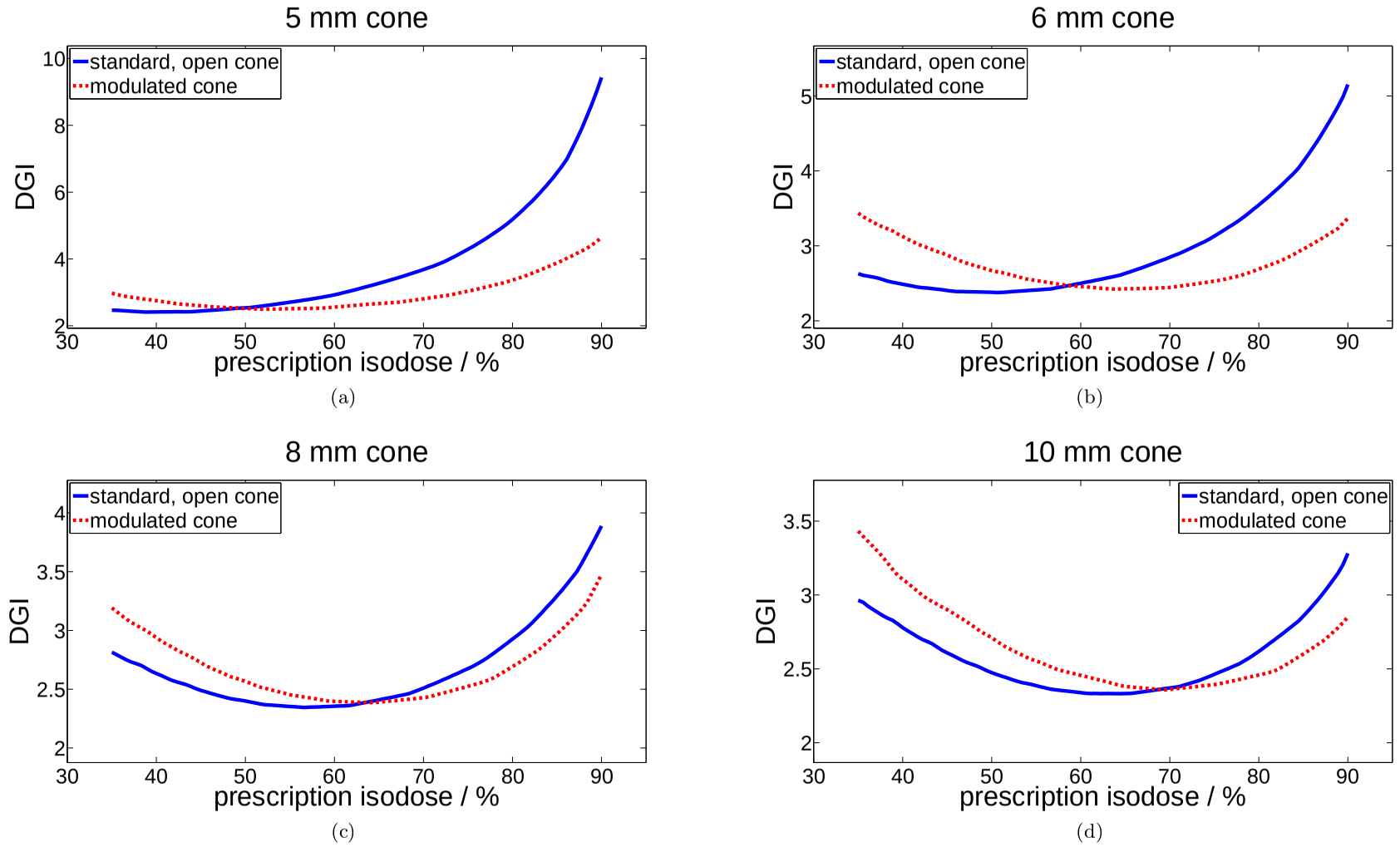

Figure 5.13: Trade-off between DGI and prescription isodose for cone sizes (a) 5 mm, (b) 6 mm, (c) 8 mm, and (d) 10 mm for a 4π isotropic delivery about a 10 cm-radius sphere of water. Standard (open) distributions are shown as a solid blue line, and modulated (filtered) distributions are shown as a dashed red line.

Table 5.6: DGI results calculated from three-dimensional dose distributions simulated from a 4π irradiation geometry for standard (open) and modulated (filtered) distributions.

Cone size (mm)	Beam modulation	Rx resulting minimum DGI (%)	Minimum DGI
5	open	38.9	2.41
6	open	50.6	2.38
8	open	56.7	2.35
10	open	64.4	2.33
5	modulated	52.1	2.50
6	modulated	63.7	2.42
8	modulated	64.2	2.39
10	modulated	69.4	2.36

5.7 Application of collimator and filter designs

This work has described the mathematical optimization techniques as well as the Monte Carlo simulations used to design collimator and filter assemblies in a modulated, orthovoltage SRS system prototype. Simulation results indicate that modulated beams are able to achieve improved flatness and penumbra statistics compared to unmodulated beams. Dose at 0.07 mm depth was consistently higher for the modulated beams compared to unmodulated beams in a simulated 4π irradiation geometry, but was $\leq 0.025\%$ of the maximum dose at isocenter. Results from this optimization were used to design orthovoltage filtered cone prototypes, described in Chapter 6.

Chapter 6

Prototype construction and characterization

Based on the results from Chapter 5, collimator and filter assembly prototypes were constructed, along with a positioning support structure for alignment within the UW250-M beam line. The fabrication of the prototypes is discussed in this chapter as well as the characterization of the system dosimetry using radiochromic film measurements in a water phantom.

6.1 Cone collimator construction

Four $(9 \times 10 \times 3.175)\,\mathrm{cm}^3$ nondivergent cone collimators were constructed using a 0.625 in-thick plate of high-leaded machining brass (Alloy 353, composed nominally of 61.5% copper, 2% lead, and 36.5% zinc, the composition used in the Monte Carlo modeling in Chapter 5). Transmission of the UW250-M beam through the solid brass was measured to be $0.12\% \pm 0.02\%$ using a $15\,\mathrm{cm}^3$ active volume parallel plate chamber. Apertures were milled into the collimators using precision reamers for cone diameters (projected to the plane of measurement) of 5, 6, 8, and 10 mm. Dowel pins were used to position filters temporarily

on the collimator plane distally from the source. Filters were centered within the aperture using the dowel pins for filtered measurements but could also be removed for open cone measurements. Photographs of the cone collimators are shown in Figure 6.1.

6.2 Manufacturing of filters

Variable-thickness filters were manufactured to project specifications by the outside prototyping firm RP+M (Avon Lake, Ohio), using a binderjetting printer with the capability of creating tungsten parts. Binderjetting is a process that involves the deposition of multiple layers sequentially—a technique commonly referred to as additive manufacturing. The layers of tungsten powder are interspersed with layers of epoxy binder, which are partially cured before the subsequent deposition of additional layers. The part is built layer by layer, referred to as a "green" part at this stage. The unbound, loose tungsten powder is removed once the green part is completed. The part is then heated in a furnace to sinter the tungsten powder together as well as cause the thermochemical decomposition of the organic material of the binding epoxy.

Although the exact composition of the binderjetted filters was not available from the manufacturer, an independent analysis (ALS Global Life, Tuscon, AZ) of the tungsten material indicated a density of 11.206 $\mathrm{g/cm^3}$, with a composition, by weight, of 2.19% carbon, 0.23% hydrogen, 0.08% nitrogen, 1.58% oxygen, and 95.92% tungsten (the composition used in the Monte Carlo modeling in Chapter 5). A photograph of the filter prototypes is included in Figure 6.2.

6.3 Frame chassis and variable-position ceiling alignment laser system

A mobile frame chassis was constructed with a variable-position ceiling alignment laser system to position the collimator and filters in the beam path of the UWMRRC orthovoltage

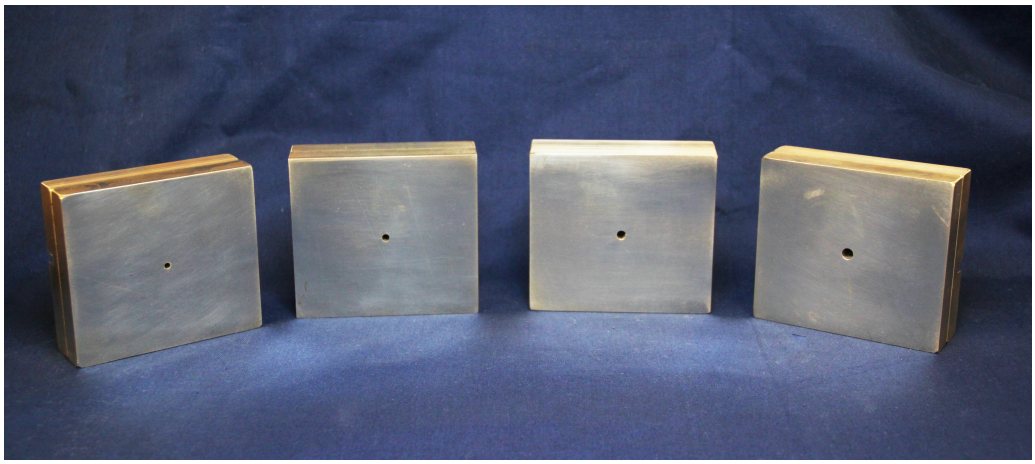

(a)

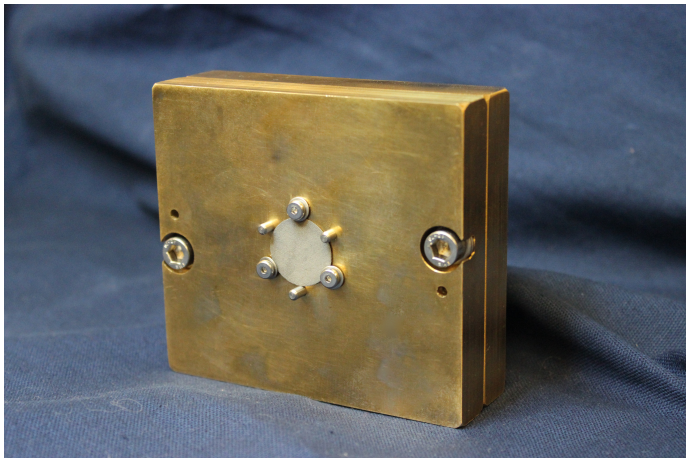

(b)

Figure 6.1: A photograph of the suite of four $(9 \times 10 \times 3.175)$ cm^3 nondivergent cone collimators. The collimators were constructed from high-leaded machining brass. Shown (a) from left to right are the 5, 6, 8, and 10 mm cones without filters in place, facing the surface to be placed proximally to the source. The 10 mm cone is shown (b) facing the surface to be placed distally to the source. Its tungsten filter is positioned in place using three dowel pins and fastened flush to the collimator surface using three small bolts.

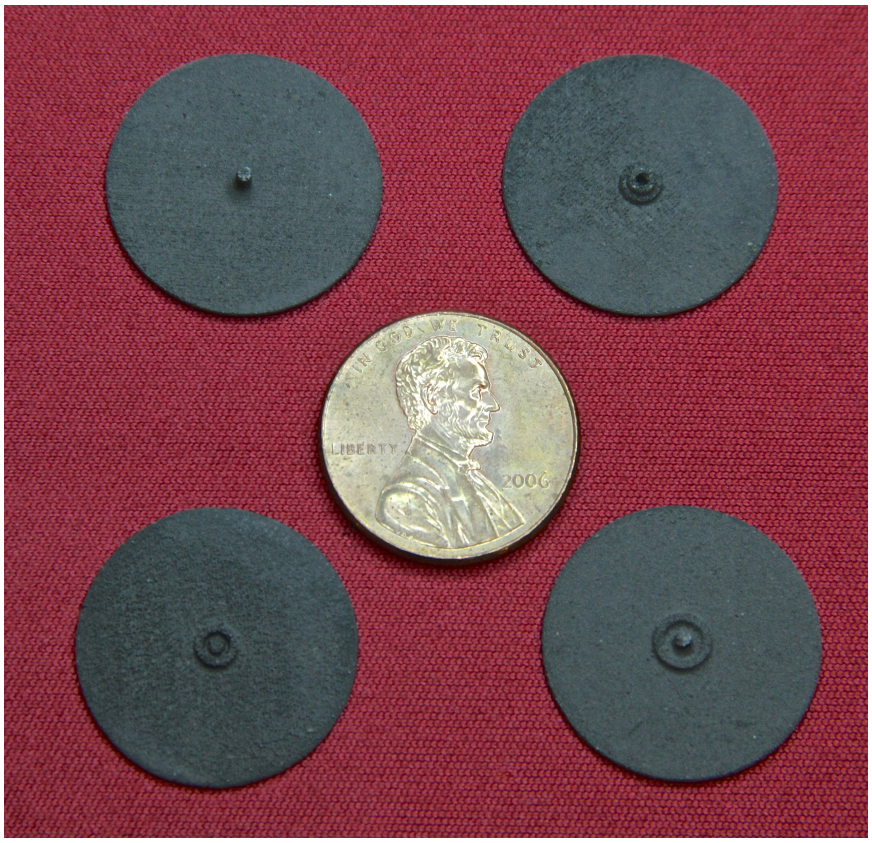

Figure 6.2: A photograph of the binderjetted epoxy-infiltrated bonded tungsten filter prototypes: 5 mm cone filter (upper left), 6 mm cone filter (upper right), 8 mm cone filter (lower left), and 10 mm cone filter (lower right).

unit. The frame chassis consists of an aluminum extrusion framing base that may be temporarily affixed to the UWMRRC orthovoltage tube stand housing, along with two precision stages: one with tip, tilt, and rotational adjustment, and one with three linear axes cross-roller adjustment, allowing for fine-tuning of collimator position with six degrees of freedom.

The frame chassis was used to position the collimator 62.5 cm from the focal spot (measured from the collimator plane farthest from the source). For a conceivable future isocentric irradiation geometry, this would allow 37.5 cm to isocenter, which is within the range of clinically available industry standards for human SRS treatment delivery (small animal irradiators often have much lower clearance). This clearance distance is deemed sufficient for

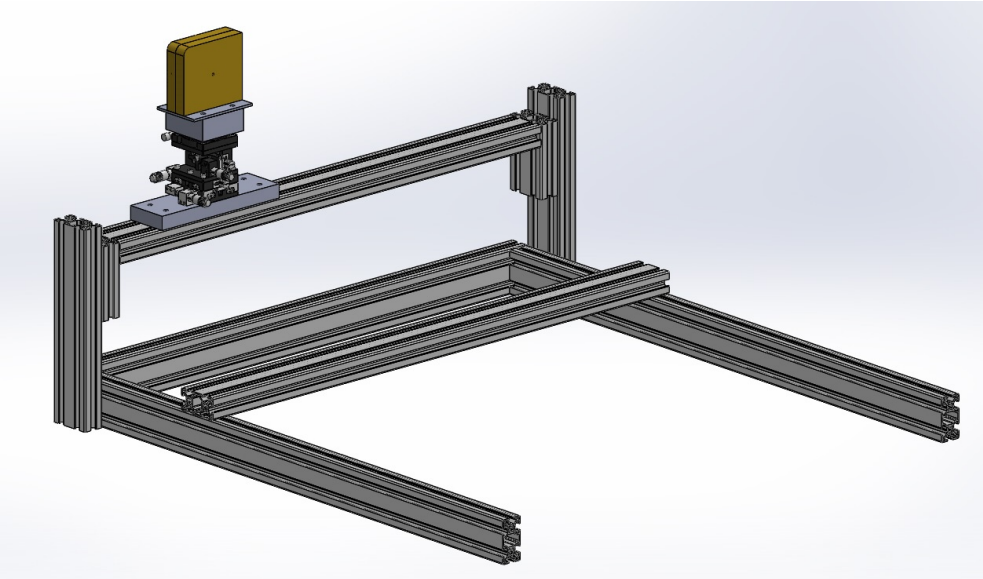

Figure 6.3: A CAD rendering of the mobile frame chassis for positioning the collimator and filter assembly in the UWMRRC orthovoltage beam path. The chassis consists of an aluminum extrusion framing base and precision stages that afford fine positioning adjustment with six degrees of freedom. The 5 mm collimator is included in the rendering.

avoiding geometric collisions with patients in most conceivable clinical treatments involving noncoplar-arc delivery. A CAD rendering of the frame chassis and one of the collimators is pictured in Figure 6.3. The frame chassis affixed to the UWMRRC orthovoltage tube stand housing is pictured in Figure 6.4.

A 45° fan angle, 532 nm, 4.5 mW fixed-focus green diode laser was acquired for alignment of equipment. The laser was factory focused to a distance of 1219 mm, which corresponds to the approximate distance between the beam path and the laser's mounted position. The laser was mounted on a rail-track system that allows for precision positioning using software designed in LabVIEW (National Instruments Corporation, Austin, TX). The laser and positioning system are pictured in Figure 6.5.

6.4 Radiochromic film irradiations

All radiochromic film irradiations were performed using $(4 \times 4)\,\mathrm{cm}^2$ film samples, which were placed individually in air-tight, vacuum-sealed packets as discussed in Section 3.3. Each film packet was positioned in the UWMRRC thin-window water phantom using a custom-built PMMA holder. The packet was suspended away from the holder edges using Kapton tape, as shown in Figure 6.6. A single film was used for each irradiation to avoid disturbance of the beam by films placed at multiple depths. Irradiations were completed using a 100 cm SAD geometry, at depths of 2.5, 5.0, and 7.5 cm. The positioning of the water phantom and the film within the phantom were determined using the variable-position ceiling alignment laser system, fixed-wall lasers, and the phantom plumb bobs. All films were irradiated to calculated central axis dose-to-water values that assured both the expected minimum and maximum dose values fell within the film calibration curve. These values were determined using the methods described in Section 3.6.2. Throughout the irradiation duration, the overhead vault lights were darkened to avoid any fogging effects of the film from ambient room light.

Irradiations were completed with filtered and unfiltered cone collimators positioned in the beam line using the mobile frame chassis, as well as open field irradiations with no collimator or chassis in place. For the collimated measurements, the positioning of the cone collimators was reviewed prior to every cone change, and adjusted using the fine positioning stages to assure correct positioning and leveling within the beam line.

6.5 Radiochromic film analysis

All film was scanned using the UWMRRC LDS and EPSON scanners following the film handling and scanning methods discussed in Sections 3.3 and 3.4. For pre-irradiation scanning, films were scanned first using the EPSON and then the LDS. For post-irradiation scanning, films were scanned first using the LDS and then the EPSON. This order was

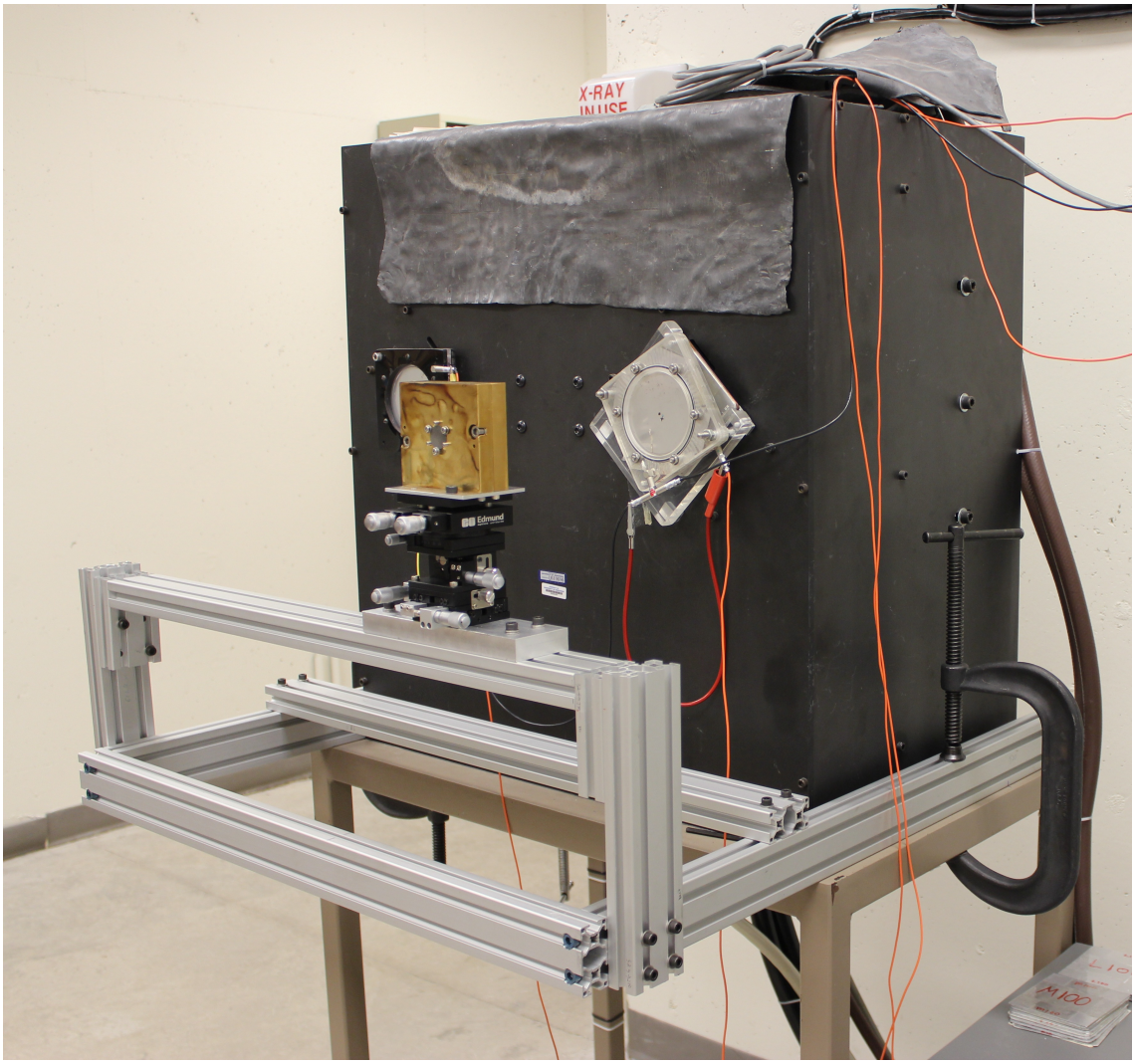

Figure 6.4: A photograph of the mobile frame chassis for positioning the collimator and filter assembly in the UWMRRC orthovoltage beam path. The aluminum extrusion framing base is temporarily clamped to the UWMRRC orthovoltage tube stand. The 6 mm collimator is positioned in the beam line, with its filter in place.

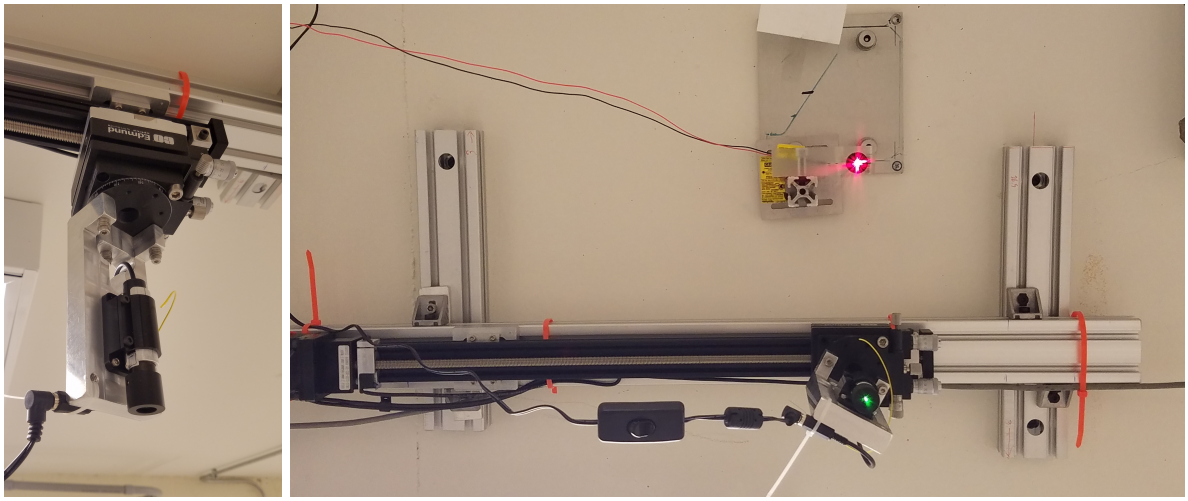

(a) (b)

Figure 6.5: A photograph of the translational ceiling laser system designed to meet the alignment needs of the UWMRRC orthovoltage energy-modulated SRS system. (a) A 45° fan angle, 532 nm, 4.5 mW fixed focus green diode laser was affixed to positioning stages for fine position adjustment. (b) A rail-track system allows for variable, precise positioning of the line laser with respect to the UWMRRC orthovoltage unit focal spot. Also shown is the stationary red laser alignment for positioning at 100 cm from the focal spot.

chosen in order to minimize the effect of film fogging due to exposure to the white light source of the EPSON. Prior to scanning, three fiducials were marked on each film to be used as fixed points of positioning reference, as shown in Figure 6.7. Raw image values were converted to dose-to-water values using the methods from Section 3.6. Samples of film images are included in Figures 6.8 and 6.9.

The requested fine feature specifications of the commissioned filter prototypes approached the limit of the manufacturing firm's commissioned manufacturing capabilities. Some initial filtered measurement results were poor, and it was discovered that the filter ring structures were composed of too much deposited tungsten (the rings were too wide in the plane perpendicular to the beam axis, and also too thick along the axis parallel to the beam axis) by up to 0.35 mm. A miniature needle file, a fine-tipped pointed metallic probe, and 80-grit aluminum-oxide sandpaper were used to shave and etch small amounts of tungsten from the

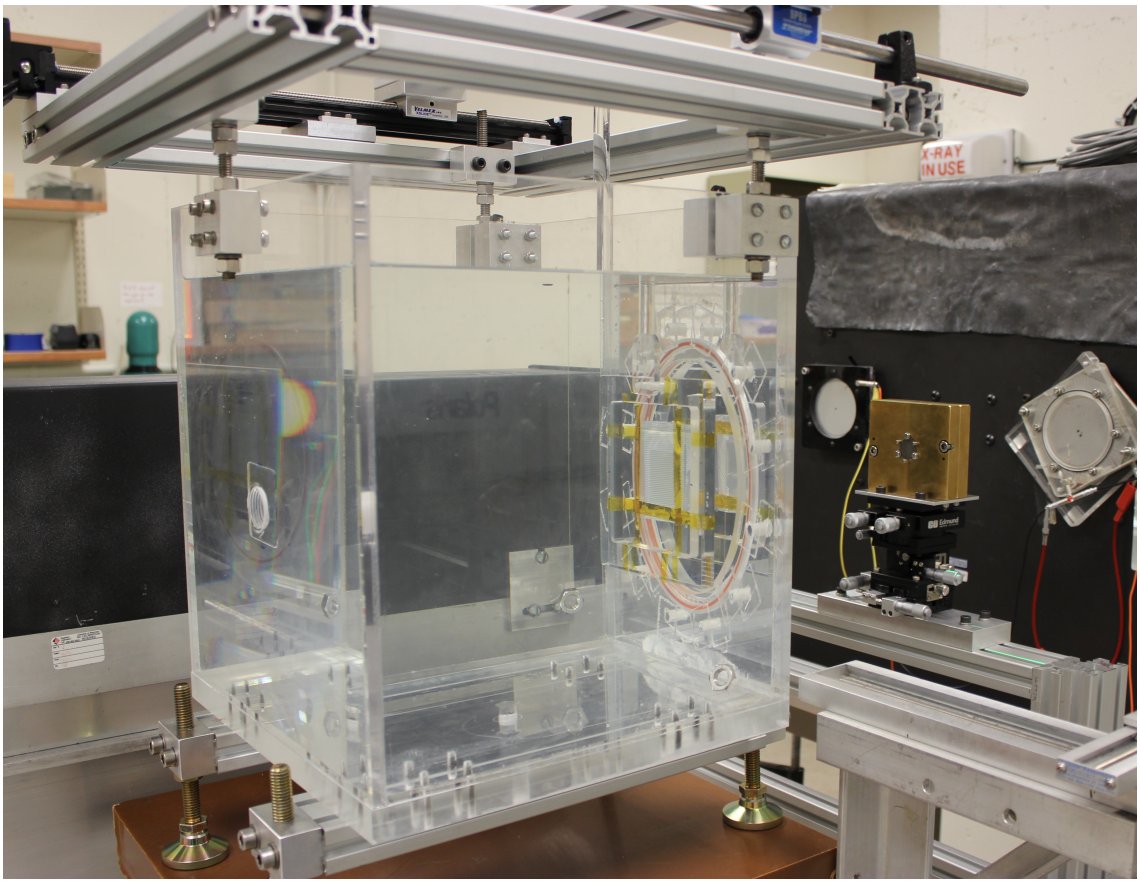

Figure 6.6: A photograph of the irradiation geometry for measurements of the filtered 10 mm collimator, with a $(4 \times 4)\,\mathrm{cm}^2$ film segment suspended in the UWMRRC thin-window water phantom at 2.5 cm depth and 100 cm SAD.

filters, iteratively removing attenuation material and then verifying filter dimensions using a micrometer and vernier calipers, until the filters reached design specifications. Small variations in filter feature thickness created during the manufacturing process (and subsequent in-house adjustment), as well as possible sub-millimeter misalignment during irradiation, may result in asymmetries in the final dose-to-water distributions measured on film.

6.5.1 Profile calculation

The post-irradiation film image processing was completed using ImageJ (U.S. National Institutes of Health, Bethesda, MD) and MATLAB software. Profiles were taken through

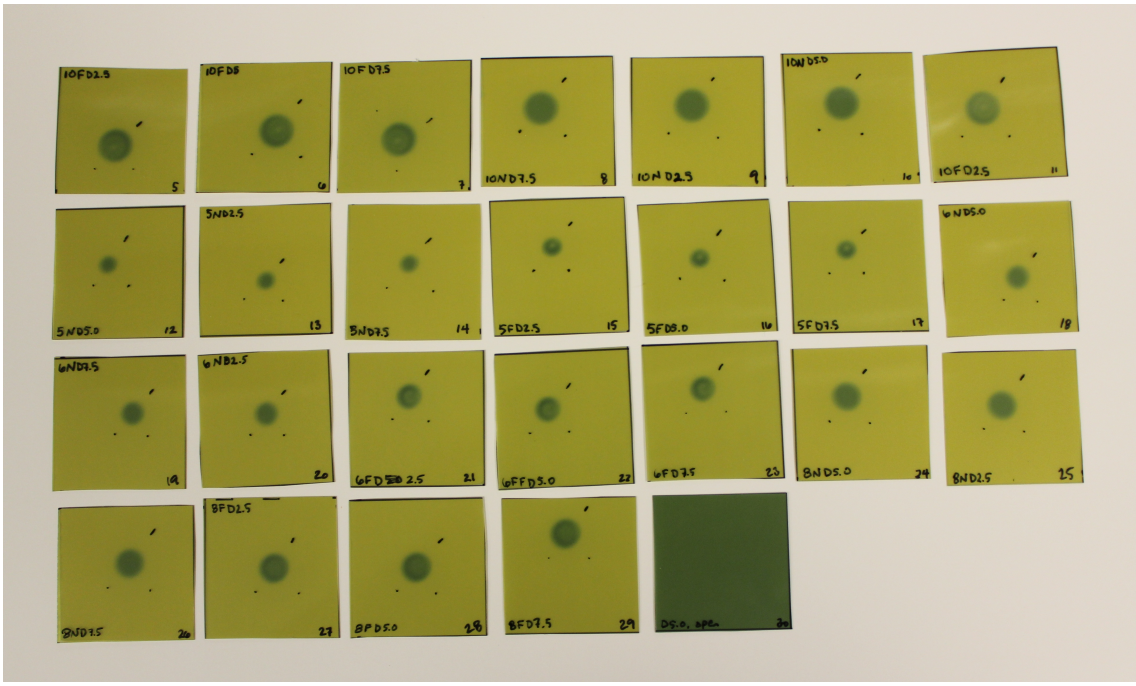

Figure 6.7: A photograph of one set of irradiated radiochromic films with marked fiducials.

the center of mass (centroid) of each array of dose values. To find the position of the centroid, small artifacts in the images due to specks of dust or scratches in the film were first processed out of the data with a threshold of 150% of the maximum expected dose value. An isodose value of 50% of the maximum dose was used to define the centroid. Linear dose profiles were extracted at 1,000 equally spaced angles about the centroid position. The average of these profiles was used to compute profile statistics. As discussed by Bender (2014), averaging over many profiles reduces the effect of noise in the analyzed image without requiring a separate smoothing image-processing step. Examples of profiles extracted from film data are included in Figure 6.10. It is noted that this profile extraction and averaging process results in symmetric profiles (as shown in Figure 6.10), though as discussed in the previous section, small variations in filter feature thicknesses as well as sub-millimeter misalignment during radiation may deliver asymmetric distributions (as shown in Figure 6.9). This difficulty may be avoided for possible future iterations of the prototype system as additive manufacturing technologies improve.

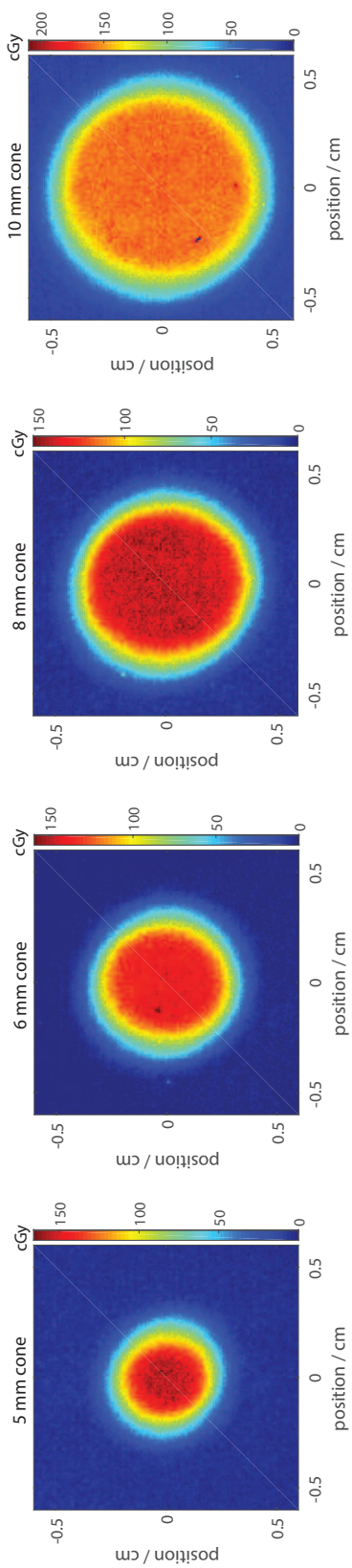

Figure 6.8: Example film images irradiated with open cones at 5 cm depth, acquired using the EPSON, and converted to dose-to-water values: (a) 5 mm cone, (b) 6 mm cone, (c) 8 mm cone, and (d) 10 mm cone.

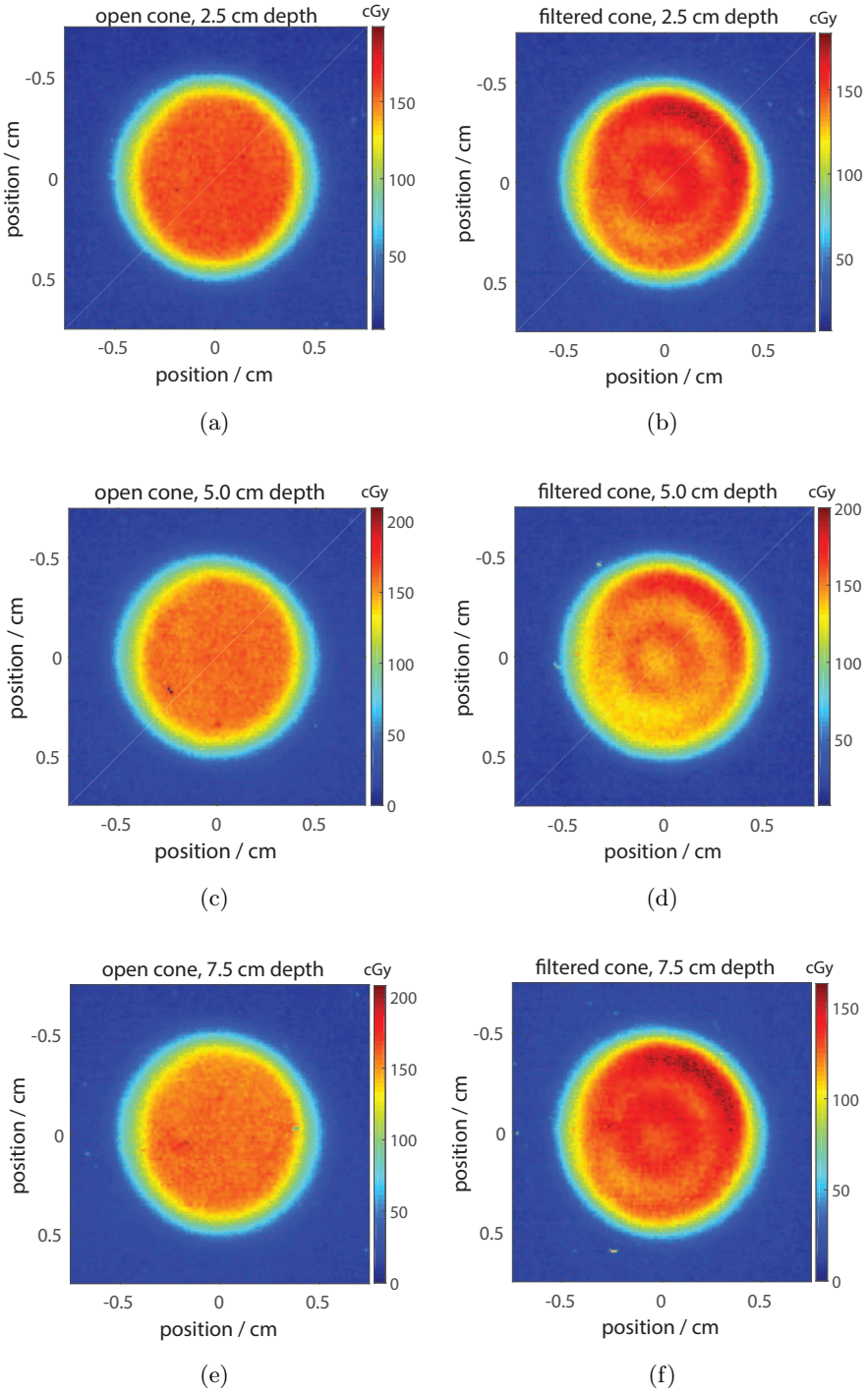

Figure 6.9: Example film images acquired using the EPSON and converted to dose-to-water values for the 10 mm cone. Standard, open cones (left) and filtered cones (right) are shown for depths of 2.5 cm [(a) and (b)], 5.0 cm [(c) and (d)], and 7.5 cm [(e) and (f)].

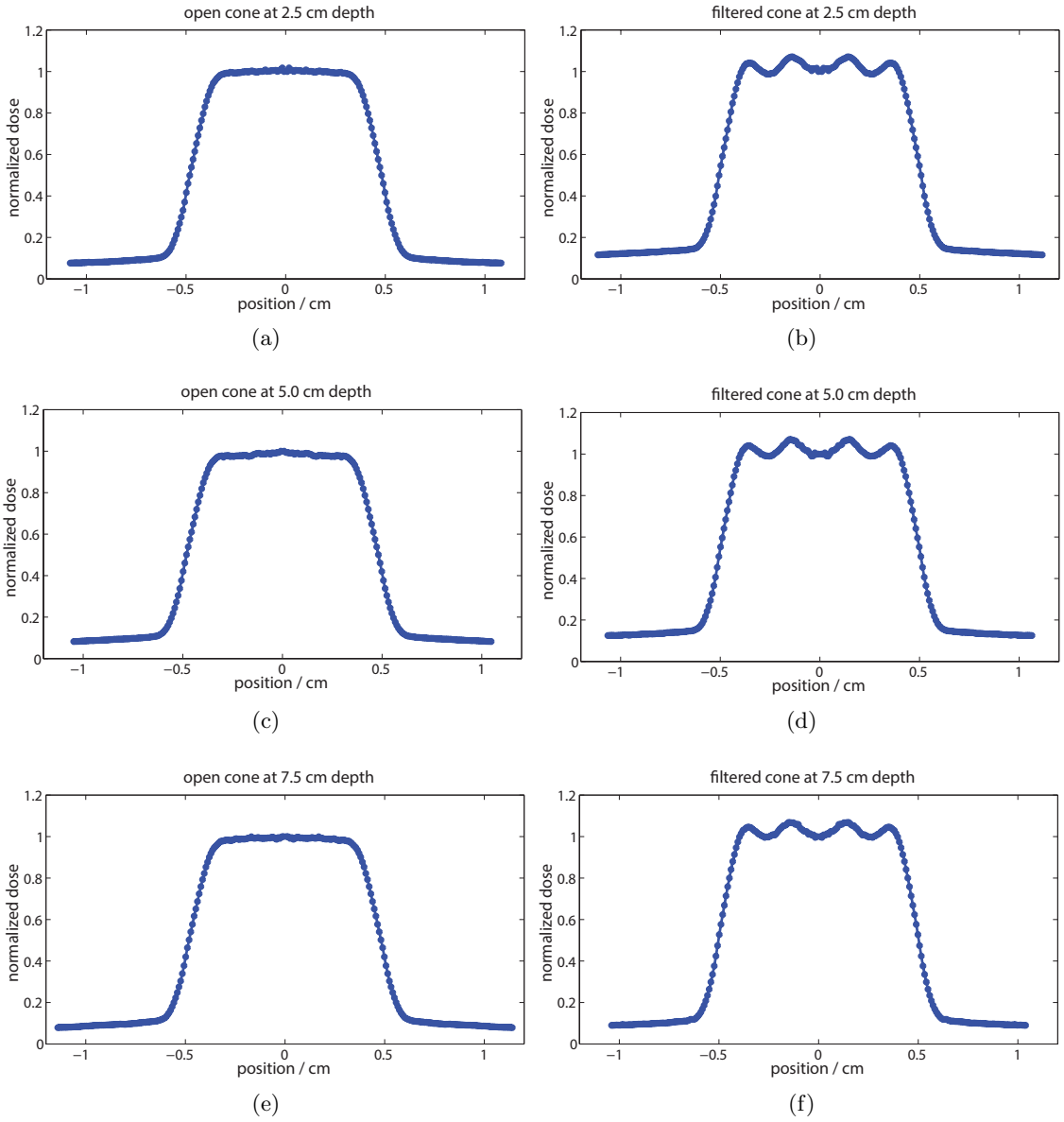

Figure 6.10: Example dose profiles from film images irradiated with the 10 mm cone, acquired using the EPSON. Standard, open cones (left) and filtered cones (right) are shown for 2.5 cm depth [(a) and (b)], 5.0 cm depth [(c) and (d)], and 7.5 cm depth [(e) and (f)].

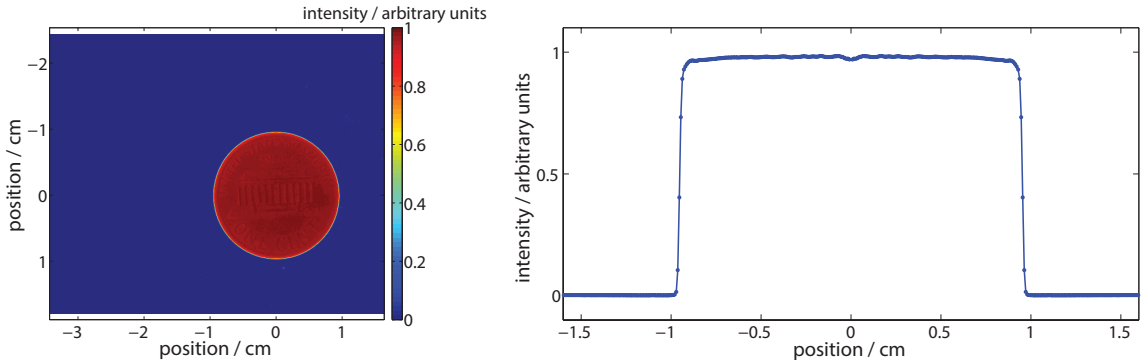

(a) (b)

Figure 6.11: Quality verification of average profile process using a penny. Shown in (a) is a zero-padded EPSON scan, and (b) the subsequent average profile of the scan.

The profile calculation process was tested by scanning a penny with both the LDS and the EPSON scanners to attain scanning data from an opaque, nearly circular object with dimensions accommodated by the ABS $(4 \times 4)\,\mathrm{cm}^2$ scanning frames. For the LDS scan, the penny was suspended using a thin layer of transparent plastic stretched over an ABS scanning frame cell, and for the EPSON scanner the penny was placed directly on the glass scan bed. The scanning data were zero padded to offset the high intensity regions from center, as shown in Figure 6.11. The automated profile process correctly identified the scan centroid position to within one pixel in both the horizontal and vertical directions, and also correctly identified (to within 0.005 mm) the nominal measured penny diameter, based on the profile FWHM.

6.5.2 Scanning resolution

The resolution involved with radiochromic film dosimetry is not determined exclusively by the film, but also by the scanning system and acquisition protocol (Bouchard et al., 2009; Asero et al., 2016; Butson et al., 2003; Soares, 2009; Niroomand-Rad et al., 1998; Rosen et al., 2015). Asero et al. (2016) used a mammography unit and a bar pattern to acquire film images with XR-QA2 radiochromic film. The film images were scanned on an EPSON

Perfection V750 Pro white light flatbed document scanner using a range of resolution acquisition parameters to find the effective resolution corresponding to the modulation transfer function (MTF) at 50%. They found that for their experimental set-up and a scanning setting of 300 dpi (corresponding to a nominal scan setting resolution of 85 μm), they achieved a much coarser resolution than the nominal value indicated by their chosen scanning parameters (measuring approximately 128 μm). They concluded that although commercial flatbed scanners may offer acquisition resolution options in the thousands of dpi, it is important to distinguish between geometrical resolution of real content and higher resolution values acquired through interpolation. Although a different model flatbed scanner was used in this work, this effect was observed through the finer pixelated patterns acquired using the LDS compared to the EPSON Expression 10000XL scanner. However, the practice of averaging over many profiles has the effect of smoothing the LDS profiles such that profiles acquired with either scanner appear qualitatively similar.

6.5.3 Profile analysis

For both LDS and EPSON data, profiles were analyzed for flatness and penumbra, using the methods discussed in Chapter 5. These results are summarized in Tables 6.1, 6.2, 6.3, and 6.4. The profile statistics were similar for data acquired using the EPSON and using the LDS and the measured penumbra and flatness values from both scanners showed the same directional trends when comparing the results between open and filtered profiles. Because the time required to collect scanning data for the LDS is significantly higher than for the EPSON (several hours for the LDS compared to minutes on the EPSON), and considering that most facilities do not have access to a prototype laser densitometry system similar to the LDS, this result suggests that film analysis using a high-quality, white-light flatbed scanner is adequate for this application. The filtered beams showed improved flatness and penumbra statistics compared to the unfiltered beam for all measurement configurations; however, for two specific measurements, this improvement fell within the uncertainty of the

Table 6.1: 80–20% penumbra statistics for LDS-measured beam profiles at 2.5, 5.0, and 7.5 cm depths. Films were suspended in the UWMRRC thin-window water phantom in a 100 cm SAD irradiation geometry. Measurements were completed for standard (open) cones, as well as for modulated cones with optimized filters in place. Uncertainty values represent the standard deviation of repeated measurements.

Cone size (mm)	depth (cm)	standard (mm)	modulated (mm)	percent improvement
5	2.5	1.11 ± 0.05	1.00 ± 0.03	11%
6	2.5	1.17 ± 0.06	0.962 ± 0.027	18%
8	2.5	1.15 ± 0.06	1.04 ± 0.02	10%
10	2.5	1.25 ± 0.07	1.06 ± 0.02	15%
5	5.0	1.13 ± 0.03	1.02 ± 0.06	9%
6	5.0	1.19 ± 0.04	0.966 ± 0.046	19%
8	5.0	1.17 ± 0.06	1.07 ± 0.04	9%
10	5.0	1.25 ± 0.06	1.13 ± 0.03	9%
5	7.5	1.15 ± 0.05	1.04 ± 0.03	10%
6	7.5	1.18 ± 0.03	1.01 ± 0.05	15%
8	7.5	1.21 ± 0.05	1.06 ± 0.07	12%
10	7.5	1.27 ± 0.03	1.17 ± 0.03	8%

measurements (the EPSON 80–20% penumbra measurement with the 10 mm cone at 5.0 cm depth, and the EPSON flatness measurement with the 10 mm cone at 2.5 cm depth).

From Figure 6.10 it is apparent that the slightly rippled profile shape will produce areas slight dose inhomogeneity inside the target volume. This would need to be taken into account in the prescription if such a system were to be used clinically.

The Monte Carlo results used to design the system (Chapter 5) were compared to example film profiles, included in in Figure 6.12. All profiles were normalized to the central axis dose value. There is excellent agreement between the measured and predicted profiles in the central and fall-off regions for the open cone measurements. The profile tails are slightly different and likely due to the selection of normalization point. The results for the filtered cones show similar shapes and tight agreement in the FWHM region, but show discrepancies in the more modulated peak areas. Differences between the modeled and measured beam

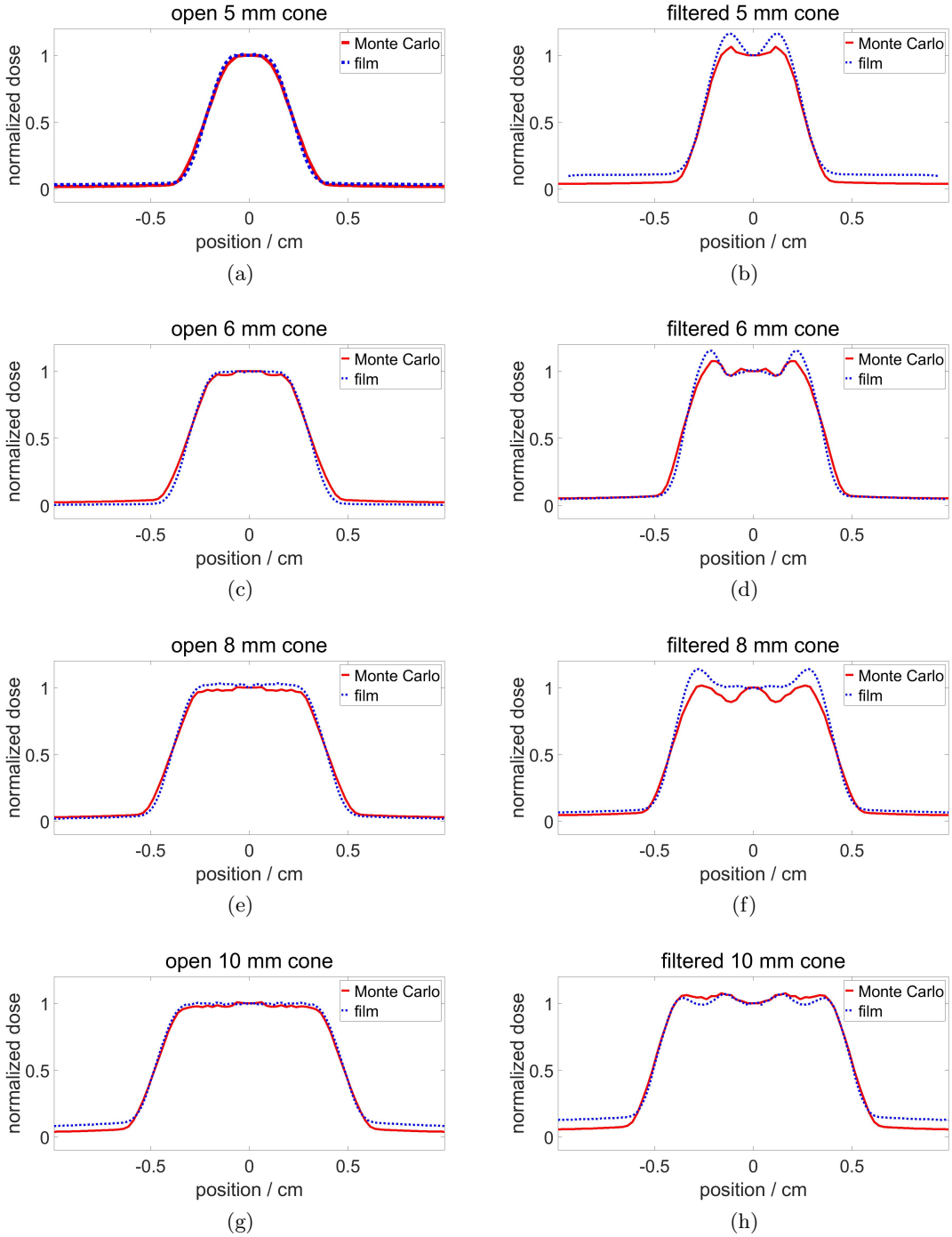

Figure 6.12: Monte Carlo-predicted profiles compared to example film dose profiles acquired using the EPSON for 5 cm depth. Standard, open cones (left) and filtered cones (right) are shown for the 5 mm cone [(a) and (b)], 6 mm cone [(c) and (d)], 8 mm cone [(e) and (f)] and 10 mm cone [(g) and (h)].

Table 6.2: Flatness statistics for LDS-measured beam profiles at 2.5, 5.0, and 7.5 cm depths. Films were suspended in the UWMRRC thin-window water phantom in a 100 cm SAD irradiation geometry. Measurements were completed for standard (open) cones, as well as for modulated cones with optimized filters in place. Uncertainty values represent the standard deviation of repeated measurements.

Cone size (mm)	depth (cm)	standard (%)	modulated (%)	percent improvement
5	2.5	16.8 ± 0.9	12.8 ± 0.4	24%
6	2.5	12.2 ± 0.6	7.77 ± 0.28	37%
8	2.5	8.65 ± 0.44	5.47 ± 0.28	37%
10	2.5	7.13 ± 0.50	4.33 ± 0.16	39%
5	5.0	16.4 ± 0.6	13.4 ± 0.6	18%
6	5.0	12.7 ± 0.7	7.65 ± 0.42	40%
8	5.0	8.38 ± 0.23	6.14 ± 0.25	27%
10	5.0	7.42 ± 0.42	5.09 ± 0.42	31%
5	7.5	16.6 ± 0.6	12.7 ± 0.3	23%
6	7.5	12.4 ± 0.4	7.98 ± 0.27	36%
8	7.5	10.4 ± 0.6	6.17 ± 0.36	40%
10	7.5	6.56 ± 0.48	4.57 ± 0.23	30%

profiles may be attributed to inconsistencies between modeled and measured conditions. These differences may be due to factors including inaccuracies in the initial BEAMnrc model of the UWMRRC orthovoltage unit, discrepancies between modeled filter composition and dimensions compared to their physical values, and misalignment of system components during measurement. Similar to previous work (Bender, 2014), the overall goal of this project was to lay the groundwork for establishing a clinical stand-alone system and not to demonstrate perfect agreement between measured and predicted profiles.

Table 6.3: 80–20% penumbra statistics for EPSON-measured beam profiles at 2.5, 5.0, and 7.5 cm depths. Films were suspended in the UWMRRC thin-window water phantom in a 100 cm SAD irradiation geometry. Measurements were completed for standard (open) cones, as well as for modulated cones with optimized filters in place. Uncertainty values represent the standard deviation of repeated measurements.

Cone size (mm)	depth (cm)	standard (mm)	modulated (mm)	percent improvement
5	2.5	1.23 ± 0.02	1.12 ± 0.05	9%
6	2.5	1.25 ± 0.04	1.08 ± 0.01	14%
8	2.5	1.26 ± 0.03	1.15 ± 0.04	9%
10	2.5	1.42 ± 0.07	1.31 ± 0.06	8%
5	5.0	1.26 ± 0.05	1.17 ± 0.04	7%
6	5.0	1.28 ± 0.05	1.04 ± 0.03	18%
8	5.0	1.30 ± 0.05	1.21 ± 0.04	6%
10	5.0	1.40 ± 0.06	1.36 ± 0.07	3%
5	7.5	1.26 ± 0.04	1.20 ± 0.02	5%
6	7.5	1.24 ± 0.06	1.09 ± 0.07	12%
8	7.5	1.30 ± 0.04	1.14 ± 0.06	13%
10	7.5	1.42 ± 0.07	1.32 ± 0.03	7%

Table 6.4: Flatness statistics for EPSON-measured beam profiles at 2.5, 5.0, and 7.5 cm depths. Films were suspended in the UWMRRC thin-window water phantom in a 100 cm SAD irradiation geometry. Measurements were completed for standard (open) cones, as well as for modulated cones with optimized filters in place. Uncertainty values represent the standard deviation of repeated measurements.

Cone size (mm)	depth (cm)	standard (%)	modulated (%)	percent improvement
5	2.5	16.3 ± 0.7	12.5 ± 0.2	23%
6	2.5	11.6 ± 0.4	7.93 ± 0.23	32%
8	2.5	8.20 ± 0.14	7.15 ± 0.21	13%
10	2.5	6.25 ± 0.40	5.79 ± 0.21	7%
5	5.0	16.4 ± 0.8	12.9 ± 0.2	22%
6	5.0	12.1 ± 0.7	8.90 ± 0.23	26%
8	5.0	8.39 ± 0.47	6.25 ± 0.42	26%
10	5.0	6.37 ± 0.26	4.12 ± 0.23	35%
5	7.5	16.5 ± 0.8	12.9 ± 0.2	22%
6	7.5	12.0 ± 0.7	8.51 ± 0.82	29%
8	7.5	8.52 ± 0.25	7.03 ± 0.53	17%
10	7.5	5.95 ± 0.44	4.20 ± 0.19	29%

Chapter 7

Conclusions

7.1 Conclusions

Optimization in the context of orthovoltage SRS has been explored. This was done first by investigating orthovoltage SRS systems in general, and then in the context of the UWMRRC orthovoltage unit specifically. A prototype system was designed using mathematical and Monte Carlo methods, and then constructed for dosimetry characterization using radiochromic film. Film measurements in a water phantom verified the ability to manipulate orthovoltage SRS distributions, in this case in order to achieve distributions approaching rectangular functions.

7.1.1 Orthovoltage Dose Gradient Index analyses

This work examined a trade-off between prescription isodose and dose gradients in orthovoltage SRS with dose distributions generated using point energy deposition kernels. These dose distributions were used to calculate dose profiles through a 4π isotropic delivery of circularly collimated beams. Monoenergetic beams and an orthovoltage polyenergetic spectrum were analyzed. The Dose Gradient Index was calculated as a function of prescription isodose for circular cones ranging from 4 to 18 mm in diameter and monoenergetic beams

with energies ranging from 20 to 250 keV. The relationship between DGI and prescription isodose was found to be dependent on both field size and energy, and prescription isodose values were found that optimize DGI.

7.1.2 System design with optimization and Monte Carlo methods

A methodology has been presented in this work that may be used to optimize the spatial distribution of added filtration material in an orthovoltage SRS beam to result in dose distributions with improved flatness and penumbrae compared to standard open cones. This thesis provides the mathematical foundation for a novel, orthovoltage modulated SRS system.

To achieve SRS dose distributions approaching rectangular functions using orthovoltage energy fluence modulation, inverse planning optimization techniques were used to determine patterns of spatially variant filtration material spaced within SRS cone collimator apertures. A pencil-beam model was used to calculated dose distributions based on the UWMRRC UW250-M beam. Kernels for the model were derived using Monte Carlo methods, and a Genetic Algorithm search heuristic was used to optimize the filtration pattern. Optimizations were performed for 5.0 cm depth, with cone sizes of 5, 6, 8, and 10 mm. In addition to the beam profiles, 4π isocentric irradiations of a 10 cm-radius sphere of water were modeled to examine dose at 0.07 mm, a representative skin depth, for the low energy beams. Dose to bone was also examined in a 4π isocentric irradiation geometry to calculate dose to a spherical bone shell of 7 mm thickness, a representative skull thickness, as function of dose to a central tissue region.

Based on the results of the optimization, circularly symmetric tungsten filters were designed to modulate the orthovoltage beam across the aperture of an SRS cone collimator. For each cone size at depths of 2.5, 5.0, and 7.5 cm, the beam flatness and 80–20% and 90–10% penumbrae were calculated for both standard, open cone-collimated beams as well as for the optimized, filtered beams. For all configurations tested, the modulated beams

were able to achieve improved penumbra widths and flatness statistics at depth. The dose at 0.07 mm depth in the 4π isocentric irradiation geometries was higher for the modulated beams compared to unmodulated beams; however, the modulated dose at 4π depth remained $<0.025\%$ of the central, maximum dose. For the 4π dose-to-bone simulations, the dose deposited in the bone was $<3.5\%$ of the dose deposited in the central tissue material.

An analysis of DGI was included for the standard, open cone-collimated beams as well as for the optimized, filtered beams. Again, an optimal value for prescription isodose was found for all configurations tested. For all cone sizes, the DGI for the modulated cones were less than that for the unmodulated cones for all prescription isodose values $>70\%$. Optimizing the choice of prescription would maximize the benefits of the specialized system, and a summary of the optimal values is tabulated in Chapter 5.

7.1.3 Prototype construction and characterization

Four cone collimators were custom built using Alloy 353 high-leaded machining brass. Cone sizes of 5, 6, 8, and 10 mm were machined, and were designed to either be used open or with an epoxy-infiltrated bonded tungsten filter in place. These filters were manufactured based on the design process described in Chapter 5 through an additive manufacturing process called binderjetting. Finally, an aluminum framing chassis offering six degrees of positioning freedom was built for use with a variable-position ceiling alignment laser system to position the collimator and filter assemblies within the UW250-M beam line.

Dosimetry measurements were performed using two different scanning systems and radiochromic film in a water phantom for both filtered and unfiltered cones at depths of 2.5, 5.0, and 7.5 cm. The LDS offered higher true spatial resolution; however, after averaging over many profiles, similar results were achieved using either scanner. Extracted beam profiles validated the ability to optimize dosimetric results based on desired dose distributions—for this work, the goal distributions were rectangular functions. In all cases, filtered, optimized

cones were able to achieve distributions more closely approaching rectangular functions compared to open cones, as determined by penumbra and flatness statistics.

7.2 University of Wisconsin physician perspective on a rectangular function dose distributions

Dr. Steven P. Howard, a radiation oncologist and professor of the Department of Human Oncology at the University of Wisconsin School of Medicine and Public Health, is an expert in SRS procedures, overseeing the majority of SRS cases treated at UW. When interviewed as part of this project (2017), he discussed a rectangular function dose distribution in an SRS context. He pointed out a theoretical benefit, notably when it comes to long term effects, of minimizing integral dose by shrinking the penumbra. He elaborated that such an effect could especially benefit younger patients, for whom the probability of secondary malignancies is an important consideration (mentioning that in the last year alone he treated three AVM cases in patients who were all under the age of nineteen, for whom rectangular function dose distributions would be especially desirable). And while he noted that he welcomes hot spots within metastatic target volumes, "for benign disease, I would go out of my way to have a homogeneous dose" to avoid possible complications.

7.3 Factors concerning future treatment platforms

7.3.1 Relative Biological Effectiveness

In addition to providing improved dose distributions, an orthovoltage energy-modulated system may also offer a benefit regarding relative biological effectiveness (RBE). RBE is defined as the ratio of the dose of a "standard" (or reference) radiation source required to achieve a given biological endpoint, to the dose of a test radiation required to achieve the same endpoint (ICRP Publication 92, 2003). 250 kVp x-rays and ^{60}Co have both been

proposed as the standard radiation against which to form comparisons. Various factors affect RBE, including radiation quality, number of fractions, dose rate, and type of cell or tissue irradiated (Hall and Giaccia, 2006; Podgorsak, 2005). Of interest for this project is the influence of beam quality, particularly linear energy transfer (LET), on RBE. The rate of energy absorption of an irradiated medium of unit density by a traversing electron, the LET, is approximately 0.2 keV µm^{-1} for ^{60}Co, 2.0 keV µm^{-1} for 250 kVp x-rays, 166 keV µm^{-1} for 2.5 MeV α-particles, and 1000 keV µm^{-1} for high-energy Fe ions (cosmic radiation) (Hall and Giaccia, 2006). A value of 100 keV µm^{-1} may maximize the RBE for endpoints such as cell killing, mutagenesis, or oncogenic transformation, due to the average separation between ionizing events on the order of the width of DNA (Barendsen, 1968; Prasad, 1995; Shrieve and Loeffler, 2009; Zeman, 2007). Treating with higher RBE does not offer a treatment benefit unless it improves the therapeutic ratio (the relationship between the probabilities for tumor control and for normal tissue damage). Because fractionated treatment regimes exploit the ability of healthy tissue to recover from sublethal damage, using a beam quality with increased RBE in a fractionated setting may negate some benefits of fractionation, as healthy tissues are less capable of repair between fractions (Nias, 1988, 1990; Tubiana and Wambersie, 1990). However, in a single-fraction environment (e.g., SRS) in which healthy tissues are not expected to repair prior to a subsequent fraction, an increase in RBE may be beneficial. Though the LET of the radiation used in this work is far from the optimized value of 100 keV µm^{-1}, decreasing the clinically standard 6 MV photon SRS energy to the orthovoltage range will result in a higher LET and RBE.

7.3.2 Design considerations

7.3.2.1 Geometric clearance

This work examined beam modulation in an orthovoltage energy range using a prototype device. Although direct clinical application is beyond the scope of this project, this project established the foundation for a feasible orthovoltage SRS system with potential applica-

tions to other areas of research and technological development. Calculations were completed with 37.5 cm clearance between the collimator distal face and isocenter for possible application to a clinical setting. For comparison, an Elekta linear accelerator equipped with a Standard MLC model offers a clearance distance of 35.3 cm, a Varian linear accelerator with a Millennium MLC-120 model offers a distance of 33.4 cm, and a Varian linear accelerator with a BrainLAB mMLC model offers a distance of 31 cm (Sharma et al., 2011; Tacke et al., 2008). Bortfeld et al. (1999) state that for intracranial targets, a clearance distance of 30 cm is sufficient even for large-angle non-coplanar beam orientations. The prototype clearance distance is within the range of industry standards, and is adequate clearance for non-coplanar arc plan delivery to avoid geometric collisions with a human patient. It is far more than adequate for the clearance demands of a small animal irradiator. Orthovoltage energies have been noted as the ideal energy range for small animal irradiators, (Verhaegen et al., 2011) and may be used effectively with radiosensitizers such as gold nanoparticles (Hainfeld et al., 2004; Rahman et al., 2009), suggesting possible applications aside from human patient SRS.

7.3.2.2 Future system image guidance

In general, orthovoltage x-ray tubes and collimation systems are relatively light for possible integration into a gantry-mounted platform for rotational delivery. Further, using orthovoltage energies assures that if an imaging component were added to the delivery platform, the imaging and treatment components may be delivered by a single x-ray tube. Such a dual-purpose x-ray tube represents a benefit in terms of cost as well as imaging-treatment system alignment.

7.3.2.3 Ideal orthovoltage unit specifications

Because the UWMRRC orthovoltage unit is maintained and NIST-matched only up to 250 kVp, the maximum beam energy available that could be actually used for measure-

ments was chosen for this work. This unit is used solely for research purposes and to complete NIST-traceable calibrations of therapy- and diagnostic-class ionization chambers; it is not intended to treat human subjects. However, traditional orthovoltage units designed specifically for treatment offer higher dose rates and can reach up to 500 kVp, and the early "supervoltage" units ranged from 600–1000 kVp (Almond and Orton, 2013; Hill et al., 2014; Medina et al., 2008). Gulmay, the manufacturer of the x-ray generator used in this work, offers commercially available generators with energies up to 450 kVp. A future system built from the foundation specifically for the treatment of human subjects would ideally include a high output, high orthovoltage energy, and small focal spot size x-ray tube and generator. The methods described in this work could be followed to optimize and characterize such a system.

7.3.3 Possible radiation-induced complications

7.3.3.1 Dose to skin

To avoid potential radiation-induced complications with a future modulated orthovoltage treatment platform, SRS treatment planning precautions that are standard with other SRS treatment platforms should be taken, including avoiding treatment plans that include beams traversing volumes of the brain that contain critical structures such as those controlling speech, motor functions, and senses (Ruzevick and Lim, 2013). Beyond the treatment planning safety considerations taken in conventional SRS treatment planning, skin dose is of special concern for an orthovoltage SRS system due to a lack of skin-sparing effect with low energies compared to customary SRS energies, as discussed in Chapter 5.

The skin is composed of epidermal and dermal layers, under which lies a layer of subcutaneous tissue, all of which may be damaged by radiation (Archambeau et al., 1995). Factors affecting skin reactions to radiation include radiation treatment characteristics, such as absorbed dose to skin, fractionation, radiation type, overall duration, and field size, as well as individual patient characteristics, such as anatomical site, other concurrent or previous

therapies, and individual susceptibility. These effects may be divided into acute (early) effects and late effects. Acute effects include erythema, pigmentation, dry (peeling) or moist (weeping) desquamation, and alopecia, and late effects include cosmetic changes as well as dyschromia, atrophy, edema, and ulceration (Banfi, 1988; Wagner and Casciato, 2004).

Studies of dose to skin from diagnostic imaging and interventional studies offer an indication of possible complications based on low-energy, single-fraction treatment, such as would be the case with the proposed modulated orthovoltage SRS treatment platform. Cutaneous radiation injury (CRI) refers to damage to the skin and underlying tissues due to acute exposure to external radiation (CDC, 2014). The lowest single-fraction threshold dose to induce CRI in interventional procedures—in this case, presenting as early transient erythema—is 2 Gy (Johnson et al., 2000; Kelsey et al., 2014; Wagner et al., 1994). Where skin dose is expected to be $\geq$3 Gy, recommendations from the International Commission on Radiological Protection (ICRP) and others indicate interventionists should record estimated skin dose and follow up with the patient 10 to 14 days and one month following the procedure (Cousins and Sharp, 2004; ICRP Publication 85, 2000; Jaco and Miller, 2010). Further, the U.S. Food and Drug Administration (FDA) recommends specifically monitoring skin dose for patients undergoing diagnostic radiology studies with the possibility of delivering 1 Gy (Hendee and Ritenour, 2002).

In Section 5.3.3, dose at 0.07 mm depth for a 10 cm-radius sphere of water irradiated in a 4π treatment geometry was tallied and found to be $\leq$ 0.025% of the central, isocentric dose with modulated orthovoltage cones. For a high-dose SRS target such as trigeminal neuralgia, a reasonable prescribed maximum dose is 75 Gy (Singh et al., 2016). For a lower-dose target such as vestibular schwannoma, a corresponding reasonable maximum dose is approximately 15 Gy (Puataweepong et al., 2014). 0.025% of the maximum doses for the high- and low-dose targets are 1.9 and 0.4 cGy, respectively. These values are far below the FDA recommended level of 1 Gy for patient skin dose monitoring; however, for extreme

irradiation geometries involving few incident beam angles or arcs, it is recommended that skin dose be carefully quantified and evaluated prior to treatment.

7.3.3.2 Dose to bone

As determined by O'Malley et al. (2006), a higher energy beam than the one used in this work would be ideal for intermediate-energy SRS; however, the 250 kVp beam with a relatively large focal spot size (nominally 5.5 mm) was chosen for this work because of its availability. In this energy range, the strong contribution of the photoelectric cross section results in a high dependence on atomic number. In heterogeneous media including bone, absorption of kilovoltage x-rays will be affected by the high-density material as well as by the presence of calcium. Due to the structure of bone and distribution of calcium, as discussed by Wagner et al. (1994), this dose is expected to be highly heterogeneous based on the matrix of calcium hydroxyapatite, osteocytes, endosteal cells, marrow, Haversian canals, and vessels.

Dose-to-bone values were quantified in the prototype system, and the results of O'Malley et al. regarding the effect of bone were confirmed in similar simulations, and a 4π treatment geometry of a 10 cm-radius sphere of tissue material with a 7 mm-thick spherical bone shell found a ratio of dose deposited in bone to dose deposited at the central, isocentric volume to be $\leq 3.5\%$. If an orthovoltage system is designed using the methods described here and used to treat a volume including bone, it is important that any high-dose regions be quantified. Preferably this dosimetry calculation would be completed using a treatment planning system designed to calculate dose to heterogeneous media.

7.4 Recommendations for future work

This research produced a working prototype to establish the foundation of a potential future full treatment platform. Other work completed with the University of Wisconsin Medical Physics Department has developed a convolution-superposition-based small animal

micro-RT orthovoltage treatment planning system for use with a custom irradiator with integrated imaging and radiotherapy capabilities (Prajapati, 2015; Prajapati et al., 2014) using the EDKs calculated for this work. Future directions for the modulated orthovoltage stereotactic radiosurgery system could include the construction of a gantry-mounted delivery system with a high orthovoltage energy, small focal spot, and high output x-ray tube and generator, for either human patient or small animal irradiations, as well as the development of a new, complementary treatment planning system (or adaption of an existing treatment planning system) for use with modulated orthovoltage stereotactic radiosurgery.

7.5 Closing remarks

As discussed in Chapter 1, previous work has shown immense potential for the use of both modulation and orthovoltage energies for SRS treatment delivery. This work examined multiple ways to achieve desired dose distributions, specifically rectangular function distributions, in SRS within this energy range. A novel, modulated orthovoltage SRS system was designed using mathematical optimization techniques and Monte Carlo modeling. These designs were used to construct working prototype cone collimator and filter assemblies that were then used to perform measurements of dose distributions in water with radiochromic film. Both the computational and measurement results showed that the prototypes were able to achieve dose distributions approaching rectangular function distributions at depth, therefore establishing the feasibility and efficacy of a full future treatment platform that relies on fluence modulation in the orthovoltage energy range to shape resulting dose distributions.

Bibliography

AAPM, 2004. Profile of radiation oncology departments. Professional survey, American Association of Physicists in Medicine, College Park, MD.

Abt Associates, 2015. The Abt study of medical physicist work values for radiation oncology physics services: Round IV. Professional survey, American Association of Physicists in Medicine, Bethesda, MD.

Adler, Jr., J. R., Gibbs, I. C., Puataweepong, P., Chang, S., 2006. Visual field preservation after multisession CyberKnife radiosurgery for perioptic lesions. Neurosurgery 59 (2), 244–254.

Ahnesjö, A., Aspradakis, M. M., 1999. Dose calculations for external photon beams in radiotherapy. Phys. Med. Biol. 44, R99–R155.

Ahnesjö, A., Saxner, M., Trepp, A., 1992. A pencil beam model for photon dose calculation. Med. Phys. 19 (2), 263–273.

Akbas, U., Kesen, N. D., Koksal, C., Bilge, H., 2016. Surface and buildup region dose measurements with Markus parallel-plate ionization chamber, GafChromic EBT3 film, and MOSFET detector for high-energy photon beams. Adv. High Energy Phys. 5, 1–10.

Alaei, P., Gerbi, B. J., Geise, R. A., 1999. Generation and use of photon energy deposition kernels for diagnostic quality x-rays. Med. Phys. 26 (8), 1687–1697.

Aldelaijan, S., Devic, S., Mohammed, H., Tomic, H., Liang, L., Deblois, F., Seuntjens, J., 2010. Evaluation of EBT-2 model GAFCHROMIC™ film performance in water. Med. Phys. 37 (7), 3687–3693.

Alexander, III, E., Loeffler, J. S., 1998. Textbook of Stereotactic and Functional Neurosurgery. McGraw-Hill, Inc., New York, NY, Ch. Clinical experience with linac radiosurgery, pp. 745–756.

Alexander, III, E., Loeffler, J. S., 1999. The case for radiosurgery. Clin. Neurosurg. 45, 32–40.

Allen, Jr., M. B., Doetsch, G. S., Gindin, R. A., Haar, F. L., Yaghmai, F., 1978. A Manual for Neurosurgery. University Park Press, Baltimore, MD.

Almond, P., Orton, C. G., 2013. History symposium: Early developments in teletherapy machines. (abstract) Med. Phys. 40 (6), 499.

Andrés, C., del Castillo, A., Tortosa, R., Alonso, D., Barquero, R., 2010. A comprehensive study of the GafChromic EBT2 radiochromic film. A comparison with EBT. Med. Phys. 37 (12), 6271–6278.

Andrews, D. W., Corn, B. W., Buchheit, W. A., 1998. Textbook of Stereotactic and Functional Neurosurgery. McGraw-Hill, Inc., New York, NY, Ch. Focused and conventional radiation treatments for acoustic neurinomas, pp. 823–833.

Andrews, D. W., Scott, C. B., Sperduto, P. W., Flanders, A. E., Gaspar, L. E., Schell, M. C., Werner-Wasik, M., Demas, W., Ryu, J., Bahary, J.-P., Souhami, L., Rotman, M., Mehta, M. P., Curran, Jr., W. J., 2004. Whole brain radiation therapy with or without stereotactic radiosurgery boost for patients with one to three brain metastases: Phase III results of the RTOG 9508 randomised trial. Lancet 363 (9422), 1665–1672.

Andrews, D. W., Suarez, O., Goldman, H. W., Downes, M. B., Bednarz, G., Corn, B. W., Werner-Wasik, M., Rosenstock, J., Curran, Jr., W. J., 2001. Stereotactic radiosurgery

and fractionated stereotactic radiotherapy for the treatment of acoustic schwannomas: comparative observations of 125 patients treated at one institution. Int. J. Radiat. Oncol. Biol. Phys. 50 (5), 1265–1278.

Anton, M., Büermann, L., 2015. Relative response of the alanine dosimeter to medium energy x-rays. Phys. Med. Biol. 60 (15), 6113–6129.

Antypas, C., Floros, I., Rouchota, M., Armpilia, C., Lyra, M., 2015. MLC positional accuracy evaluation through the picket fence test on EBT2 films and a 3D volumetric phantom. J. Appl. Clin. Med. Phys. 16 (2), 189–197.

Archambeau, J. O., Pezner, R., Wasserman, T., 1995. Pathophysiology of irradiated skin and breast. Int. J. Radiat. Oncol. Biol. Phys. 31 (5), 1171–1185.

Arfken, G., 1970. Mathematical Methods for Physicists, 2nd Edition. Academic Press, Inc., New York, NY, Ch. Determinants, matrices, and group theory, pp. 156–236.

Asero, G., Greco, C., Gueli, A. M., Raffaele, L., Spampinato, S., 2016. Evaluation of spatial resolution in image acquisition by optical flatbed scanners for radiochromic film dosimetry. J. Instrum. 11 (3), P03024.

Asgharizadeh, S., Bekera, H., Syme, A., Aldelaijan, S., DeBlois, F., Vuong, T., Evans, M., Seuntjens, J., Devic, S., 2015. Radiochromic film-based quality assurance for CT-based high-dose-rate brachytherapy. Brachytherapy 14 (4), 578–585.

Attix, F. H., 1986. Introduction to Radiological Physics and Radiation Dosimetry. John Wiley & Sons, Inc., New York, NY.

Azorín, J. F. P., García, L. I. R., Martí-Climent, J. M., 2014. A method for multichannel dosimetry with EBT3 radiochromic films. Med. Phys. 41 (6), 062101–1–062101–10.

Badakhshi, H., 2016. Image-Guided Stereotactic Radiosurgery. Springer International Publishing, Berlin, Germany.

Balagamwala, E. H., Suh, J. H., Barnett, G. H., Khan, M. K., Neyman, G., Cai, R. S., Vogelbaum, M. A., Novak, E., Chao, S. T., 2012. The importance of the conformal, heterogeneity, and gradient indices in evaluating Gamma Knife radiosurgery treatment plans for intracranial meningiomas. Int. J. Radiat. Oncol. Biol. Phys. 83 (5), 1406–1413.

Banfi, A., 1988. Handbook of Medical Oncology, 3rd Edition. Year Book Medical Publishers, Inc., Chicago, IL, Ch. Radiation-induced complications, pp. 955–962.

Barbaro, N. M., Quigg, M., Broshek, D. K., Ward, M. M., Lamborn, K. R., Laxer, K. D., Larson, D. A., Dillon, W., Verhey, L., Garcia, P., Steiner, L., Heck, C., Kondziolka, D., Beach, R., Olivero, W., Witt, T. C., Salanova, V., Goodman, R., 2009. A multicenter, prospective pilot study of Gamma Knife radiosurgery for mesial temporal lobe epilepsy: seizure response, adverse events, and verbal memory. Ann. Neurol. 65 (2), 167–175.

Barcia, J. A., Barcia-Salorio, J. L., López-Gómez, L., Hernández, G., 1994. Stereotactic radiosurgery may be effective in the treatment of idiopathic epilepsy: report on the methods and results in a series of eleven cases. Stereotact. Funct. Neurosurg. 63, 271–279.

Barcia-Salorio, J. L., Barcia, J. A., Hernández, G., López-Gómez, L., 1994. Radiosurgery of epilepsy. Long-term results. Acta Neuochir. Suppl. 62, 111–113.

Barcia-Salorio, J. L., Barcia, J. A., Roldán, P., Hernández, G., López-Gómez, L., 1993. Radiosurgery of epilepsy. Acta Neuochir. Suppl. 58, 195–197.

Barcia-Salorio, J. L., Roldán, P., Hernández, G., López-Gómez, L., 1985. Radiosurgical treatment of epilepsy. Appl. Neurophysiol. 48, 400–403.

Barendsen, G., 1968. Responses of cultured cells, tumours, and normal tissues to radiations of different linear energy transfer. Radiat. Res. Quart. 4, 293–356.

Barnett, G. H., Linskey, M. E., Adler, J. R., Cozzens, J. W., Friedman, W. A., Heilbrun, M. P., Lunsford, L. D., Schulder, M., Sloan, A. E., 2007. Stereotactic radiosurgery—an organized neurosurgery-sanctioned definition. J. Neurosurg. 106 (1), 1–5.

Bekerat, H., Devic, S., DeBlois, F., Singh, K., Sarfehnia, A., Seuntjens, J., Shih, S., Yu, X., Lewis, D., 2014. Improving the energy response of external beam therapy (EBT) GafChromic™ dosimetry films at low energies (≤100 keV). Med. Phys. 41 (2), 022101–1–022101–14.

Bender, E. T., 2014. Increasing dose gradient and uniformity in small fields using modulation: theory and prototypes for cone-based stereotactic radiosurgery. Med. Phys. 41 (5), 051706–1–051706–7.

Benedict, S. H., Yenice, K. M., Followill, D., Galvin, J. M., Hinson, W., Kavanagh, B., Keall, P., Lovelock, M., Meeks, S., Papiez, L., Purdie, T., Sadagopan, R., Schell, M. C., Salter, B., Schlesinger, D. J., Shiu, A. S., Solberg, T., Song, D. Y., Stieber, V., Timmerman, R., Tomé, W. A., Verellen, D., Want, L., Yin, F.-F., 2010. Stereotactic body radiation therapy: The report of AAPM Task Group 101. Med. Phys. 37 (8), 4078–4101.

Berg, A. T., Berkovic, S. F., Brodie, M. J., Buchhalter, J., Cross, J. H., van Emde Boas, W., Engel, J., French, J., Glauser, T. A., Mathern, G. W., Moshe, S. L., Nordli, D., Plouin, P., Scheffer, I. E., 2010. Revised terminology and concepts for organization of seizures and epilepsies: Report of the ILAE Commission on Classification and Terminology, 2005–2009. Epilepsia 51 (4), 676–685.

Berger, M. J., 1963. Monte Carlo calculation of the penetration and diffusion of fast charged particles. Meth. Comput. Phys. 1, 135–215.

Berger, M. J., Coursey, J. S., Zucker, M. A., Chang, J., 2005. ESTAR, PSTAR, and ASTAR: Computer programs for calculating stopping-power and range tables for electrons, protons, and helium atoms (version 1.2.3). Tech. rep., National Institute of Standards and Technology, Gaithersburg, MD, available: http://physics.nist.gov/star (last accessed November 4, 2016).

Berger, M. J., Hubbell, J. H., Seltzer, S. M., Chang, J., Coursey, J. S., Sukumar, R., Zucker, D. S., 2010. XCOM: Photon Cross Section Database (Version 1.5). Tech. rep., National Institute of Standards and Technology, Gaithersburg, MD, Gaithersburg, MD, available: http://physics.nist.gov/xcom (last accessed November 4, 2016).

Bernier, J., Hall, E. J., Giaccia, A., 2004. Radiation oncology: a century of achievements. Nat. Rev. Cancer 4 (9), 737–747.

Bhatnagar, J. P., Novotny, Jr., J., Niranjan, A., Kondziolka, D., Flickinger, J., Lunsford, D., Huq, M. S., 2009. First year experience with newly developed Leksell Gamma Knife® Perfexion™. J. Med. Phys. 34 (3), 141–148.

Bijl, H. P., van Luijk, P., Coppes, R. P., Schippers, J. M., Konings, A. W. T., van der Kogel, A. J., 2002. Dose-volume effects in the rat cervical spinal cord after proton irradation. Int. J. Radiat. Oncol. Biol. Phys. 52 (1), 205–211.

Biswas, T., Sandhu, A. P., Singh, D. P., Schell, M. C., Maciunas, R. J., Bakos, R. S., Muhs, A. G., Okunieff, P., 2003. Low-dose radiosurgery for benign intracranial lesions. Am. J. Clin. Oncol. 26 (4), 325–331.

Bonadonna, G., Buraggi, G. L., 1988. Handbook of Medical Oncology, 3rd Edition. Year Book Medical Publishers, Inc., Chicago, IL, Ch. Cancer of the endocrine system, pp. 873–858.

Borca, V. C., Pasquino, M., Russo, G., Grosso, P., Cante, D., Sciacero, P., Girelli, G., Porta, M. R. L., Tofani, S., 2013. Dosimetric characterization and use of GAFCHROMIC EBT3 film for IMRT dose verification. J. Appl. Clin. Med. Phys. 14 (2), 158–171.

Bortfeld, T., Schlegel, W., Höover, K.-H., Schultz-Ertner, D., 1999. Mini and micro multileaf collimators. Presented at the 41st Annual Meeting of the AAPM.
URL `https://www.aapm.org/meetings/99AM/pdf/2796-50260.pdf`

Bouchard, H., Frédéric Lacroix, Gilles Beaudoin, J.-F. C., Kawrakow, I., 2009. On the characterization and uncertainty analysis of radiochromic film dosimetry. Med. Phys. 36 (6), 1931–1946.

Brady, S., Yoshizumi, T., Toncheva, G., Frush, D., 2010. Implementation of radiochromic film dosimetry protocol for volumetric dose assessments to various organs during diagnostic CT procedures. Med. Phys. 37 (9), 4782–4792.

Brady, S. L., Toncheva, G., Dewhirst, M. W., Yoshizumi, T. T., 2009. Characterization of a ^{137}Cs irradiator from a new perspective with modern dosimetric tools. Health Phys. 97 (3), 195–205.

Brown, P. D., Roberge, D., Ballman, K., Laack, N., Giannini, C., Farace, E., Ashman, J., Khuntia, D., Cerhan, J., Parney, I., Urbanic, J., Gaspar, L. E., Barker, F., Hadjipanayis, C. G., 2014. Phase III trial of post-surgical stereotactic radiosurgery (SRS) compared with whole brain radiotherapy (WBRT) for resected metastatic brain disease. RTOG Protocol 1270. Tech. rep., Radiation Therapy Oncology Group of the American College of Radiology and North Central Cancer Treatment Group.

Brown, T. A. D., Hogstrom, K. R., Alvarez, D., Matthews, II, K. L., Ham, K., Dugas, J. P., 2012. Dose-response curve of EBT, EBT2, and EBT3 radiochromic films to synchrotron-produced monochromatic x-ray beams. Med. Phys. 39 (12), 7412–7417.

Butson, E. T., Cheung, T., Yu, P. K. N., Butson, M. J., 2010a. Measuring solar UV radiation with EBT radiochromic film. Phys. Med. Biol. 55 (20), N487–N493.

Butson, M. J., Cheung, T., Yu, P., 2008. Measuring energy response for RTQA radiochromic film to improve quality assurance procedures. Australas. Phys. Eng. Sci. Med. 31 (3), 203–206.

Butson, M. J., Cheung, T., Yu, P. K. N., Abbati, D., Greenoak, G. E., 2000. Ultraviolet radiation dosimetry with radiochromic film. Phys. Med. Biol. 45 (7), 1863–1868.

Butson, M. J., Cheung, T., Yu, P. K. N., Alnawaf, H., 2009. Dose and absorption spectra response of EBT2 Gafchromic film to high energy x-rays. Australas. Phys. Eng. Sci. Med. 32 (4), 196–202.

Butson, M. J., Mathur, J. N., Metcalfe, P. E., 1996. Radiochromic film as a radiotherapy surface-dose detector. Phys. Med. Biol. 41 (6), 1073–1075.

Butson, M. J., Yu, P. K., Cheung, T., Alnawaf, H., 2010b. Energy response of the new EBT2 radiochromic film to x-ray radiation. Radiat. Meas. 45 (7), 836–839.

Butson, M. J., Yu, P. K., Cheung, T., Metcalfe, P., 2003. Radiochromic film for medical radiation dosimetry. Mat. Sci. Eng. R. 41 (3-5), 61–120.

Butson, M. J., Yu, P. K. N., Metcalfe, P. E., 1998. Effects of read-out light sources and ambient light on radiochromic film. Phys. Med. Biol. 43 (8), 2407–2412.

Butson, M. J., Yu, P. K. N., Metcalfe, P. E., 1999. Extrapolated surface dose measurements with radiochromic film. Med. Phys. 26 (3), 485–488.

Calzavara, F., Piazza, G., Pozza, F., 1966. Aspetti fisici e radiobiologici della penombra in radioterapia. Minerva. Radiol. Fisioter. Radiobiol. 11 (10), 529–532.

Cameron, J. R., 1967. A survey of solid state dosimetry. In: Amelinckx, S., Batz, B., Strumane, R. (Eds.), Solid State Dosimetry. NATO Summer School, Gordon and Breach Science Publishers, Inc., Brussels, Belgium, pp. 695–721.

Carrasco, M., Perucha, M., Luis, F., Baeza, M., Herrador, M., 2013. A comparison between radiochromic EBT2 film model and its predecessor EBT film model. Phys. Med. 29 (4), 412–422.

CDC, 2014. Cutaneous radiation injury (CRI): A fact sheet for clinicians. Tech. rep., Centers for Disease Control and Prevention, U.S. Department of Health and Human Services, Atlanta, GA.

Chan, A. W., Cardinale, R. M., Loeffler, J. S., 2004. Stereotactic Irradiation, 4th Edition. Lippincott Williams & Wilkins, Philadelphia, PA, Ch. Principles and Practice of Radiation Oncology, pp. 410–427.

Chang, S., Adler, J. R., 1997. Treatment of cranial base meningiomas with linear accelerator radiosurgery. Neurosurgery 41 (5), 1019–1027.

Chang, S. D., Gibbs, I. C., Sakamoto, G. T., Lee, E., Oyelese, A., Adler, Jr., J. R., 2005. Staged stereotactic irradiation for acoustic neuroma. Neurosurgery 56 (6), 1254–1261.

Chen, F., Gupta, R., Metcalfe, P., 2010. Intensity modulated radiation therapy (IMRT) surface dose measurements using a PTW Advanced Markus chamber. Australas. Phys. Eng. Sci. Med. 33 (33), 23–34.

Chetty, I. J., Curran, B., Cygler, J. E., DeMarco, J. J., Ezzell, G., Faddegon, B. A., Kawrakow, I., Keall, P. J., Liu, H., Ma, C.-M. C., Rogers, D. W. O., Seuntjens, J., Sheikh-Bagheri, D., Siebers, J. V., 2007. Report of the AAPM Task Group No. 105: Issues associated with clinical implementation of Monte Carlo-based photon and electron external beam treatment planning. Med. Phys. 34 (12), 4818–4853.

Cheung, T., Butson, M. J., Yu, P. K. N., 2005. Post-irradiation colouration of Gafchromic EBT radiochromic film. Phys. Med. Biol. 50 (20), N281–N285.

Chiou, S.-M., Lunsford, L. D., Niranjan, A., Kondziolka, D., Flickinger, J. C., 2001. Stereotactic radiosurgery of residual or recurrent craniopharyngioma, after surgery, with or without radiation therapy. Neuro-Oncol. 3 (3), 159–166.

Chong, E. K. P., Żak, S. H., 2001. An Introduction to Optimization, 2nd Edition. John Wiley & Sons, Inc., New York, NY.

Chui, C.-S., Spirou, S., Yang, J., Hong, L., Hunt, M., 2001. 3-D Conformal and Intensity Modulated Radiation Therapy: Physics and Clinical Applications. Advanced Medical

Publishing, Inc., Madison, WI, Ch. Helios optimization algorithm and IMRT planning process, pp. 277–291.

Chung, C., Nam, D.-H., Stupp, R., 2015. Union for International Cancer Control Manual of Clinical Oncology, 9th Edition. John Wiley & Sons, Inc., Oxford, UK, Ch. Central nervous system, pp. 706–725.

Cleave, C. D. V., 1963. Irradiation and the Nervous System. Roman and Littlefield, Inc., New York, NY, Ch. Effects of therapeutic doses of x-rays and radium on the central nervous system of man (1896 to 1945), pp. 71–111.

Colombo, F., Casentini, L., Cavedon, C., Stancanello, J., Francescon, P., Causin, F., Pinna, V., 2006. Radiosurgery: 7th International Stereotactic Radiosurgery Society Meeting. Vol. 6. Karger Medical and Scientific Publishers, Brussels, Belgium, Ch. Arteriovenous malformation radiosurgery: evolution of the technique, pp. 1–11.

Colombo, F., Cavedon, C., Casentini, L., Francescon, P., Causin, F., Pinna, V., 2009. Early results of CyberKnife radiosurgery for arteriovenous malformations. J. Neurosurg. 111 (4), 807–819.

Colombo, F., Pozza, F., Chierego, G., Casentini, L., De Luca, G., Francescon, P., 1994. Linear accelerator radiosurgery of cerebral arteriovenous malformations: an update. Neurosurgery 34 (1), 14–21.

Cook, M. J., 1965. The Anatomy of the Laboratory Mouse. Academic Press, Inc., New York, NY.

Cousins, C., Sharp, C., 2004. Medical interventional procedures—reducing the radiation risks. Clin. Radiol. 59 (6), 468–473.

Crijns, W., Maes, F., van der Heide, U., den Heuvel, F. V., 2013. Calibrating page sized Gafchromic EBT3 films. Med. Phys. 40 (1), 012102–1–012102–13.

Davis, L., Steenstrup, M., 1987. Genetic Algorithms and Simulated Annealing. Research Notes in Artificial Intelligence. Morgan Kaufmann Publishers, Inc., Los Altos, CA, Ch. Genetic Algorithms and Simulated Annealing: an overview, pp. 1–11.

Davis, S. D., Ross, C. K., Mobit, P. N., Van der Zwan, L., Chase, W. J., Shortt, K. R., 2003. The response of LiF thermoluminescence dosemeters to photon beams in the energy range from 30 kV x-rays to ^{60}Co gamma rays. Radiat. Prot. Dosim. 106 (1), 33–43.

DeAngelis, L. M., 2004. Manual of Clinical Oncology, 5th Edition. Lippincott Williams & Wilkins, Philadelphia, PA, Ch. Neurological tumors, pp. 321–332.

DeAngelis, L. M., Posner, J. B., 2001. Clinical Oncology. American Cancer Society, Inc., Atlanta, GA, Ch. Cancer of the central nervous system and pituitary gland, pp. 653–704.

della Cuna, G. R., Gasparini, M., 1988. Handbook of Medical Oncology, 3rd Edition. Year Book Medical Publishers, Inc., Chicago, IL, Ch. Neoplasms of the nervous system, pp. 435–452.

Deloar, H. M., Kunieda, E., Kawase, T., Saitoh, H., Ozaki, M., Fujisaki, T., Myojoyama, A., Saito, K., Takagi, S., Sato, O., Kubo, A., 2004. Monte Carlo simulations for stereotactic radiotherapy system with various kilovoltage x-ray energy. In: Namito, Y., Hirayama, H., Ban, S. (Eds.), Third International EGS Workshop. Vol. 2005-3. KEK Proceedings, High Energy Accelerator Research Organization, Tsukuba, Japan, pp. 172–179.

Deloar, H. M., Kunieda, E., Kawase, T., Tsunoo, T., Saitoh, H., Ozaki, M., Saito, K., Takagi, S., Sato, O., Fujisaki, T., Myojoyama, A., Sorell, G., 2006. Investigations of different kilovoltage x-ray energy for three-dimensional converging stereotactic radiotherapy system: Monte Carlo simulations with CT data. Med. Phys. 33 (12), 4365–4642.

Demiral, S., Beyzadeoglu, M., Sager, O., Dincoglan, F., Gamsiz, H., Uysal, B., Oysul, K., Gundem, E., Dirican, B., Sirin, S., 2014. Evaluation of linear accelerator (linac)-based

stereotactic radiosurgery (SRS) for the treatment of craniopharyngiomas. Int. J. Hematol. Oncol. 24 (2), 123–129.

Devic, S., 2011. Radiochromic film dosimetry: Past, present, and future. Phys. Med. 27 (3), 122–134.

Devic, S., Aldelaijan, S., Mohammed, H., Tomic, N., Liang, L., Deblois, F., Seuntjens, J., 2010. Absorption spectra time evolution of EBT-2 model GAFCHROMIC™ film. Med. Phys. 37 (5), 2207–2214.

Devic, S., Seuntjens, J., Hegyi, G., Podgorsak, E., Soares, C. G., Kirov, A. S., Ali, I., Williamson, J. F., Elizondo, A., 2004. Dosimetric properties of improved GafChromic films for seven different digitizers. Med. Phys. 31 (9), 2392–2401.

Devic, S., Seuntjens, J., Sham, E., Podgorsak, E. B., Schmidtlein, C. R., Kirov, A. S., Soares, C. G., 2005. Precise radiochromic film dosimetry using a flat-bed document scanner. Med. Phys. 32 (7), 2245–2253.

Devic, S., Tomic, N., Aldelaijan, S., DeBlois, F., Seuntjens, J., Chan, M. F., Lewis, D., 2012. Linearization of dose-response curve of the radiochromic film dosimetry system. Med. Phys. 39 (8), 4850–4857.

Devic, S., Tomic, N., Soares, C. G., Podgorsak, E. B., 2009. Optimizing the dynamic range extension of a radiochromic film dosimetry system. Med. Phys. 36 (2), 429–437.

Dreindl, R., Georg, D., Stock, M., 2014. Radiochromic film dosimetry: Considerations on precision and accuracy for EBT2 and EBT3 type films. Z. Med. Phys. 24 (2), 153–163.

Ebert, M. A., Asad, A. H., Siddiqui, S. A., 2009. Suitability of radiochromic films for dosimetry of low energy x-rays. J. Appl. Clin. Med. Phys. 10 (4), 232–240.

Engel, Jr., J., 2001. Mesial temporal lobe epilepsy: what have we learned? Neuroscientist 7 (4), 340–352.

Evgeniia, S., Leonid, S., Evgeniy, M., 2015. Polimer Gafchromic EBT3 films in clinical dosimetry. Adv. Mat. Res. 1084, 572–576.

Fagerstrom, J. M., Bender, E. T., Culberson, W. S., 2016. Technical Note: Dose gradients and prescription isodose in orthovoltage stereotactic radiosurgery. Med. Phys. 43 (5), 2072–2080.

Fano, U., 1953. Gamma-ray attenuation: basic processes. Nucleonics 11 (8), 8–12.

Ferreira, B. C., Lopes, M. C., Capela, M., 2009. Evaluation of an Epson flatbed scanner to read Gafchromic EBT films for radiation dosimetry. Phys. Med. Biol. 54 (4), 1073–1085.

Fiandra, C., Ricardi, U., Ragona, R., Anglesio, S., Giglioli, F. R., Calamia, E., Lucio, F., 2006. Clinical use of EBT model Gafchromic™ film in radiotherapy. Med. Phys. 33 (11), 4314–4319.

Flickinger, J. C., Lunsford, L. D., Kondziolka, D., Maitz, A. H., Epstein, A. H., Simons, S. R., Wu, A., 1992. Radiosurgery and brain tolerance: an analysis of neurodiagnostic imaging changes after Gamma Knife radiosurgery for arteriovenous malformations. Int. J. Radiat. Oncol. Biol. Phys. 23 (1), 19–26.

Flickinger, J. C., Niranjan, A., 2015. Principles and Practice of Stereotactic Radiosurgery. Springer Science & Business Media, LLC, New York, NY, Ch. Gamma Knife radiosurgery, pp. 111–119.

Forst, W., Hoffmann, D., 2010. Optimization: Theory and Practice. Springer Undergraduate Texts in Mathematics and Technology. Springer Science & Business Media, LLC, New York, NY.

Freeman, A., Flower, D., Rogers, G., Cross, H., Wong, I. C. K., Duncan, J., Jackson, M., Harnor, M., Kosky, N., Appleton, R., Gomersall, S., Mackey, S., Truscott, T., 2012. The epilepsies: the diagnosis and management of the epilepsies in adults and children in

primary and secondary care. Tech. rep., National Clinical Guideline Centre, London, UK, Partial Pharmacological Update of Clinical Guideline 20.

Fuss, M., Sturtewagen, E., De Wagter, C., Georg, D., 2007. Dosimetric characterization of GafChromic EBT film and its implication on film dosimetry quality assurance. Phys. Med. Biol. 52 (14), 4211–4225.

Ganz, J. C., 1998. Textbook of Stereotactic and Functional Neurosurgery. McGraw-Hill, Inc., New York, NY, Ch. Radiosurgery for pituitary tumors, pp. 845–855.

Gen, M., Cheng, R., 2000. Genetic Algorithms and Engineering Optimization. Wiley Series in Engineering Design and Automation. John Wiley & Sons, Inc., New York, NY.

Gibbs, J. W., 1898. Fourier's series. Nature 59 (1522), 200.

Gibbs, J. W., 1899. Fourier's series. Nature 59 (1539), 606.

Gill, S., Hill, R., 2013. A study on the use of Gafchromic™ EBT3 film for output factor measurements in kilovoltage x-ray beams. Australas. Phys. Eng. Sci. Med. 36 (4), 465–471.

Girard, F., Bouchard, H., Lacroix, F., 2012. Reference dosimetry using radiochromic film. J. Appl. Clin. Med. Phys. 13 (6), 339–353.

Goldberg, D. E., 1989. Genetic Algorithms in Search, Optimization, and Machine Learning. Addison-Wesley Publishing Company, Inc., Reading, MA.

Goldstein, H., 1980. Classical Mechanics, 2nd Edition. Addison-Wesley Publishing Company, Inc., Reading, MA, Ch. The kinematics of rigid body motion, pp. 128–187.

Gramegna, A., 1909. Un cas d'acromegalie traité par la radiothérapie. Note clinique. Rev. Neurol. 17, 15–17.

Greenberg, M. S., 2010. Handbook of Neurosurgery, 7th Edition. Thieme Medical Publishers, Inc., New York, NY.

Güler, O., 2010. Foundations of Optimization. Graduate Texts in Mathematics. Springer Science & Business Media, LLC, New York, NY.

Hainfeld, J. F., Slatkin, D. N., Smilowitz, H. M., 2004. The use of gold nanoparticles to enhance radiotherapy in mice. Phys. Med. Biol. 49 (18), N309–N315.

Hakim, R., Alexander, III, E., Loeffler, J. S., Shrieve, D. C., Wen, P., Fallon, M. P., Stieg, P. E., Black, P., 1998. Results of linear accelerator-based radiosurgery for intracranial meningiomas. Neurosurgery 42 (3), 446–454.

Hall, E. J., Giaccia, A. J., 2006. Radiobiology for the Radiologist, 6th Edition. Lippincott Williams & Wilkins, Philadelphia, PA.

Hamilty, J. M., Rahmat-Samii, Y., 1999. Electromagnetic Optimzation by Genetic Algorithms. Wiley Series in Microwave and Optical Engineering. John Wiley & Sons, Inc., New York, NY, Ch. An introduction to Genetic Algorithms, pp. 1–28.

Hammer, C. G., Rosen, B. S., Fagerstrom, J. M., Culberson, W. S., DeWerd, L. A., 2017. Experimental investigation of GafChromic® EBT3 intrinsic energy-dependence with kilovoltage x-rays, ^{137}Cs, and ^{60}Co. Med. Phys. (Manuscript in preparation).

Hammond, F. M., Masel, T., 2012. Brain Injury Medicine, 2nd Edition. Demos Medical Publishing, LLC, New York, NY, Ch. Cranial nerve disorders, pp. 680–692.

Hara, Y., Furukawa, T., Mizushima, K., Takeshita, E., Shirai, T., Noda, K., 2014. Application of radiochromic film for quality assurance in the heavy-ion beam scanning irradiation system at HIMAC. Nucl. Instr. Meth. Phys. Res. B 331, 253–256.

Haupt, R. L., Haupt, S. E., 2004. Practical Genetic Algorithms, 2nd Edition. John Wiley & Sons, Inc., Hoboken, NJ.

Haupt, R. L., Werner, D. H., 2007. Genetic Algorithms in Electromagnetics. John Wiley & Sons, Inc., Hoboken, NJ.

Hendee, W. R., Ritenour, E. R., 2002. Medical Imaging Physics, 4th Edition. John Wiley & Sons, Inc., New York, NY, Ch. Human radiobiology, pp. 413–433.

Hermida-López, M., Lüdemann, L., Flühs, A., Bruall, L., 2014. Technical Note: Influence of the phantom material on the absorbed-dose energy dependence of the EBT3 radiochromic film for photons in the energy range 3 keV–18 MeV. Med. Phys. 41 (11), 112103–1–112103–6.

Hill, R., Healy, B., Holloway, L., Kuncic, Z., Thwaites, D., Baldock, C., 2014. Advances in kilovoltage x-ray beam dosimetry. Phys. Med. Biol. 59 (6), 183–231.

Hoffman, H. J., 1994. Surgical management of craniopharyngioma. Pediatr. Neurosurg. 21 (Suppl 1), 44–49.

Holland, J. H., 1975. Adaptation in natural and artificial systems: an introductory analysis with applications to biology, control, and artificial intelligence. The MIT Press, Cambridge, MA.

Hong, L. X., Garg, M., Lasala, P., Kim, M., Mah, D., Chen, C.-C., Yaparpalvi, R., Mynampati, D., Kuo, H.-C., Guha, C., Kalnicki, S., 2011. Experience of micromultileaf collimator linear accelerator based single fraction stereotactic radiosurgery: tumor dose inhomogeneity, conformity, and dose fall off. Med. Phys. 38 (3), 1239–1247.

Hopewell, J. W., Morris, A. D., Dixon-Brown, A., 1987. The influence of field size on the late tolerance of the rat spinal cord to single doses of x-rays. Br. J. Radiol. 60 (719), 1099–1108.

Howard, S. P., January 2017. Personal communication, interview conducted at the University of Wisconsin Clinical Sciences Center.

Hårdemark, B., Liander, A., Rehbinder, H., Löf, J., 2004. P^{3}IMRT® direct machine parameter optimization. Pinnacle^3® white paper, Philips Medical Systems, Inc., Eindhoven, Netherlands.

Hubbell, H., 1999. Review of photon interaction cross section data in the medical and biological context. Phys. Med. Biol. 44 (1), R1–R22.

Hubbell, J. H., Seltzer, S. M., 2004. Tables of x-ray mass attenuation coefficients and mass energy-absorption coefficients (Version 1.4). Tech. rep., National Institute of Standards and Technology, Gaithersburg, MD, available: http://physics.nist.gov/xaamdi (last accessed November 4, 2016).

Hwang, A., Ma, L., 2011. Gamma Knife Radiosurgery. InTech, Rijeka, Croatia, Ch. Advanced Gamma Knife treatment planning of epilepsy, pp. 123–132.

ICRP Publication 60, 1991. 1990 Recommendations of the International Commission on Radiological Protection. Ann. ICRP 21 (1-3), 1–201.

ICRP Publication 85, 2000. Avoidance of radiation injuries from medical intervention procedures. Ann. ICRP 30 (2), 7–67.

ICRP Publication 92, 2003. Relative Biological Effectiveness (RBE), Quality Factor (Q), and Radiation Weighting Factor (w_R). Ann. ICRP 33 (4), 1–117.

ICRU Report 37, 1984. Stopping powers for electrons and positions. Tech. rep., International Commission on Radiation Units and Measurements, Bethesda, MD.

ICRU Report 39, 1985. Determination of dose equivalents resulting from external radiation sources. Tech. rep., International Commision on Radiation Units and Measurements, Bethesda, MD.

ICRU Report 44, 1989. Tissue substitutes in radiation dosimetry and measurement. Tech. rep., International Commision on Radiation Units and Measurements, Bethesda, MD.

ICRU Report 50, 1993. Prescribing, recording, and reporting photon beam therapy. Tech. rep., International Commission on Radiation Units and Measurements, Bethesda, MD.

ICRU Report 62, 1999. Prescribing, recording, and reporting photon beam therapy: Supplement to ICRU Report 50. Tech. rep., International Commission on Radiation Units and Measurements, Bethesda, MD.

Iwata, H., Sato, K., Tatewaki, K., Yokota, N., Inoue, M., Baba, Y., Shibamoto, Y., 2011. Hypofractionated stereotactic radiotherapy with CyberKnife for nonfunctioning pituitary adenoma: high local control with low toxicity. Neuro-Oncol. 13 (8), 916–922.

Jaco, J. W., Miller, D. L., 2010. Measuring and monitoring radiation dose during fluoroscopically guided procedures. Tech. Vasc. Interv. Radiol. 13 (3), 188–193.

Johnson, D. R., Kyriou, J., Morton, E. J., Clifton, A., Fitzgerald, M., Macsweeney, E., 2000. Radiation protection in interventional radiology. Clin. Radiol. 56 (2), 99–106.

Kairn, T., Aland, T., Kenny, J., 2010. Local heterogeneities in early batches of EBT2 film: a suggested solution. Phys. Med. Biol. 55 (15), L37–L42.

Kajiwara, K., Saito, K., Yoshikawa, K., Kato, S., Akimura, T., Nomura, S., Ishihara, H., Suzuki, M., 2005. Image-guided stereotactic radiosurgery with the CyberKnife for pituitary adenomas. Minim. Invasive Neurosurg. 48 (2), 91–96.

Kathren, R. L., 1987. The Dosimetry of Ionizing Radiation. Vol. II. Academic Press, Inc., San Diego, CA, Ch. External beta-photon dosimetry for radiation protection, pp. 321–370.

Kaul, D., Badakhshi, H., Gevaert, T., Budach, D. P. A., Tulaesca, C., Gruen, A., Prasad, V., Levivier, M., Kufeld, M., 2015. Dosimetric comparison of different treatment modalities for stereotactic radiosurgery of meningioma. Acta Neurochir. 157 (4), 559–564.

Kawrakow, I., 2000a. Accurate condensed history Monte Carlo simulation of electron transport. I. EGSnrc, the new EGS4 version. Med. Phys. 27 (3), 485–498.

Kawrakow, I., 2000b. Accurate condensed history Monte Carlo simulation of electron transport. II. Application to ion chamber response simulations. Med. Phys. 27 (3), 499–513.

Kawrakow, I., 2005. EGSnrc C++ class library. PIRS-898. Tech. rep., National Research Council of Canada, Ottawa, Canada.

Kawrakow, I., Mainegra-Hing, E., Rogers, D. W. O., Tessier, F., Walters, B., 2010. The EGSnrc code system: Monte Carlo simulation of electron and photon transport. PIRS-701. Tech. rep., National Research Council of Canada, Ottawa, Canada.

Kayalilar, N., Caglar, H., Aydin, G., Gungor, G., Yapici, B., Atalar, B., Ozyar, E., Şengöz, M., 2013. Comparison of CyberKnife and GammaKnife treatment plans for target volume and normal tissue doses. J. Radiosurg. SBRT 2 (Suppl. 2.1), 105.

Keller, B. M., Beachey, D. J., Pignol, J.-P., 2007. Experimental measurement of radiological penumbra associated with intermediate energy x-rays (1 MV) and small radiosurgery field sizes. Med. Phys. 34 (10), 3996–4002.

Keller, B. M., Pignol, J.-P., Presutti, J., Beachey, D. J., 2009. Intermediate energy photons (1 MV) to improve dose gradient, conformality, and homogeneity: Potential benefits for small field intracranial radiosurgery. Med. Phys. 36 (1), 33–39.

Kelsey, C. A., Heintz, P. H., Sandoval, D. J., Chambers, G. D., Adolphi, N. L., Paffett, K. S., 2014. Radiation Biology of Medical Imaging. John Wiley & Sons, Inc., Hoboken, NJ.

Kim, W., Clelland, C., Yang, I., Pouratian, N., 2012. Comprehensive review of stereotactic radiosurgery for medical and surgical refractory pituitary adenomas. Surg. Neurol. Int. 3 (Suppl 2), S79–S89.

Kim, Y.-H., Kim, D. G., Han, J. H., Chung, H.-T., Kim, I. K., Song, S. W., Park, J.-H., Kim, J. W., Kim, Y. H., Park, C.-K., Kim, C.-Y., Paek, S. H., Jung, H.-W., 2013.

Hearing outcomes after stereotactic radiosurgery for unilateral intracanalicular vestibular schwannomas: implication of transient volume expansion. Int. J. Radiat. Oncol. Biol. Phys. 85 (1), 61–67.

Kissick, M. W., Fakhraei, S., 2016. Lectures on Radiation Dosimetry Physics: A Deeper Look into the Foundations of Clinical Protocols. Medical Physics Publishing, Madison, WI.

Kissick, M. W., Flynn, R. T., Westerly, D. C., Mackie, T. R., Hoban, P. W., 2007. On the making of sharp longitudinal dose profiles with helical tomotherapy. Phys. Med. Biol. 52 (21), 6497–6510.

Kjellberg, R. N., 1979. Isoeffective dose parameters for brain necrosis in relation to proton radiosurgical dosimetry. In: Szikla, G. (Ed.), Stereotactic Cerebral Irradiation. Vol. 12. INSERM Symposium, Elsevier/North-Holland Biomedical Press, Amsterdam, Netherlands, pp. 157–166.

Kjellberg, R. N., Hanamura, T., Davis, K. R., Lyons, S. L., Adams, R. D., 1983. Bragg-peak proton-beam therapy for arteriovenous malformations of the brain. N. Engl. J. Med. 309 (5), 269–274.

Klassen, N. V., van der Zwan, L., Cygler, J., 1997. Gafchromic MD-55: Investigated as a precision dosimeter. Med. Phys. 24 (12), 1924–1934.

Koch, H., Motz, J., 1959. Bremsstrahlung cross-section formulas and related data. Rev. Mod. Phys. 31 (4), 920–955.

Kondziolka, D., 1999. Functional radiosurgery. Neurosurgery 44 (1), 12–20.

Kondziolka, D., Flickinger, J. C., Lunsford, L. D., 2013. Intracranial Stereotactic Radiosurgery. Elsevier Health Sciences, Philadelphia, PA, Ch. Stereotactic radiosurgery for epilepsy and functional disorders, pp. 623–632.

Kondziolka, D., Flickinger, J. C., Niranjan, A., Lunsford, L. D., 2012. Trends and importance of radiosurgery for the development of functional neurosurgery. Surg. Neurol. Int. 3 (Suppl.), S3–S9.

Kondziolka, D., Lunsford, D., Coffey, R. J., Flickinger, J. C., 1991. Stereotactic radiosurgery of meningiomas. J. Neurosurg. 74, 552–559.

Kondziolka, D., Lunsford, L. D., McLaughlin, M. R., Flickinger, J. C., 1998. Long-term outcomes after radiosurgery for acoustic neuromas. N. Engl. J. Med. 339 (20), 1426–1433.

Kondziolka, D., Lunsford, L. D., Witt, T. C., Flickinger, J. C., 2000. The future of radiosurgery: radiobiology, technology, and applications. Surg. Neurol. 54 (6), 406–414.

Kooy, H. M., 1993. Stereotactic Radiosurgery. McGraw-Hill, Inc., New York, NY, Ch. Three-dimensional treatment planning for stereotactic radiosurgery, pp. 17–30.

Kry, S. F., Smith, S. A., Weathers, R., Stovall, M., 2012. Skin dose during radiotherapy: a summary and general estimation technique. J. Appl. Clin. Med. Phys. 13 (3), 20–34.

Kwan, P., Brodie, M. J., 2000. Early identification of refractory epilepsy. N. Engl. J. Med. 342 (5), 314–319.

Larson, D. A., Flickinger, J. C., Loeffler, J. S., 1993. The radiobiology of radiosurgery. Int. J. Radiat. Oncol. Biol. Phys. 25 (3), 557–561.

Lawless, M. J., 2016. Development of kilovoltage x-ray dosimetry methods and their application to cone beam computed tomography. Ph.D. thesis, University of Wisconsin, Madison, WI.

Laws, E. R., Sheehan, J. P., Sheehan, J. M., Jagnathan, J., Jane, Jr., J. A., Oskouian, R., 2004. Stereotactic radiosurgery for pituitary adenomas: a review of the literature. J. Neurooncol. 69, 257–272.

Lee, M., Kalani, M. Y. S., Cheshier, S., Gibbs, I. C., Adler, Jr., J. R., Chang, S. D., 2008. Radiation therapy and CyberKnife radiosurgery in the management of craniopharyngiomas. Neurosurg. Focus 24 (5), E4 (1–7).

Leenstra, J. L., Tanaka, S., Kline, R. W., Brown, P. D., Link, M. J., Nippoldt, T. B., Young, J. W. F., Pollock, B. E., 2010. Factors associated with endocrine deficits after stereotactic radiosurgery of pituitary adenomas. Neurosurgery 67 (1), 27–33.

Leksell, L., 1949. A stereotactic apparatus for intracerebral surgery. Acta Chir. Scand. 99, 229–233.

Leksell, L., 1951. The stereotaxis method and radiosurgery of the brain. Acta Chir. Scand. 102, 316–319.

Leksell, L., 1983. Stereotactic radiosurgery. J. Neurol. Neurosurg. Psychiatry 46 (9), 797–803.

Lemieux, C., 1972. Monte Carlo and Quasi-Monte Carlo Sampling. Springer Science & Business Media, LLC, New York, NY, Ch. Sampling from known distributions, pp. 41–56.

Levy, R. P., Lo, E. H., Fabrikant, J. I., 1993. Physical Aspects of Stereotactic Radiosurgery. Plenum Publishing Corporation, New York, NY, Ch. Clinical applications of stereotactic radiosurgery, pp. 239– 278.

Lewis, D., Chan, M. F., 2015. Correcting lateral response artifacts from flatbed scanners for radiochromic film dosimetry. Med. Phys. 42 (1), 416–429.

Lewis, D., Micke, A., Yu, X., Chan, M. F., 2012. An efficient protocol for radiochromic film dosimetry combining calibration and measurement in a single scan. Med. Phys. 39 (10), 6339–6350.

Li, H., Ruan, J., Xie, Z., Wang, H., Liu, W., 2007. Investigation of the critical geometric characteristics of living human skulls utilising medical image analysis techniques. Int. J. Veh. Saf. 2 (4), 345–367.

Lim, M. L. F., 2006. Principles and practice of clinical physics and dosimetry. Advanced Medical Publishing, Inc., Madison, WI.

Lindquist, C., Paddick, I., 2007. The Leksell Gamma Knife Perfexion and comparisons with its predecessors. Neurosurgery 61 (3 Suppl.), 130–140.

Lindsay, P., Rink, A., Ruschin, M., Jaffray, D., 2010. Investigation of energy dependence of EBT and EBT-2 Gafchromic film. Med. Phys. 37 (2), 571–576.

Louis, D. N., Ohgaki, H., Wiestler, O. D., Cavenee, W. K., Burger, P. C., Jouvet, A., Scheithauer, B. W., Kleihues, P., 2007. The 2007 WHO classification of tumours of the central nervous system. Acta Neuropathol. 114 (2), 97–109.

Lucy, L., 1974. An iterative technique for the rectification of observed distributions. Astron. J. 79 (6), 745–754.

Lunsford, L. D., 1991. Neurosurgery Update II: Vascular, Spinal, Pediatric, And Functional Neurosurgery. McGraw-Hill, Inc., St. Louis, MO, Ch. Stereotactic radiosurgery of intracranial arteriovenous malformations, pp. 175–185.

Lynch, B. D., Kozelba, J., Ranade, M. K., Li, J. G., Simon, W. E., Dempsey, J. F., 2006. Important considerations for radiochromic film dosimetry with flatbed CCD scanners and EBT GAFCHROMIC® film. Med. Phys. 33 (12), 4551–4556.

Ma, C., Faddegon, B., Rogers, D., Mackie, T., 1997. Accurate characterization of Monte Carlo calculated electron beams for radiotherapy. Med. Phys. 24 (3), 401–416.

Ma, C. M., Rogers, D. W. O., 1995. BEAMDP as a general-purpose utility. PIRS-509e. Tech. rep., National Research Council of Canada, Ottawa, Canada.

Mackie, T. R., Bielajew, A. F., Rogers, D. W. O., Battista, J. J., 1988. Generation of photon energy deposition kernels using the EGS Monte Carlo code. Phys. Med. Biol. 33 (1), 1–20.

Mainegra-Hing, E., Rogers, D. W. O., Kawrakow, I., 2005. Calculation of photon energy deposition kernels and electron dose point kernels in water. Med. Phys. 32 (3), 685–699.

Mansky, P. J., Hamilty, J. M., 2001. Bethesda Handbook of Clinical Onocology. Lippincott Williams & Wilkins, Philadelphia, PA, Ch. Central Nervous System tumors, pp. 397–418.

Marchetti, M., Bianchi, S., Milanesi, I., Bergantin, A., Bianchi, L., Broggi, G., Fariselli, L., 2011. Multisession radiosurgery for optic nerve sheath meningiomas—an effective option: Preliminary results of a single-center experience. Neurosurgery 69 (5), 1116–1122.

Martišìkovà, M., Ackermann, B., Jäkel, O., 2008. Analysis of uncertainties in Gafchromic EBT film dosimetry of photon beams. Phys. Med. Biol. 53 (24), 7013–7027.

Massager, N., Maris, C., Nissim, O., Devriendt, D., Salmon, I., Levivier, M., 2009. Experimental analysis of radiation dose distribution in radiosurgery: dose fall-off outside the target volume. Stereotact. Funct. Neurosurg. 87, 137–142.

Massager, N., Nissim, O., Delbrouck, C., Devriendt, D., David, P., Desmedt, F., Wikler, D., Hassid, S., Brotchi, J., Levivier, M., 2006. Role of intracanalicular volumetric and dosimetric parameters on hearing preservation after vestibular schwannoma radiosurgery. Int. J. Radiat. Oncol. Biol. Phys. 64 (5), 1331–1340.

Massillon-JL, G., Chiu-Tsao, S., Domingo-Munoz, I., Chan, M., 2012. Energy dependence of the new Gafchromic EBT3 film: Dose response curves for 50 kV, 6 and 15 MV x-ray beams. Int. J. Med. Phys. Clin. Eng. Radiat. Oncol. 1 (2), 60–65.

Massillon-JL, G., Cueva-Prócel, D., Díaz-Aguirre, P., Rodríguez-Ponce, M., Herrera-Martínez, F., 2013. Dosimetry for small fields in stereotactic radiosurgery using Gafchromic MD-V2-55 film, TLD-100 and alanine dosimeters. PloS One 8 (5), 1–8.

Matrosic, C., Culberson, W., Rosen, B., Madsen, E., Frank, G., Bednarz, B., 2016. Initial characterization of a gel patch dosimeter for *in vivo* dosimetry. Phys. Med. Biol. 61 (10), N240–N248.

McCaw, T. J., 2015. Characterization of interplay errors in step-and-shoot intensity-modulated radiation therapy of the lung. Ph.D. thesis, University of Wisconsin, Madison, WI.

McHaffie, D., Khuntia, D., Suh, J. H., Tomé, W. A., Mehta, M. P., 2012. Clinical Radiation Oncology, 3rd Edition. Elsevier Health Sciences, Philadelphia, PA, Ch. Stereotactic irradiation: linear accelerator and Gamma Knife, pp. 331–343.

McLaughlin, W. L., 1970. Manual on Radiation Dosimetry. Dekker, New York, NY, Ch. Film, dyes, and photographic systems, pp. 129–177.

McLaughlin, W. L., Al-Sheikhly, M., Lewis, D. F., Kovacs, A., Wojnarovits, L., 1996. Irradiation of Polymers: Fundamentals and Technological Advances. Vol. 620 of ACS Symposium Series. American Chemical Society, Washington, DC, Ch. Radiochromic solid-state polymerization reaction, pp. 152–166.

Medina, L.-A., Herrera-Penilla, B.-I., Castro-Morales, M.-A., García-López, P., Jurado, R., Pérez-Cárdenas, E., Chanona-Vilchis, J., Brandan, M.-E., 2008. Use of an orthovoltage x-ray treatment unit as a radiation research system in a small-animal cancer model. J. Exp. Clin. Canc. Res. 27 (1), 57–68.

Meeks, S. L., Buatti, J. M., Bova, F. J., Friedman, W. A., Mendenhall, W. M., 1998. Treatment planning optimization for linear accelerator radiosurgery. Int. J. Radiat. Oncol. Biol. Phys. 41 (1), 183–197.

Melanie, M., 1999. An Introduction to Genetic Algorithms. MIT Press, Cambridge, MA.

Messac, A., 2015. Optimization in Practice with MATLAB® for Engineering Students and Professionals. Cambridge University Press, New York, NY.

Moga, J., DeWerd, L., 2010. Characterization of kilovoltage x-ray spectra using measurements with a high-purity germanium detector and Monte Carlo simulations. Med. Phys. 37, 3427, abstract.

Moga, J. D., 2011. Characterization of low-energy photon-emitting brachytherapy sources and kilovoltage x-ray beams using spectrometry. Ph.D. thesis, UW-Madison.

Mora, G. M., Maio, A., Rogers, D. W. O., 1999. Monte Carlo simulation of a typical ^{60}Co therapy source. Med. Phys. 26 (11), 2494–2502.

Morrill, S. M., Lane, R. G., Rosen, I. I., 1990. Constrained simulated annealing for optimized radiation therapy treatment planning. Comput. Meth. Prog. Bio. 33 (3), 135–144.

Morrison, H., Menon, G., Sloboda, R., 2014. Radiochromic film calibration for low-energy seed brachytherapy dose measurement. Med. Phys. 41 (7), 072101–1–072101–11.

Moylan, R., Aland, T., Kairn, T., 2013. Dosimetric accuracy of Gafchromic EBT2 and EBT3 film for in vivo dosimetry. Australas. Phys. Eng. Sci. Med. 36 (3), 331–337.

Muir, B. R., Rogers, D. W. O., 2010. Monte Carlo calculations of k_{Q}, the beam quality conversion factor. Med. Phys. 37 (11), 5939–5950.

Najim, K., Ikonen, E., Daoud, A.-K., 2004. Stochastic Processes: Estimation, Optimisation and Analysis. Butterworth-Heinemann, Sterling, VA.

Nakazawa, H., Mori, Y., Komori, M., Tsugawa, T., Shibamoto, Y., Kobayashi, T., Hashizume, C., Uchiyama, Y., Hagiwara, M., 2014. Simulational study of a dosimetric comparison between a Gamma Knife treatment plan and an intensity-modulated radiotherapy plan for skull base tumors. J. Radiat. Res. 55 (3), 518–526.

Nataf, F., Ghossoub, M., Schlienger, M., Moussa, R., Meder, J.-F., Roux, F.-X., 2004. Bleeding after radiosurgery for cerebral arteriovenous malformations. Neurosurgery 55 (2), 298–306.

Nath, R., Biggs, P. J., Bova, F. J., Ling, C. C., Purdy, J. A., van de Geijn, J., Weinhous, M. S., 1994. AAPM code of practice for radiotherapy accelerators: Report of AAPM Radiation Therapy Task Group No. 45. Med. Phys. 21 (7), 1093–1121.

Nedzi, L. A., 2008. The implementation of ablative hypofractionated radiotherapy for stereotactic treatments in the brain and body: observations on the efficacy and toxicity in clinical practice. Semin. Radiat. Oncol. 18 (4), 265–272.

Nedzi, L. A., Kooy, H., Alexander, III, E., Gelman, R. S., Loeffler, J. S., 1991. Variables associated with the development of complications from radiosurgery of intracranial tumors. Int. J. Radiat. Oncol. Biol. Phys. 21 (3), 591–599.

Nias, A., 1988. Clinical Radiobiology, 2nd Edition. Churchill Livingstone, New York, NY.

Nias, A., 1990. An Introduction to Radiobiology. John Wiley & Sons, Inc., New York, NY.

Niranjan, A., Kano, H., Mathieu, D., Kondziolka, D., Flickinger, J. C., Lunsford, L. D., 2010. Radiosurgery for craniopharyngioma. Int. J. Radiat. Oncol. Biol. Phys. 78 (1), 64–71.

Niroomand-Rad, A., Blackwell, C. R., Coursey, B. M., Gall, K. P., Galvin, J. M., McLaughlin, W. L., Meigooni, A. S., Nath, R., Rodgers, J. E., Soares, C. G., 1998. Radiochromic film dosimetry: Recommendations of AAPM Radiation Therapy Committee Task Group 55. Med. Phys. 25 (11), 2093–2115.

Nunn, A., Davis, S., Micka, J., DeWerd, L. A., 2008. LiF:Mg,Ti TLD response as a function of photon energy for moderately filtered x-ray spectra in the range of 20 to 250 kVp relative to ^{60}Co. Med. Phys. 35 (5), 1859–1869.

O'Malley, L., Pignol, J.-P., Beachey, D. J., Keller, B. M., Presutti, J., Sharpe, M., 2006. Improvement of radiological penumbra using intermediate energy photons (IEP) for stereotactic radiosurgery. Phys. Med. Biol. 51 (10), 2537–2548.

Ondra, S. L., Troupp, H., George, E. D., , Schwab, K., 1990. The natural history of symptomatic arteriovenous malformations of the brain: a 24-year follow-up assessment. J. Neurosurg. 73 (2), 387–391.

O'Neill, B. P., Iturria, N. J., Link, M. J., Pollock, B. E., Ballman, K. V., O'Fallon, J. R., 2003. A comparison of surgical resection and stereotactic radiosurgery in the treatment of solitary brain metastases. Int. J. Radiat. Oncol. Biol. Phys. 55 (5), 1169–1176.

O'Reilly, M. A., Muller, A., Hynynen, K., 2011. Ultrasound insertion loss of rat parietal bone appears to be proportional to animal mass at sub-megahertz frequencies. Ultrasound Med. Biol. 37 (11), 1930–1937.

Oster, J. M., Gutrecht, J. A., Bagla, R., Arle, J. E., Cosgrove, G. R., 2012. Netter's Neurology, 2nd Edition. Elsevier Health Sciences, Philadelphia, PA, Ch. Epilepsy, pp. 175–190.

Pachamanova, D. A., Fabozzi, F. J., 2010. Simulation and Optimization in Finance: Modeling with MATLAB, @RISK, or VBA. John Wiley & Sons, Inc., Hoboken, NJ, Ch. Optimization modeling, pp. 143–210.

Paddick, I., 2013. Gamma Knife evolution: How have technical developments enhanced the quality of treatment plans? J. Radiosurg. SBRT 2 (Suppl. 1), 138.

Paddick, I., Lippitz, B., 2006. A simple dose gradient measurement tool to complement the conformity index. J. Neurosurg. 105 (Suppl.), 194–201.

Paelinck, L., De Neve, W., De Wagter, C., 2007. Precautions and strategies in using a commercial flatbed scanner for radiochromic film dosimetry. Phys. Med. Biol. 52 (1), 231–242.

Papaconstadopoulos, P., Hegyi, G., Seuntjens, J., Devic, S., 2014. A protocol for EBT3 radiochromic film dosimetry using reflection scanning. Med. Phys. 41 (12), 122101–1–122101–6.

Pedregal, P., 2004. Introduction to Optimization. Vol. 46 of Texts in Applied Mathematics. Springer Science & Business Media, LLC, Berlin, Germany.

Pidikiti, R., Song, S. S., Speiser, M., Seliounine, S., Saha, D., Solberg, T., 2009. Image-guided stereotactic small animal irradiator. In: Dössel, O., Schlegel, W. C. (Eds.), World Congress on Medical Physics and Biomedical Engineering. Vol. 25/XIII. International Federation for Medical and Biological Engineering, Springer Science & Business Media, LLC, Munich, Germany, pp. 55–58.

Pincus, J. H., Tucker, G. J., 2003. Behavioral Neurology, 4th Edition. Oxford University Press, Inc., New York, NY.

Plowman, P. N., Wraith, C., Royle, N., Grossman, A. B., 1999. Stereotactic radiosurgery IX. Craniopharyngioma: durable complete imaging responses and indications for treatment. Br. J. Neurosurg. 13 (4), 352–358.

Podgorsak, E. B., 2005. Radiation Oncology Physics: A Handbook for Teachers and Students. International Atomic Energy Agency, Vienna, Austria.

Podgorsak, E. B., Podgorsak, M. B., 1999. The Modern Technology of Radiation Oncology. Medical Physics Publishing, Madison, WI, Ch. Stereotactic radiosurgery, pp. 588–639.

Pollock, B. E., Flickinger, J. C., Lunsford, L. D., Bissonette, D. J., Kondziolka, D., 1995. Hemorrhage risk after stereotactic radiosurgery of cerebral arteriovenous malformations. Neurosurgery 38 (4), 652–661.

Pollock, B. E., Stafford, S. L., 2005. Results of stereotactic radiosurgery for patients with imaging defined cavernous sinus meningiomas. Int. J. Radiat. Oncol. Biol. Phys. 62 (5), 1427–1431.

Poludniowski, G., Landry, G., DeBlois, F., Evans, P. M., Verhaegen, F., 2009. SpekCalc: a program to calculate photon spectra from tungsten anode x-ray tubes. Phys. Med. Biol. 54 (19), N433–N438.

Poludniowski, G. G., 2007. Calculation of x-ray spectra emerging from an x-ray tube. Part II. X-ray production and filtration in x-ray targets. Med. Phys. 34 (6), 2175–2186.

Poludniowski, G. G., Evans, P. M., 2007. Calculation of x-ray spectra emerging from an x-ray tube. Part I. Electron penetration characteristics in x-ray targets. Med. Phys. 34 (6), 2164–2174.

Powers, B. E., Thames, H. D., Gillette, S. M., Smith, C., Beck, E. R., Gillette, E. L., 1998. Volume effects in the irradiated canine spinal cord: do they exist when the probability of injury is low? Radiother. Oncol. 46 (3), 297–306.

Prajapati, S., 2015. Development of micro-radiotherapy within the design of integrated small animal imaging and therapy system: an open-source medical devices initiative. Ph.D. thesis, University of Wisconsin, Madison, WI.

Prajapati, S., Mackie, T., Jeraj, R., 2014. Open-Source Medical Devices (OSMD) design of a small animal radiotherapy system. J. Phys.: Conf. Ser. 489 (1), 012017.

Prasad, K. N., 1995. Handbook of Radiobiology, 2nd Edition. CRC Press, LLC, New York, NY.

Puataweepong, P., Dhanachai, M., Dangprasert, S., Narkwong, L., Sitathanee, C., Sawangsilpa, T., Janwityanujit, T., Yongvithisatid, P., 2014. Linac-based stereotactic radiosurgery and fractionated stereotactic radiotherapy for vestibular schwannomas: comparative observations of 139 patients treated at a single institution. J. Radiat. Res. 55 (2), 351–358.

Quigg, M., Rolston, J., Barbaro, N. M., 2012. Radiosurgery for epilepsy: clinical experience and potential antiepiletic mechanisms. Epilepsia 53 (1), 7–15.

Rahman, W. N., Bishara, N., Ackerly, T., He, C. F., Jackson, P., Wong, C., Davidson, R., Geso, M., 2009. Enhancement of radiation effects by gold nanoparticles for superficial radiation therapy. Nanomed. Nanotech. Biol. Med. 5 (2), 136–142.

Raleigh, D. R., Barani, I. J., Sneed, P., Larson, D. A., 2016. Handbook of Evidence-Based Stereotactic Radiosurgery and Stereotactic Body Radiotherapy. Springer International Publishing, New York, NY, Ch. Intracranial Tumors, pp. 41–78.

Raymond, F., 1905. La syringomyélie. Rev. Gén. Clin. Thér. 19, 817–818.

Reed, J. L., Rasmussen, B. E., Davis, S. D., Micka, J. A., Culberson, W. S., DeWerd, L. A., 2014. Determination of the intrinsic energy dependence of LiF:Mg,Ti thermoluminescent dosimeters for ^{125}I and ^{103}Pd brachytherapy sources relative to ^{60}Co. Med. Phys. 41 (12), 122103–1–122103–11.

Reeves, C. R., Rowe, J. E., 2003. Genetic Algorithms—Principles and Perspectives: A Guide to GA Theory. Operations Research/Computer Science Interfaces Series. Kluwer Academic Publishers, New York, NY.

Regaud, C., Ferroux, R., 1927. Discordance des effects de rayons x, d'une part dans le testicile, par le peau, d'autre parts dans le fractionment de la dose. Compt. Rend. Soc. Biol. 97, 431–434.

Régis, J., Caron, R., Bartolomei, F., Chauvel, P., 2012. Seeking new paradigms in epilepsy: stereotactic radiosurgery. In: Clinical Neurosurgery. Vol. 59. Congress of Neurological Surgeons, Lippincott Williams & Wilkins, Baltimore, MD, pp. 59–69.

Régis, J., Caron, R., Bartolomei, F., Chauvel, P., 2013. Handbook of Radiosurgery in CNS Disease. Demos Medical Publishing, LLC, New York, NY, Ch. Radiosurgery for drug-resistant epilepsies: state of the art, results, and perspectives, pp. 161–179.

Reinhardt, S., Hillbrand, M., Wilkens, J., Assmann, W., 2012. Comparison of GafChromic EBT2 and EBT3 films for clinical photon and proton beams. Med. Phys. 39 (8), 5257–5262.

Reinhardt, S., Würl, M., Greubel, C., Humble, N., Wilkens, J. J., Mairani, M. H. A., Assmann, W., Parodi, K., 2015. Investigation of EBT2 and EBT3 films for proton dosimetry in the 4–20 MeV energy range. Radiat. Environ. Biophys. 54 (1), 71–79.

Richardson, W. H., 1972. Bayesian-based iterative method of image restoration. J. Opt. Soc. Am. 62 (1), 55–59.

Rink, A., Lewis, D. F., Varma, S., Vitkin, I. A., Jaffray, D. A., 2008. Temperature and hydration effects on absorbance spectra and radiation sensitivity of a radiochromic medium. Med. Phys. 35 (10), 4545–4555.

Rink, A., Vitkin, I., Jaffray, D., 2007. Energy dependence (75 kVp to 18 MV) of radiochromic film assessed using a real-time optical dosimeter. Med. Phys. 34 (2), 458–463.

Rogers, D. W. O., Bielajew, A. F., 1990. The Dosimetry of Ionizing Radiation. Vol. III. Academic Press, Inc., New York, NY, Ch. Monte Carlo techniques of electron and photon transport for radiation dosimetry, pp. 427–539.

Rogers, D. W. O., Faddegon, B. A., Ding, G. X., Ma, C., We, J., Mackie, T. R., 1995. BEAM: A Monte Carlo code to simulate radiotherapy treatments. Med. Phys. 22 (5), 503–524.

Rogers, D. W. O., Kawrakow, I., Seuntjens, J. P., Walters, B. R. B., 2011. NRC user codes for EGSnrc. PIRS-702. Tech. rep., National Research Council of Canada, Ottawa, Canada.

Rosen, B., Soares, C., Hammer, C., Kunugi, K., DeWerd, L., 2015. A prototype, glassless densitometer traceable to primary optical standards for quantitative radiochromic dosimetry. Med. Phys. 42 (7), 4055–4068.

Rosen, B. S., 2015. Advanced radiochromic film methodologies for quantitative dosimetry of small and nonstandard fields. Ph.D. thesis, University of Wisconsin, Madison, WI.

Ross, S. M., 2002. Simulation, 3rd Edition. Academic Press, Inc., San Diego, CA.

Rutigliano, M. J., Lunsford, L. D., Kondziolka, D., Strauss, M. J., Khanna, V., Green, M., 1995. The cost effectiveness of stereotactic radiosurgery versus surgical resection in the treatment of solitary metastatic brain tumors. Neurosurgery 37 (3), 445–455.

Ruzevick, J., Batra, S., Lim, M., Rigamonti, D., 2013a. Handbook of Radiosurgery in CNS Disease. Demos Medical Publishing, LLC, New York, NY, Ch. Radiosurgery for arteriovenous malformations, pp. 123–135.

Ruzevick, J., Lim, M., 2013. Handbook of Radiosurgery in CNS Disease. Demos Medical Publishing, LLC, New York, NY, Ch. Technology and Techniques of Cranial Radiosurgery, pp. 13–32.

Ruzevick, J., Lim, M., Rigamonti, D., 2013b. Handbook of Radiosurgery in CNS Disease. Demos Medical Publishing, LLC, New York, NY, Ch. Skull-base tumors: radiosurgery for vestibular schwannomas, pp. 83–91.

Saladin, K., 2005. Human Anatomy. McGraw-Hill, Inc., Madison, WI.

Saur, S., Frengen, J., 2008. Gafchromic EBT film dosimetry with flatbed CCD scanner: A novel background correction method and full dose uncertainty analysis. Med. Phys. 35 (7), 3094–3101.

Schell, M. C., Bova, F. J., Larson, D. A., Leavitt, D. D., Lutz, W. R., Podgorsak, E. B., Wu, A., 1995. Stereotactic radiosurgery: Report of AAPM Therapy Committee Task Group 42. Tech. rep., American Association of Physicists in Medicine.

Schultheiss, T. E., Stephens, L. C., Ang, K. K., Price, R. E., Peters, L. J., 1994. Volume effects in rhesus monkey spinal cord. Int. J. Radiat. Oncol. Biol. Phys. 29 (1), 67–72.

Schumer, W., Fernandoa, W., Carolan, M., Wonga, T., Wallace, S., Quong, G., Geso, M., 1999. Verification of brachytherapy dosimetry with radiochromic film. Med. Dosim. 24 (3), 197–203.

Seung, S. K., Larson, D. A., Galvin, J. M., Mehta, M. P., Potters, L., Schultz, C. J., Yajnik, S. V., Hartford, A. C., Rosenthal, S. A., 2013. American College of Radiology (ACR) and American Society for Radiation Oncology (ASTRO) practice guidelines for the performance of stereotactic radiosurgery (SRS). Am. J. Clin. Oncol. 36 (3), 310–315.

Shani, G., 1991. Radiation Dosimetry Instrumentation and Methods. CRC Press, LLC, Ann Arbor, MI.

Sharma, D. S., Dongre, P. M., Mhatre, V., Heigrujam, M., 2011. Physical and dosimetric characteristic of high-definition multileaf collimator (HDMLC) for SRS and IMRT. J. Appl. Clin. Med. Phys. 12 (3), 142–160.

Shaw, E., Kline, R., Gillin, M., Souhami, L., Hirschfeld, A., Dinapoli, R., Martin, L., 1993. Radiation Therapy Oncology Group: radiosurgery quality assurance guidelines. Int. J. Radiat. Oncol. Biol. Phys. 27 (5), 1231–1239.

Shaw, E., Scott, C., Souhami, L., Dinapoli, R., Bahary, J.-P., Wharam, R. K. M., Schultz, C., Davey, P., Loeffler, J., Rowe, J. D., Marks, L., Fisher, B., Shin, K., 1996. Radiosurgery for the treatment of previously irradiated recurrent primary brain tumors and brain metastases: Initial report of Radiation Therapy Oncology Group Protocol 90-05. Int. J. Radiat. Oncol. Biol. Phys. 34 (3), 647–654.

Shaw, E., Scott, C., Souhami, L., Dinapoli, R., Kline, R., Loeffler, J., Farnan, N., 2000. Single dose radiosurgical treatment of recurrent previously irradiated primary brain tumors and brain metastases: Final report of RTOG Protocol 90-05. Int. J. Radiat. Oncol. Biol. Phys. 47 (2), 291–298.

Shorvon, S., Duncan, J., Koepp, M., Sander, J., Smith, S., Walker, M., 2009. Neurology: A Queen Square Textbook. John Wiley & Sons, Inc., London, UK, Ch. Epilepsy and related disorders, pp. 189–243.

Shrieve, D., Loeffler, J., 2009. Textbook of Stereotactic and Functional Neurosurgery, 2nd Edition. Vol. 1. Springer Science & Business Media, LLC, Berlin, Germany, Ch. Radiobiology of stereotactic radiosurgery, pp. 853–866.

Shrieve, D. C., Loeffler, J. S., McDermott, M. W., Larson, D. A., 2010. Leibel and Phillips Textbook of Radiation Oncology, 3rd Edition. Elsevier Health Sciences, Philadelphia, PA, Ch. Radiosurgery, pp. 487–508.

Singh, R., Davis, J., Sharma, S., 2016. Stereotactic radiosurgery for trigeminal neuralgia: A retrospective multi-institutional examination of treatment outcomes. Cureus 8 (4), e554.

Sivanandam, S., Deepa, S., 2008. Introduction to Genetic Algorithms. Springer Science & Business Media, LLC, New York, NY.

Soares, C. G., 2006. Radiochromic film dosimetry. Radiat. Meas. 41 (Suppl 1), S100–S116.

Soares, C. G., 2009. Radiochromic film. In: Rogers, D., Cygler, J. E. (Eds.), Clinical Dosimetry Measurements in Radiotherapy. American Association of Physicists in Medicine Summer School, Medical Physics Publishing, Colorado Springs, CO, pp. 759–814.

Sorriaux, J., Kacperek, A., Rossomme, S., Lee, J., Bertrand, D., Vynckier, S., Sterpin, E., 2013. Evaluation of Gafchromic® EBT3 films characteristics in therapy photon, electron and proton beams. Phys. Med. 29 (6), 599–606.

Souhami, L., Seiferheld, W., Brachman, D., Podgorsak, E. B., Werner-Wasik, M., Lustig, R., Schultz, C. J., Sause, W., Okunieff, P., Buckner, J., Zamorano, L., Mehta, M. P., Curran, Jr., W. J., 2004. Randomized comparison of stereotactic radiosurgery followed by conventional radiotherapy with carmustine to conventional radiotherapy with carmustine

for patients with glioblastoma multiforme: Report of the Radiation Therapy Oncology Group 93-05 Protocol. Int. J. Radiat. Oncol. Biol. Phys. 60 (3), 853–860.

Sperduto, P. W., Mehta, M. P., Robins, H. I., Konski, A., Movsas, B., Schell, M., Wang, M., 2012. A Phase III trial of whole brain radiation therapy and stereotactic radiosurgery alone with Temozolomide or Erlotinib in patients with Non-Small Cell Lung Cancer and 1-3 brain metastases. RTOG Protocol 0320. Tech. rep., Radiation Therapy Oncology Group of the American College of Radiology.

Spiegelmann, R., Nissim, O., Menhel, J., Alezra, D., Pfeffer, R. M., 2002. Linear accelerator radiosurgery for meningiomas in and around the cavernous sinus. Neurosurgery 51 (6), 1373–1379.

St-Hilaire, J., Sévigny, C., Beaulieu, F., Gingras, L., Tremblay, D., Beaulieu, L., 2009. Optimization of photon beam energy in aperture-based inverse planning. J. Appl. Clin. Med. Phys. 10 (4), 36–54.

Storm, E., Israel, H. I., 1970. Photon cross sections from 1 keV to 100 MeV for elements Z=1 to Z=100. Nucl. Data, Sect. A 7 (6), 565–681.

Sutherland, J. G. H., Rogers, D. W. O., 2010. Monte Carlo calculated absorbed-dose energy dependence of EBT and EBT2 film. Med. Phys. 37 (3), 1110–1116.

Tacke, M. B., Simeon, N., Peter, H., Uwe, O., 2008. 6 MV dosimetric characterization of the 160 MLC$^{\mathrm{TM}}$, the new Siemens multileaf collimator. Med. Phys. 35 (5), 1635–1642.

Taylor, B. N., Kuyatt, C. E., 1994. Guidelines for evaluating and expressing the uncertainty of NIST measurement results. Technical Note 1297, National Institute of Standards and Technology.

The MathWorks, Inc., 2000. MATLAB Optimization Toolbox User's Guide. Natick, MA.

The MathWorks, Inc., 2012. MATLAB and Optimization Toolbox Release 2012b. Natick, MA.

Timmerman, R. D., 2008. An overview of hypofractionation and introduction to this issue of Seminars in Radiation Oncology. Semin. Radiat. Oncol. 18 (4), 215–222.

Tomic, N., Devic, S., DeBlois, F., Seuntjens, J., 2010. Reference radiochromic film dosimetry in kilovoltage photon beams during CBCT image acquisition. Med. Phys. 37 (3), 1083–1092.

Tubiana, M., Wambersie, A., 1990. Introduction to Radiobiology. Taylor & Francis Group, New York, NY.

UWRCL, 2016. Quality Manual I.3.3 Uncertainty Tables: Air Kerma Therapy, version 13.0. University of Wisconsin Radiation Calibration Laboratory, Madison, WI.

van Battum, L. J., Huizenga, H., 2006. The curvature of sensitometric curves for Kodak XV-2 film irradiated with photon and electron beams. Med. Phys. 33 (7), 2396–2403.

van der Kogel, A. J., 1991. Radiation Injury to the Nervous System. Raven Press, Ltd., New York, NY, Ch. Central nervous system radiation injury in small animal models, pp. 91–111.

van der Kogel, A. J., 1993. Stereotactic Radiosurgery. McGraw-Hill, Inc., New York, NY, Ch. Radiation Injury in the Central Nervous System, pp. 43–50.

Vatnitsky, S., 1997. Radiochromic film dosimetry for clinical proton beams. Appl. Radiat. Isot. 48 (5), 643–651.

Vaughan, A., Rao, S. S. D., 2016. Handbook of Evidence-Based Stereotactic Radiosurgery and Stereotactic Body Radiotherapy. Springer International Publishing, New York, NY, Ch. Radiobiology of Stereotactic Radiosurgery and Stereotactic Body Radiotherapy, pp. 11–19.

Verhaegen, F., Granton, P., Tryggestad, E., 2011. Small animal radiotherapy research platforms. Phys. Med. Biol. 56 (12), R55–R83.

Villarreal-Barajas, J. E., Khan, R. F. H., 2014. Energy response of EBT3 radiochromic films: implications for dosimetry in kilovoltage range. J. Appl. Clin. Med. Phys. 15 (1), 331–338.

Wagner, L. K., Eifel, P. J., Geise, R. A., 1994. Potential biological effects following high x-ray dose interventional procedures. J. Vasc. Interv. Radiol. 5 (1), 71–84.

Wagner, Jr., R. F., Casciato, D. A., 2004. Manual of Clinical Oncology, 5th Edition. Lippincott Williams & Wilkins, Philadelphia, PA, Ch. Cutaneous complications, pp. 564–572.

Whitley, D., 1994. A genetic algorithm tutorial. Stat. Comput. 4 (2), 65–85.

Wiemels, J., Wrensch, M., Claus, E. B., 2010. Epidemiology and etiology of meningioma. J. Neurooncol. 99 (3), 307–314.

Williams, M. J., Metcalfe, P. E., 2011. Radiochromic film dosimetry and its applications in radiotherapy. In: Rosenfeld, A., Kron, T., d'Errico, F., Moscovitch, M. (Eds.), Concepts and Trends in Medical Radiation Dosimetry. Vol. 1345 of Proceedings of the SSD Summer School. American Institute of Physics, Wollongong, Australia, pp. 75–99.

X-5 Monte Carlo Team, 2005. MCNP5 Users Manual—Code version 5, Report LA-UR-03-1987. Los Alamos National Laboratory, Los Alamos, NM.

X-6 Monte Carlo Team, 2014. MCNP6 Users Manual—Code version 6.1.1beta, Report LA-CP-14-00745. Los Alamos National Laboratory, Los Alamos, NM.

Yamamoto, M., 1999. Gamma Knife radiosurgery: technology, applications, and future directions. Neurosurg. Clin. N. Am. 10 (2), 181–202.

Yeo, I. J., Kim, J. O., 2004. A Procedural Guide to Film Dosimetry. Medical Physics Publishing, Madison, WI.

Yomo, S., Tamura, M., Carron, R., Porcheron, D., Régis, J., 2010. A quantitative comparison of radiosurgical treatment parameters in vestibular schwannomas: the Leksell Gamma Knife Perfexion versus Model 4C. Acta Neurochir. 152 (1), 47–55.

Yoon, S.-C., Suh, T.-S., Jang, H.-S., Chung, S.-M., Kim, Y.-S., Ryu, M.-R., Choi, K.-H., Son, H.-Y., Kim, M.-C., Shinn, K.-S., 1998. Clinical results of 24 pituitary macroadenomas with linac-based stereotactic radiosurgery. Int. J. Radiat. Oncol. Biol. Phys. 41 (4), 849–853.

Zeidan, O. A., Stephenson, S. A. L., Meeks, S. L., Wagner, T. H., Willoughby, T. R., Kupelian, P. A., Langen, K. M., 2006. Characterization and use of EBT radiochromic film for IMRT dose verification. Med. Phys. 33 (11), 4064–4072.

Zeman, E. M., 2007. Clinical Radiation Oncology, 2nd Edition. Elsevier Health Sciences, Philadelphia, PA, Ch. Biologic basis of radiation oncology, pp. 3–42.

Zhang, Z. M., Gentile, T. R., Migdall, A. L., Datla, R. U., 1997. Transmittance measurements for filters of optical density between one and ten. Appl. Opt. 36 (34), 8889–8895.

Zink, K., Wulff, J., 2012. Beam quality corrections for parallel-plate ion chambers in electron reference dosimetry. Phys. Med. Biol. 57 (7), 1831–1854.